DISSERTATIONES
PHYSICAE
UNIVERSITATIS
TARTUENSIS
150

SHIVASUBRAMANIAN GOPINATH

Advanced Multidimensional Incoherent Imaging Systems with Reconfigurable Axial and Spectral Resolutions

DISSERTATIONES PHYSICAE UNIVERSITATIS TARTUENSIS
150

DISSERTATIONES PHYSICAE UNIVERSITATIS TARTUENSIS
150

SHIVASUBRAMANIAN GOPINATH

Advanced Multidimensional Incoherent Imaging Systems with Reconfigurable Axial and Spectral Resolutions

UNIVERSITY OF TARTU
Press
1632

Faculty of Science and Technology, Institute of Physics, University of Tartu, Estonia

The dissertation was admitted on 10.06.2026, in partial fulfilment of the requirements for the degree of Doctor of Philosophy in Physics, and allowed for defence by the Scientific Defence Council of the Institute of Physics, University of Tartu.

Supervisor: Dr. Vijayakumar Anand
ERA CIPHR Chair Holder and Associate Professor
Institute of Physics, University of Tartu, Estonia

Opponent: Dr. Enrique Tajahuerce
Professor, Institute of New Imaging Techniques (INIT)
Department of Physics, Jaume I University, Spain.

Defence: 04.09.2026, at the Institute of Physics, University of Tartu, Estonia

The work of this dissertation was carried out at the Laboratory of Physical Optics, Institute of Physics, University of Tartu. The research work was primarily funded by the European Union's Horizon 2020 research and innovation program under Grant Agreement No. 857627 (CIPHR).

The work was partially supported by DP240103231 from the Australian Research Council, European Regional Development Fund project "Emerging orders in quantum and nanomaterials" (TK134), the Estonian Research Agency (PRG753), and partially supported by the project "Center of Nanomaterials Technologies and Research" (NAMUR+ core facility project number (2014–2020.4.01.16-0123) and TT13.

The doctoral student was financially supported primarily by the Estonian national government funding, with additional support provided through the CIPHR project during the entire period of his doctoral studies.

European Union
European Regional
Development Fund

Investing
in your future

CIPHR

Australian Government
Australian Research Council

ISSN 1406-0647 (print)
ISBN 978-9908-57-253-6 (print)

ISSN 2806-2523 (pdf)
ISBN 978-9908-57-254-3 (pdf)

Copyright: Shivasubramanian Gopinath, 2026

University of Tartu Press
www.tyk.ee

CONTENTS

LIST OF PUBLICATIONS INCLUDED IN THE THESIS 8
AUTHOR'S CONTRIBUTION STATEMENT 9
ABBREVIATIONS 10
CHAPTER 1: INTRODUCTION 12
1.1 Imaging 12
1.2 Holography 13
1.3 Coded aperture imaging 15
1.4 Characteristics of imaging systems 16
1.5 Incoherent digital holography methods 17
1.5.1 Fresnel incoherent correlation holography and its evolution 17
1.5.2 Coded aperture correlation holography 19
1.5.3 Interferenceless coded aperture correlation holography 20
1.6 Computational reconstruction algorithms 21
1.6.1 Lucy Richardson algorithm 21
1.6.2 Non-linear reconstruction 22
1.6.3 Lucy-Richardson-Rosen algorithm 22
1.7 Limitations of the current state-of-the-art imaging systems 24
1.8 Limitations of LR and AR interdependency in the current state-of-the-art imaging systems 25
1.9 Multifunctional DOEs 26
1.9.1 Modulo-2π phase addition 27
1.9.2 Random multiplexing 28
1.10 Structure of the thesis 28
CHAPTER 2: MOTIVATION AND AIM OF THE THESIS 29
2.1 Research Problem and Motivation 29
2.2 Thesis contribution statement 30
2.3 Overall impact and novelty 33
CHAPTER 3: METHODOLOGY 34
3.1 TAP-GSA 34
3.1.1 Working principle of TAP-GSA 34
3.1.2 Differences between GSA and TAP-GSA 35
3.1.3 Implementation of TAP-GSA in FINCH 37
3.1.3.1 Configuration 1 – FINCH with maximum optical path difference 38
3.1.3.2 Configuration 2 – FINCH with reduced optical path difference 39
3.2 INCHIS 39
3.2.1 INCHIS-H1 40

3.2.2 INCHIS-H2 43
3.3 PEGASASS 44
3.4 PEAR-FINCH 47
CHAPTER 4: RESULTS AND DISCUSSION 52
4.1 TAP-GSA 52
4.1.1 Simulation studies 52
4.1.2 Experimental studies 55
4.1.2.1 Configuration 1 – FINCH with maximum optical path difference 56
4.1.2.2 Configuration 2 – FINCH with reduced optical path difference 60
4.1.2.3 Fabrication and testing of phase masks 64
4.2 INCHIS 66
4.2.1 Simulation studies 66
4.2.1.1 INCHIS-H1 66
4.2.1.2 INCHIS-H2 68
4.2.2 Experimental studies 70
4.2.2.1 INCHIS-H1 71
4.2.2.2 INCHIS-H2 72
4.2.3 Additional experimental studies with synthetic dot-pattern objects 74
4.2.4 Demonstration of INCHIS-H2 using passive refractive optical elements 76
4.2.5 Discussion 79
4.2.5.1 Comparison of INCHIS-H1 with existing methods 80
4.2.5.2 Anomalous axial regions 81
4.3 PEGASASS 82
4.3.1 Experimental studies 82
4.4 PEAR-FINCH 89
4.4.1 Simulation studies 89
4.4.1.1 FINCH baseline simulations 89
4.4.1.2 Focal depth of FINCH for different optical configurations 91
4.4.2 Experimental studies 92
4.4.2.1 Axial characteristics analysis for PEAR-FINCH 103
4.4.2.2 Regular Multiplane DIS 105
CHAPTER 5: CONCLUSIONS AND FUTURE PERSPECTIVES 106
5.1 Summary of the developed research 106
5.2 Challenges in the developed research 108
5.2.1 Challenges in TAP-GSA 108
5.2.2 Challenges in INCHIS 109

5.2.3 Challenges in PEGASASS 109
5.2.4 Challenges in PEAR-FINCH 109
5.3 Applications of the developed research 110
5.4 Future perspectives of the developed research 110
RESEARCH HIGHLIGHTS 112
KOKKUVÕTE (EESTI KEELES) 116
ACKNOWLEDGEMENTS 119
REFERENCES 121
CHAPTER 6: ATTACHED PUBLICATIONS 129
CURRICULUM VITAE (IN ENGLISH) 201
ELULOOKIRJELDUS (EESTI KEELES) 206

LIST OF PUBLICATIONS INCLUDED IN THE THESIS

I. **S. Gopinath**, A. Bleahu, T. Kahro, A. S. John Francis Rajeswary, R. Kumar, K. Kukli, A. Tamm, J. Rosen, and V. Anand, "Enhanced design of multiplexed coded masks for Fresnel incoherent correlation holography," Sci. Rep. **13**, 7390 (2023). https://doi.org/10.1038/s41598-023-34492-2

II. **S. Gopinath**, A. S. John Francis Rajeswary, and V. Anand, "Sculpting axial characteristics of incoherent imagers by hybridization methods," Opt. Lasers Eng. **172**, 107837 (2024). https://doi.org/10.1016/j.optlaseng.2023.107837

III. **S. Gopinath** and V. Anand, "Post-ensemble generation with Airy beams for spatial and spectral switching in incoherent imaging," Opt. Lett. **49**, 3247–3250 (2024). https://doi.org/10.1364/OL.522319

IV. **S. Gopinath**, J. Rosen, and V. Anand, "Axial resolution post-processing engineering in Fresnel incoherent correlation holography," J. Phys. Photonics **8**, 015041 (2026). https://doi.org/10.1088/2515-7647/ae38ae

AUTHOR'S CONTRIBUTION STATEMENT

Details of the author's contributions to the research papers included in this thesis are summarized below, with Roman numerals corresponding to the publication list.

Publications I–IV: The author actively participated in all scientific discussion meetings throughout the projects. The author performed optical experiments in the laboratory, recorded and processed experimental data, performed computational image reconstruction, and prepared all experimental figures. In addition, the author contributed to the preparation of experimental plots (in **Publications II–IV**). The author was involved in manuscript preparation, including drafting initial versions of manuscripts and preparing response and revision documents during the peer-review process.

The author also contributed to the initial simulations in **Publications I, II, and IV**. In **Publication I**, the author contributed to the design of phase masks for fabrication. In **Publication II**, the author prepared supplementary materials, including figures and videos, and contributed to the writing content. In **Publication IV**, the author contributed to preparing the supplementary file and served as the corresponding author, responsible for managing the manuscript submission process, communicating with the journal editors, and coordinating revisions until final publication.

ABBREVIATIONS

2D	–	two dimensional
3D	–	three dimensional
ABN	–	average background noise
AR	–	axial resolution
CAFIR	–	coded aperture with FINCH intensity responses
CAI	–	coded aperture imaging
CDH	–	coherent digital holography
CI	–	computational imaging
CIPHR	–	computational imaging and processing in high resolution
COACH	–	coded aperture correlation holography
CPM	–	coded phase mask
DIS	–	direct imaging systems
DOE	–	diffractive optical element
DoF	–	degrees of freedom
FD	–	focal depth
FINCH	–	Fresnel incoherent correlation holography
FoV	–	field of view
FZP	–	Fresnel zone plate
GDSII	–	graphic design system II
I-COACH	–	interferenceless coded aperture correlation holography
IDH	–	incoherent digital holography
IIS	–	indirect imaging systems
INCHIS	–	incoherent hybrid imaging system
LED	–	light-emitting diode
LR	–	lateral resolution
LRA	–	Lucy-Richardson algorithm
LRRA	–	Lucy-Richardson-Rosen algorithm
MATLAB	–	matrix laboratory
MURA	–	modified uniform redundant array
NA	–	numerical aperture
NLR	–	non-linear reconstruction
OH	–	object hologram
OID	–	object intensity distribution
OSH	–	optical scanning holography
PEAR-FINCH	–	post-engineering of axial resolution in Fresnel incoherent correlation holography

PEGASASS – post-ensemble generation with Airy beams for spatial and spectral switching
PM – polarization multiplexing
PSH – point-spread hologram
PSF – point-spread function
RM – random multiplexing
SLM – spatial light modulator
SNR – signal-to-noise ratio
SOH – synthetic object hologram
SOID – synthetic object intensity distribution
SPSF – synthetic point spread function
SPSH – synthetic point spread hologram
SR – spectral resolution
SSIM – structural similarity index measure
TAP-GSA – transport of amplitude into phase based on the Gerchberg-Saxton algorithm
TR – temporal resolution
URA – uniform redundant array
UT – University of Tartu

CHAPTER 1: INTRODUCTION

1.1 Imaging

Imaging is the process of creating a visual representation of an object or event. It is easier to understand the visual information, as the ancient saying goes, 'a picture is worth a thousand words.' Imaging has become an essential tool not only in daily life but also in diverse fields of science, engineering, and medicine. From the invention of photography in the 19th century to the development of *computational imaging* (*CI*) and artificial intelligence in the 20th century, imaging technologies have continuously transformed the way we perceive and understand the world. Imaging systems such as smartphone cameras, closed-circuit television cameras, web cameras, microscopes, telescopes, etc., belong to the class of *direct imaging systems* (*DIS*), in which the image of an object is formed in a single step onto an image sensor by a lens system. The schematic representation of the DIS is shown in **Figure 1(a)**.

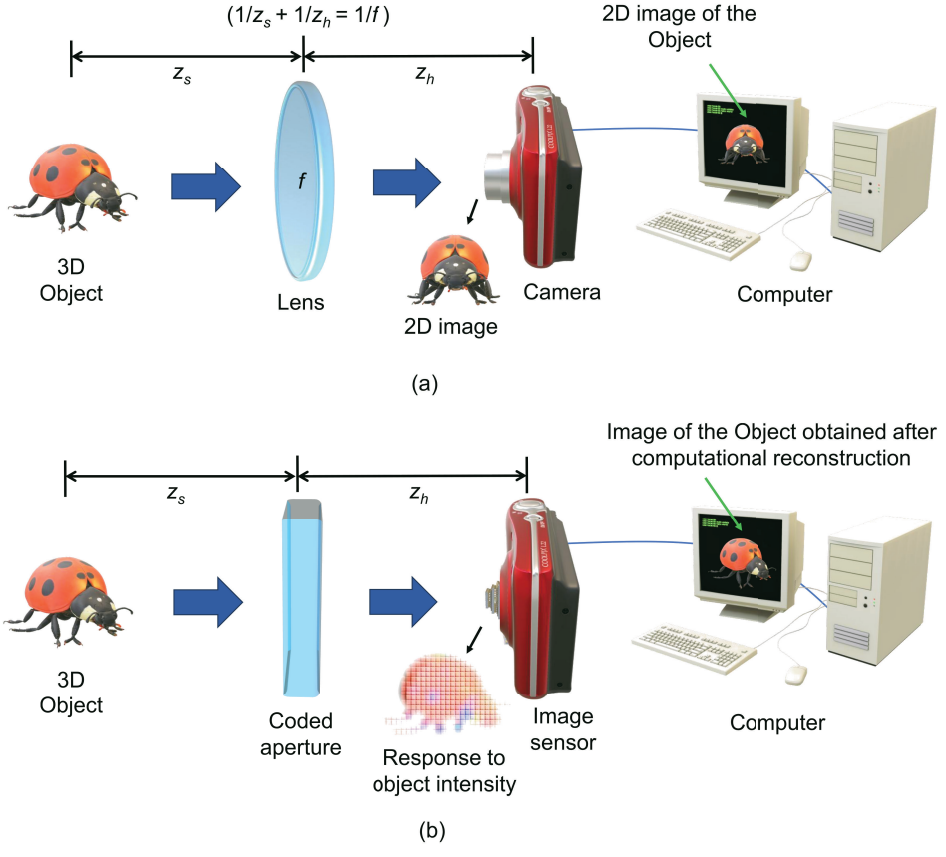

Figure 1. Schematic representation of **(a)** DIS and **(b)** IIS. z_s and z_h are object and recording distances. f is the focal length of the lens.

DIS are typically simple and robust. However, they suffer from various limitations, such as low information bandwidth, fixed imaging characteristics, and the ability to capture only *two-dimensional* (*2D*) spatial information of the object. In contrast, *indirect imaging systems* (*IIS*) involve at least two steps: optical recording and computational reconstruction [1]. IIS is an umbrella term that includes coherent and incoherent digital holography [1–10] and *coded aperture imaging* (*CAI*) [11–15]. The schematic representation of one of the methods of IIS (CAI) is shown in **Figure 1(b)**. IIS offers several advantages over DIS, including advanced capabilities such as *three-dimensional* (*3D*) imaging, super-resolution, and flexible imaging characteristics. Specifically, CAI requires minimal experimental resources, including a lesser number of low-cost optical components.

1.2 Holography

Digital holography can be broadly classified into two types: *coherent digital holography* (*CDH*) and *incoherent digital holography* (*IDH*) [1–10]. The schematic representations of the CDH and IDH are shown in **Figures 2(a) and 2(b)**, respectively. The distinction between the above two lies in the coherence properties of the light sources used and the corresponding nature of object information captured. CDH employs highly coherent light sources, such as lasers, which exhibit high spatial and temporal coherence, ensuring that the object and reference beams maintain a stable phase relationship and produce a well-defined interference pattern on the image sensor, called a coherent hologram. In CDH, the light from the object is interfered with a reference wave, derived from the same source, to create a coherent hologram. In the hologram, both the amplitude and the phase information of the object wavefront are encoded. The hologram is then processed using computational reconstruction algorithms, such as numerical back-propagation, to retrieve the object's 3D information. In contrast, IDH employs a spatially incoherent and temporally coherent light source, such as *light-emitting diodes* (*LEDs*). In IDH, the 3D location information of an object is recorded by the self-interference of light waves originating from the same object point. Due to the lack of spatial coherence, the light emitted from one object point cannot interfere with the light emitted from another point. However, light from every object point, even with incoherent illumination, is coherent with respect to itself and therefore can coherently interfere. Both CDH and IDH have advantages and disadvantages depending upon the application. CDH can retrieve phase information, which is crucial for quantitative phase imaging, whereas IDH can retrieve only the phase information corresponding to the location information. However, for certain applications, such as fluorescence imaging involving fluorescence emission mimicking spatially incoherent illumination, IDH is useful. Considering that most natural light sources in space and in everyday life are incoherent, IDH has a broader range of applicability than CDH. In the above cases, where 3D phase information is not required, CDH faces several challenges, including speckle noise and edge effects. In this doctoral research, all theoretical and experimental investigations are limited to spatially incoherent, quasi-monochromatic illumination, and coherent light sources are not employed.

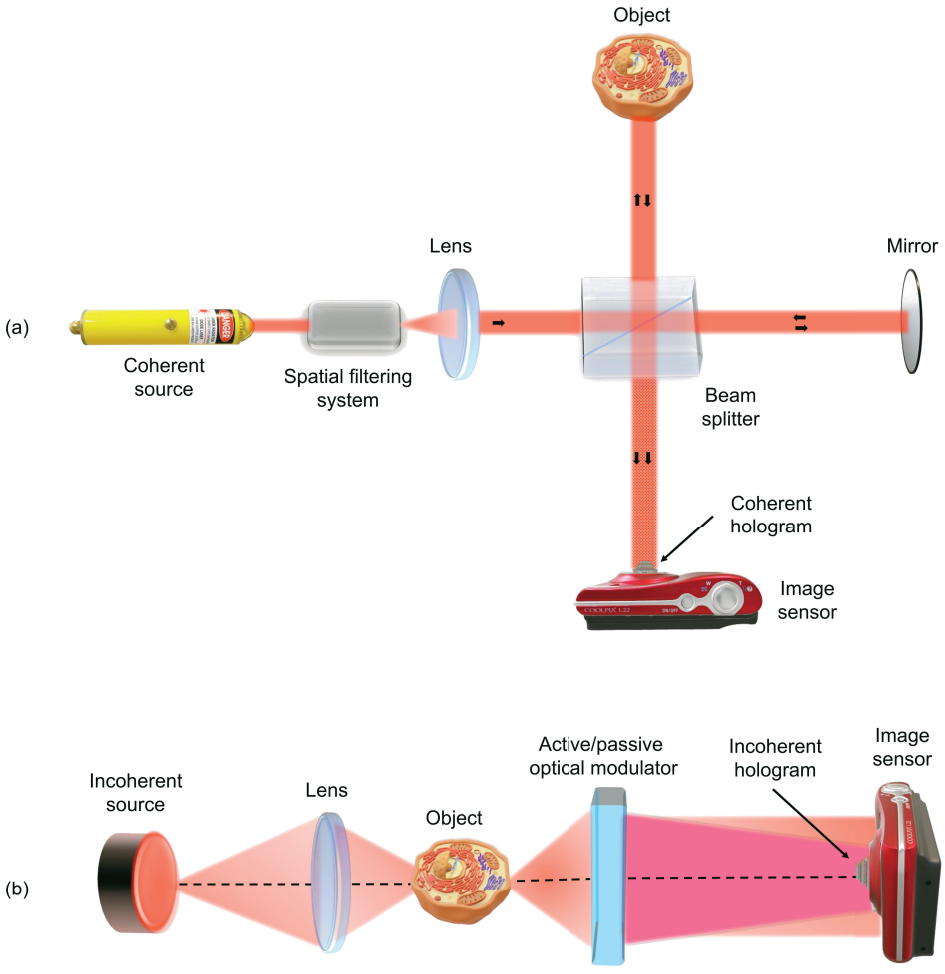

Figure 2. Schematic representation of **(a)** CDH and **(b)** IDH.

1.3 Coded aperture imaging

CAI is an innovative IIS that has played a transformative role in the development of new imaging technologies, while also addressing limitations of DIS [11–15]. One of the main challenges in DIS is that it requires lenses or reflective concave mirrors for imaging; therefore, extending DIS to non-visible areas of the electromagnetic spectrum is challenging.

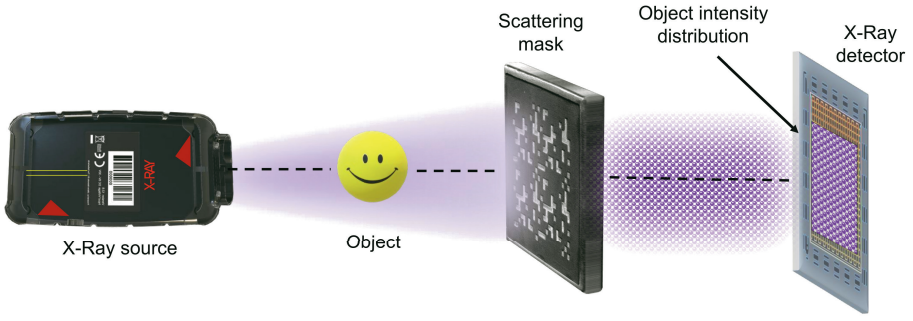

Figure 3. Schematic representation of the first version of the CAI.

While there has been significant improvement in advanced manufacturing technologies in recent years, they are not yet fully developed for the invisible regions of the electromagnetic spectrum. Unlike DIS, CAI belongs to IIS and involves two steps, similar to CDH and IDH: an optical recording step and a computational reconstruction step [11, 12]. The schematic representation of the first version of CAI is shown in **Figure 3**. In CAI, light from an object is modulated by a scattering mask, and the *object intensity distribution* (*OID*) is recorded and processed in the computer using the *point spread function* (*PSF*) recorded using a point object (under identical conditions) using a matched filter [11, 12, 16, 17]. However, in the early studies of CAI by Dicke and Ables, and in subsequent research, reconstructing the object image resulted in significant reconstruction noise. To address this challenge, Fennimore and Cannon introduced the concept of the *uniformly redundant array* (*URA*) in 1978 [17]. The URA provided a deterministic, non-random mask pattern that ensured uniform encoding of object information across the aperture. This innovation marked a breakthrough in CAI, making it more practical and efficient. Following the successful development of URA, Gottesman and Fenimore developed the *modified uniformly redundant array* (*MURA*), which enables the design of a coded aperture mask at the user's choice to match their particular detector [18]. In addition to coded aperture masks, diffractive masks, such as Fresnel zone plates (FZPs), have also been used in CAI for imaging with incoherent radiation, including X-rays and gamma rays. Barrett and Horrigan developed the theoretical framework for FZP-based gamma-ray imaging [19]. Then, Gehm *et al.* demonstrated a single-shot compressive spectral imaging system capable of reconstructing a 3D spectral data cube consisting of 2D space and spectrum [20]. After some years, Tsai and Brady demonstrated a CAI system capable of simultaneously capturing spectral and

polarization information in a single camera shot, significantly enhancing multi-dimensional imaging capabilities [21]. Overall, CAI provides a powerful framework for extending imaging capabilities beyond the fundamental limitations of DIS. CAI has become a cornerstone of modern CI and a key enabler of advanced methods in spectral, polarization, and biomedical imaging applications.

1.4 Characteristics of imaging systems

The performance of any imaging system is determined by several fundamental parameters such as *lateral resolution* (*LR*), *axial resolution* (*AR*), *spectral resolution* (*SR*), *temporal resolution* (*TR*), *field of view* (*FoV*), *signal-to-noise ratio* (*SNR*), etc. In any imaging system, whether DIS or IIS, careful consideration of these parameters is crucial for optimizing system design for specific applications. Among these parameters, AR and LR are the most critical ones, as they directly determine the spatial discriminative capability of the imaging system. AR refers to the ability to discriminate between two points along the longitudinal direction (depth). It quantifies the expected degree of blur when one plane is imaged from another. LR refers to the ability to discriminate between two points along the transverse direction, and it sets the minimum resolvable feature size. Both AR and LR depend upon the *numerical aperture* (*NA*) of the imaging system. The relations are: $\mathrm{AR} \sim \lambda/\mathrm{NA}^2$ and $\mathrm{LR} \sim \lambda/\mathrm{NA}$, where λ is the illumination wavelength, and $\mathrm{NA} \sim D/2f$, with D and f denoting the diameter and focal length of the lens, respectively. It is possible to set the LR and AR by selecting an appropriate NA of the system. However, because both parameters are fundamentally coupled through NA, independent tuning of AR without affecting LR is not possible in DIS [22]. SR refers to an imaging system's ability to distinguish information across different wavelengths. In conventional systems, it can be set either by the color filters in the image sensor or by spectrometers governed by diffraction or interference phenomena [23–25]. TR refers to an imaging system's ability to resolve events separated in time. TR is determined primarily by the image sensor's frame rate [26]. TR also depends on the number of camera shots needed to capture a scene: inline IDH and CDH systems that require multiple shots to remove twin-image and bias noise exhibit a low TR. The FoV represents the area of an object that can be captured by an image sensor in a single shot. FoV fundamentally depends on the sensor size and the system's magnification, and is inversely related to LR [27]. The SNR is another crucial parameter, which, as the name suggests, measures the ratio between signal and noise [28]. This SNR depends on various parameters, such as illumination strength, the imaging system's light throughput, exposure time, detector noise, ambient light, etc. The above parameters define the performance of any imaging system. The central challenge in imaging science lies in not only achieving optimal values of the above parameters but also engineering systems that can flexibly control these parameters, ideally decoupling them to allow independent tuning, a goal that DIS cannot achieve so far.

1.5 Incoherent digital holography methods

The conceptual foundations of IDH emerged in the late 1960s when Bryngdahl and Lohmann demonstrated that holographic information could be obtained without global spatial coherence by exploiting local self-interference between correlated wavefront copies originating from each object point. This insight overturned the prevailing assumption that coherence was a fundamental requirement for holography and laid the theoretical groundwork for later IDH architectures. The first practical realization of IDH was achieved with the invention of *optical scanning holography* (*OSH*) by Poon in 1985 [29, 30]. OSH replaced spatial interference with time-domain heterodyne interference by scanning a temporally modulated interference pattern across the object and recording the scattered light using a single-point detector. However, OSH was challenging to implement due to the requirement for a pixel-by-pixel scanning procedure and could not replace DIS. The motivation for IDH was fulfilled with the development of *Fresnel incoherent correlation holography* (*FINCH*) by Rosen and Brooker in 2007, in which the entire object or scene can be recorded using a few camera shots [31, 32]. FINCH laid the foundations for modern-day IDH implementations.

1.5.1 Fresnel incoherent correlation holography and its evolution

The schematic representation of the first version of FINCH, implemented using the *random multiplexing* (*RM*) method, is shown in **Figure 4**. In FINCH, light from each object point is split into two beams using randomly multiplexed diffractive lenses with different focal lengths. These two beams are differently modulated and interfere with one another to form a self-interference hologram on the image sensor.

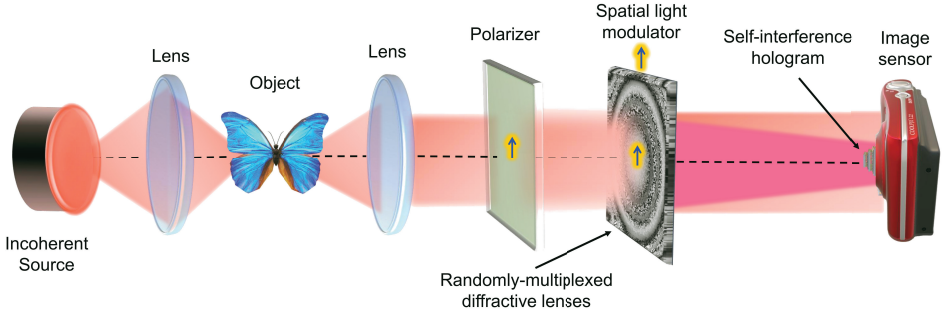

Figure 4. Schematic representation of the first version of the FINCH. The blue arrow denotes the polarization orientation and direction of the active axis of the SLM.

Since FINCH was developed as an inline IDH method, the recorded hologram consists of the twin-image and bias noises. To remove the above noises, in FINCH, at least three phase-shifted *object holograms* (*OHs*) are recorded and digitally superposed with appropriate phase values to obtain a complex hologram. The complex hologram is then reconstructed by Fresnel back-propagation, yielding a 3D image of the object free of twin-image and bias noises. FINCH implementations typically involve an active optical element, such as a *spatial light modulator* (*SLM*), to generate the required three different phase modulations between the interfering beams. Compared with DIS, FINCH exhibits a higher LR and an extended *focal depth* (*FD*) for the same NA [33]. The ability of FINCH to perform 3D imaging without mechanical scanning makes it highly attractive for various applications, outperforming both DIS and traditional OSH approaches [34–36]. In particular, FINCH-based fluorescence holographic microscopy has demonstrated significant advantages for imaging biological specimens, offering enhanced resolution and robustness [37].

Despite its unique advantages, the original FINCH configuration encountered several practical challenges, including low SNR due to scattering noise from the RM approach, low TR due to multiple phase-shifted recordings, and low AR [31]. To address these challenges, many solutions have been proposed over the years. To enhance SNR, *polarization multiplexing* (*PM*) was introduced as an alternative method for generating the two object waves [38]. In this approach, instead of randomly multiplexed diffractive lenses, a single diffractive lens is displayed on the SLM. A polarizer oriented at 45° with respect to the SLM's active axis is placed between the object and the SLM. This configuration allows approximately half of the object wave's intensity to be modulated by the SLM while the remaining portion remains unmodulated. A second polarizer is introduced after the SLM, also aligned at 45°, to enable interference between the modulated and unmodulated waves at the image sensor. This technique effectively suppressed reconstruction noise arising from light scattering by randomly multiplexed diffractive lenses used in the original FINCH setup. However, this improvement comes at the cost of reduced light throughput, as using two polarizers inherently limits the transmitted intensity. Alternative strategies to enhance light efficiency include geometric-phase lenses, which avoid polarization losses while maintaining high interference contrast [39]. The TR of FINCH was improved through spatial and polarization multiplexing techniques [40–43]. Further advancements include the introduction of dual-SLM FINCH configurations and computational optical methods, which enable optical sectioning and confocal-like imaging capabilities [44, 45]. A hybrid FINCH method was developed by changing one of the two beam modulations from quadratic phase to a spiral phase to achieve edge enhancement in reconstructed objects [46]. These developments and applications have collectively elevated FINCH into a versatile, high-resolution, and scanning-free incoherent imaging platform capable of superior 3D imaging performance, high SNR, and single-camera-shot acquisition [36].

1.5.2 Coded aperture correlation holography

Coded aperture correlation holography (*COACH*) is another unique method introduced in 2016 [47]. For the first time, in COACH, the principles of IDH and CAI were combined within a single framework. Conceptually, COACH evolved from FINCH, sharing its self-interference foundation but incorporating key modifications that enhance its flexibility and computational capability. The schematic representation of the COACH is shown in **Figure 5**. In COACH, the light from the object is split into two beams: one is modulated by a quasi-random coded phase mask (CPM), while the other remains unmodulated. Since both beams originate from the same object point, they are mutually coherent and can interfere to form a self-interference hologram. As in FINCH, COACH requires the recording of a minimum of three phase-shifted OHs, which are numerically superposed to yield a complex OH. The phase-shifting step is used to eliminate twin-image and bias terms during reconstruction.

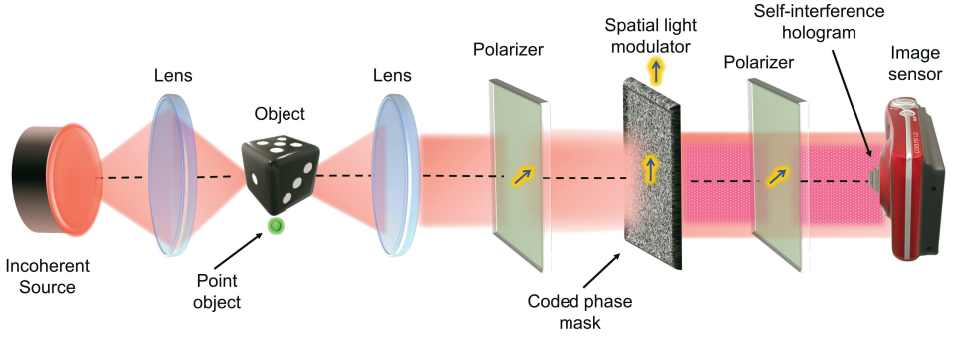

Figure 5. Schematic representation of the COACH. The blue arrow denotes the polarization orientation and direction of the active axis of the SLM.

An additional step is performed in COACH: a distinct training stage that involves recording a library of *point spread holograms* (*PSHs*) under identical conditions, using a point object placed at various axial locations with three different phase shifts, as in FINCH. The three phase-shifted PSHs are superposed to obtain a complex PSH for each axial location. Once this PSH library is constructed, the 3D image of the object is reconstructed by performing numerical cross-correlation between the OH and the PSH library [16]. Compared with FINCH, COACH exhibits AR and LR comparable to DIS. Also, COACH exhibits certain limitations. Its reconstruction noise is higher than that of FINCH due to random phase modulation. Despite these challenges, COACH remains a significant advancement in holographic imaging, offering a versatile bridge between IDH and CAI. COACH has found applications in optical security [48]. Over time, FINCH has been successfully integrated within the CAI framework [49, 50]. In these approaches, a PSH library is pre-recorded at various possible axial locations as a calibration step, without any phase shifts, and stored digitally. For 3D imaging, a single FINCH hologram is recorded and processed with the PSH library using a deconvolution algorithm [51, 52]. FINCH as CAI enables single-shot 3D imaging with an improved AR.

1.5.3 Interferenceless coded aperture correlation holography

In 2017, *interferenceless COACH* (*I-COACH*) was derived from COACH [53]. It was discovered that the 3D location information of an object is present not only in the phase but also in the amplitude of the scattered wave in COACH. Therefore, two-beam interference is not needed in COACH, unlike FINCH, to record 3D information. This discovery enabled the capture of 3D object information without the need for two-beam interference. The schematic representation of the I-COACH is shown in **Figure 6**. In I-COACH, light from an object is modulated by three independent quasi-random CPMs, and the corresponding OHs are recorded directly by the image sensor. The recorded OHs are then projected into the complex space by applying three distinct phase shifts and combined into a complex hologram. The 3D information of the object is retrieved computationally by processing the object's complex hologram with a pre-acquired library of complex-valued PSHs corresponding to different depths, using a matched filter [16]. Unlike IDH methods, I-COACH can capture the entire 3D information of an object scene with a single camera shot, if a better deconvolution method is used. The elimination of the interference requirement leads to a simpler optical configuration, reduced sensitivity to environmental instabilities, lower optical-power demand, and improved SNR. I-COACH can be considered an extension of CAI, in which PSH is recorded at multiple planes rather than at a single plane. This interference-free 3D imaging capability of I-COACH makes it an attractive candidate to replace existing IDH methods across different applications.

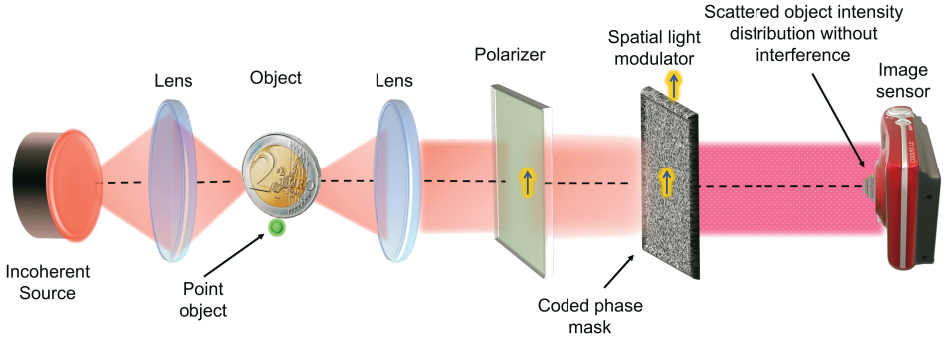

Figure 6. Schematic representation of the I-COACH. The blue arrow denotes the polarization orientation and direction of the active axis of the SLM.

Among the various IDH and CAI techniques discussed previously, FINCH and I-COACH occupy a central position due to their ability to perform 3D imaging with high flexibility in system design and computational reconstruction. FINCH represents a widely adopted IDH framework, while I-COACH extends the CAI platform to interferenceless 3D incoherent imaging. Owing to their complementary strengths and adaptability, all the imaging techniques developed in this doctoral research are based on FINCH and I-COACH architectures, with a particular focus on engineering image resolutions through post-recording.

1.6 Computational reconstruction algorithms

Computational reconstruction algorithms are an essential component of IIS for retrieving the object information from the recorded OIDs. In in-line IDH systems, image reconstruction is typically performed by numerically back-propagating the complex OH generated from the recorded phase-shifted OHs [31]. In contrast, early CAI systems utilized the matched filter method for image reconstruction [11, 12, 16]. Over the years, several iterative and non-iterative computational reconstruction methods have been developed to enhance SNR and image quality in various imaging domains. Among these, notable examples include the *Lucy-Richardson algorithm* (*LRA*) [54, 55], *nonlinear reconstruction* (*NLR*) [51], and the *Lucy-Richardson-Rosen algorithm* (*LRRA*) [56]. The above reconstruction algorithms have been widely investigated. It has been found that the recently developed LRRA outperforms many existing algorithms across a wide range of deterministic and random CPMs, making it a highly versatile reconstruction algorithm [57]. Given its superior performance and proven adaptability, the LRRA has been employed for many CAI, I-COACH, and FINCH systems [50, 58, 59]. The above-mentioned reconstruction algorithms are discussed further in the following sub-sections 1.6.1, 1.6.2, and 1.6.3.

1.6.1 Lucy Richardson algorithm

The LRA developed by Richardson and Lucy is a well-established iterative deconvolution technique widely used in CI systems for image restoration [54, 55, 60]. It is particularly effective for reconstructing images degraded by blurring and other system-induced distortions. In the LRA, the reconstruction process begins with an initial estimate of the object, R^1, which is iteratively updated to minimize the difference between the recorded image and the forward-convolved estimate. Specifically, the PSF is convolved with the current estimate of the object, and the ratio between the recorded OID and the forward-convolved result is computed. This ratio is then backward correlated with the PSF and multiplied by the current estimate to produce an improved reconstruction. The iterative process continues until convergence is achieved, typically when the object's maximum-likelihood solution is obtained. The LRA is mathematically expressed as

$$R^{n+1} = R^n \left\{ \frac{OID}{R^n \otimes PSF} \otimes PSF' \right\}, \tag{1}$$

where $\otimes$ denotes a 2D convolutional operator, and PSF' denotes the complex conjugate of PSF. By an iterative approach, LRA enhances the fidelity of the reconstructed image. An improved version of LRA was reported in [61]. Owing to its effectiveness, LRA has been widely applied in a range of imaging fields, including optical coherence tomography, fluorescence microscopy, astronomical imaging, and thermal imaging, where accurate restoration of fine details is essential [61, 62]. However, despite its success, LRA has certain limitations. The

number of iterations required by LRA for severely distorted images can reach thousands, resulting in longer reconstruction times. Consequently, LRA may not be suitable for real-time imaging of events.

1.6.2 Non-linear reconstruction

Following the development of I-COACH, a new computational algorithm, NLR, was developed that unified all correlation-based reconstruction methods, such as matched filter, phase-only filter, and inverse filter, under a single roof. The NLR was first demonstrated in conjunction with I-COACH for single-camera-shot 3D imaging, achieving superior reconstruction performance compared to matched filter, phase-only filter, and inverse filter [51]. In this implementation, NLR was applied to I-COACH imaging reconstructions under different noise conditions: reflection (higher noise) and transmission (lower noise) imaging configurations. Experimental results demonstrated that NLR significantly improved image contrast, edge sharpness, and overall reconstruction fidelity relative to linear cross-correlation methods. However, it was also observed that reconstruction noise increased with the scattering rank of the CPMs, indicating that reconstruction stability depends on the statistical properties of the phase modulation. In the NLR framework, the reconstructed image of the object is expressed as,

$$R = \Im^{-1}\left\{\left|\widetilde{PSF}\right|^{\alpha} exp\left[j \cdot arg\left(\widetilde{PSF}\right)\right] \left|\widetilde{OID}\right|^{\beta} exp\left[-j \cdot arg\left(\widetilde{OID}\right)\right]\right\}, \qquad (2)$$

where $\Im^{-1}\{\cdot\}$ denotes the inverse Fourier transform operator, $\widetilde{PSF}$ and $\widetilde{OID}$ denotes the Fourier transforms of PSF and OID; $arg\,(\cdot)$ refers to the phase of a complex quantity. The parameters α and β are varied between –1 and 1 until the entropy of the reconstructed image is minimized. Because of its flexibility, NLR was applied to the next versions of I-COACH and IDH methods implemented in the CAI framework [63].

1.6.3 Lucy-Richardson-Rosen algorithm

In 2022, LRRA was introduced by combining NLR and the LRA [56]. In LRA, reconstruction involves a forward convolution $R^n \otimes PSF$, followed by a backward correlation between the ratio (recorded OID and the forward-convolved result) and the PSF.

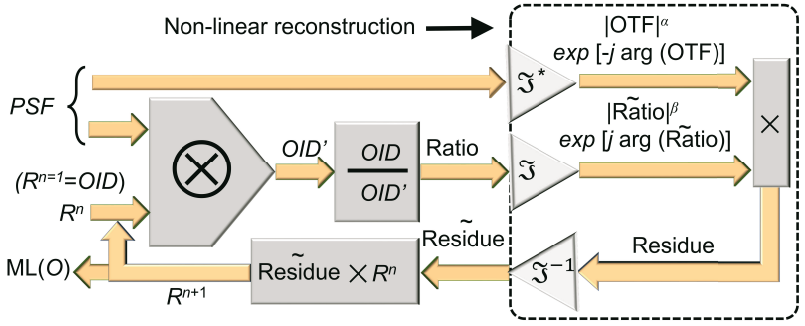

Figure 7. Schematic representation of LRRA. O – object; ML – maximum-likelihood solution of object; OTF – optical transfer function; × – element by element product; n – number of iterations; ⊗ – 2D convolutional operator; $\mathfrak{F}$ – Fourier transform, $\mathfrak{F}^*$ – complex conjugate operation following a Fourier transform, $\mathfrak{F}^{-1}$ – inverse Fourier transform, R^n and $R^{(n+1)}$ are the n^{th} and $(n+1)^{\text{th}}$ solutions, OID was used as the initial guess solution $R^{n=1}$, ~ Fourier transform of a variable.

In the LRRA, the forward convolution step remains unchanged, but the backward correlation is replaced with the NLR step. This approach accelerates convergence, enhances contrast, and reduces background noise, yielding reconstructions with higher SNR and improved fidelity compared to those of LRA and NLR. The schematic representation of LRRA is shown in **Figure 7**. The algorithm iteratively refines the relationships among the object, PSF, and OID. The reconstruction process begins with an initial guess of the object, typically the recorded intensity distribution itself ($R^{n=1} = OID$). It is convolved with the PSF, and the resulting matrix is compared with OID by calculating the ratio. This ratio is correlated with PSF using NLR to produce a residue, and is multiplied by the previous estimate $R^{n=1}$. The process is repeated until the solution converges to a non-changing value.

Recent studies have investigated the performance of LRRA across diverse imaging scenarios and found that it outperforms many existing reconstruction methods [57, 64]. The first version of I-COACH is primarily employed with random CPMs [53]. After a few years, the applicability of I-COACH has been extended to deterministic optical fields, such as axicon, spiral lens, cubic-phase, random lens, and spiral axicon [57]. These structured beams exhibit unique 3D propagation characteristics, such as nondiffracting and self-healing behaviour, but they lack a conventional point focus and are therefore unsuitable for DIS. By tailoring the CPM design and applying LRRA reconstruction, I-COACH successfully transferred the exotic propagation characteristics of these optical fields into imaging applications in a single camera shot. Also, in [57], LRRA was, for the first time, applied to enhance the quality of medical images obtained through colonoscopy and cone-beam computed tomography using a synthetic PSF, and it was found that LRRA performs better than other reconstruction algorithms. In [64], LRRA was demonstrated for the first time on smartphone-based imaging under white-light illumination, in both invasive and non-invasive modes. It was employed to deblur images captured with low-NA lenses exhibiting spatial and

spectral aberrations. LRRA produced markedly improved deblurring results compared with other reconstruction algorithms. Furthermore, its reconstructions were evaluated using several deep-learning-based classification networks trained on blurred image datasets. In all tested cases, LRRA reconstructions yielded higher classification accuracy than those obtained with LRA or NLR, confirming LRRA's superior image-restoration capability. Collectively, these developments establish the LRRA as a powerful and versatile reconstruction algorithm. By integrating the LRA with the adaptive non-linearity of NLR, LRRA achieves fast convergence, high robustness, and low noise, making it a promising tool for advanced IDH, CAI, and CI systems. Given its demonstrated advantages over existing reconstruction algorithms in convergence speed, noise suppression, and reconstruction quality, LRRA is well-suited for object recovery in incoherent imaging applications. Accordingly, LRRA is employed as the principal reconstruction algorithm for the imaging techniques developed in this doctoral research. Beyond the notable reconstruction algorithms discussed above, namely the LRA, NLR, and LRRA, in most recent years, a few computational non-linear and hybrid reconstruction algorithms have been reported to further improve the performance of IDH and CAI systems [52, 60, 65]. These developments represent the ongoing evolution of image reconstruction algorithms, marking significant progress in image restoration.

1.7 Limitations of the current state-of-the-art imaging systems

Despite significant advancements made in imaging technologies, DIS, IDH, and CAI, current state-of-the-art imaging systems continue to suffer from fixed imaging characteristics. Recalling the relation between AR and LR, where tuning one characteristic by changing NA results in changing the other. Similarly, there are many such interdependencies among imaging characteristics that limit the capabilities of imaging systems. For example, the inverse relation between FoV and LR. Lensless CI systems have been developed to relax the FoV-LR interdependence and achieve an improved space-bandwidth product [66]. Another challenge with DIS is the need for the corresponding sensing device to detect that parameter. For instance, a color image sensor is needed for color imaging, a fast camera for recording fast events, and a large image sensor for recording large-area objects. CI modalities have also been proposed and demonstrated to record fast transient events beyond the limits of the image sensor [67]. Similarly, CI techniques for extending the FoV beyond the limits set by the image sensor have been reported [68, 69]. Numerous super-resolution techniques, such as structured illumination [70], stimulated-emission-depletion [71], and stochastic optical reconstruction microscopy [72], have been developed to overcome the LR limits set by the NA. In FINCH, the LR was improved beyond the limits defined by the NA using structured illumination [73] and scattering [74].

1.8 Limitations of LR and AR interdependency in the current state-of-the-art imaging systems

A fundamental challenge shared by DIS, IDH, and CAI is the lack of flexibility in independently controlling key imaging parameters, particularly LR and AR. In conventional imaging architectures, LR and AR are intrinsically coupled through the NA, such that modifying one parameter inevitably affects the other. This interdependence limits the adaptability of imaging systems for applications that require customized imaging characteristics. For example, when a thick and sparse sample is imaged, a high LR and low AR can be useful as the entire sample can be recorded within a few camera shots. To address these limitations, several IDH and CAI imaging technologies have been proposed to decouple AR and LR. One such approach involves hybridization, where the architectures of multiple imaging modalities are combined to exploit their complementary strengths. In 2017, a hybrid imaging system combining the CPMs of FINCH and COACH was demonstrated, enabling AR and LR tunability between the LR and AR limits of both methods [75]. Subsequently, the *coded aperture with FINCH intensity responses* (*CAFIR*) framework was introduced in 2021 to achieve the high LR of FINCH together with the AR of COACH through CPM engineering [76]. However, neither of these hybridization schemes allowed independent tuning of AR without affecting LR.

Beyond hybridization approaches, PSF engineering using an ensemble of spatially structured beams has emerged as another way to achieve AR tunability without affecting LR in real-time. In 2022, a CI technique demonstrated tuning of AR independent of LR using an ensemble of Bessel beams that generated Bessel speckles [77]. Increasing the number of Bessel beams increased the randomness and shortened the axial correlation length, thereby improving AR, while the lateral correlation length remained unaffected, retaining the same LR. However, in this study, a high reconstruction noise was observed. Later, two I-COACH-based techniques were proposed that used a sparse ensemble of Airy and self-rotating beams to achieve tunable AR with a constant LR [58, 78]. Airy beams naturally follow curved propagation paths in 3D space. When multiplexed randomly, they exhibit random transverse shifts with respect to one another, producing unique intensity distributions at different depths. As the number of Airy beams increases, the AR improves and approaches the limit set by the NA. Unlike Airy beams, self-rotating beams rotate with depth. This property provides a more uniform intensity distribution across depths and exhibits lower reconstruction noise compared to Airy beams.

Rai and Rosen later introduced an innovative CAI method to vary AR independent of LR by designing advanced CPMs [79]. Their design combined three distinct *diffractive optical elements* (*DOEs*), a diffractive spherical lens, a radial quartic phase function, and a quasi-random CPM into a single multiplexed CPM architecture. Each DOE served a unique purpose: the diffractive spherical lens determined the initial axial point of the sub-volume in imaging space, the radial quartic phase function defined the length of the imaged sub-volume, and the

quasi-random CPM was utilized for digital reconstruction. By combining these three DOEs, the system could engineer the depth of field to selectively image multiple sub-volumes of a 3D scene. Experimental validation confirmed that this method enabled real-time, user-defined FD control and multi-volume imaging from a single camera shot. However, despite these advantages, their method exhibits several limitations. The design and optimization of the multiplexed CPM are complex. Moreover, the system's tunability is limited to real-time control during recording; post-recording tuning of imaging parameters remains unachieved. Additionally, combining multiple DOEs increases reconstruction noise. Although this method can tune AR without affecting LR, further advancements are needed to meet specific application requirements by simplifying the optical design and reducing reconstruction noise.

Over the years, numerous CAI-based imaging methods have been developed to engineer AR in real-time [58, 77–79]. On the other hand, in IDH, FINCH remains a robust and well-established technology that inherently provides high FD, making it well-suited for applications such as biomedical and microscopic imaging. However, despite its extensive use and proven advantages, only a single study by Nobukawa *et al*. on FD engineering may be applicable for the FINCH framework [80]. They demonstrated a bimodal IDH method capable of switching between 3D imaging and quasi-infinite-depth-of-field imaging by altering the phase mask displayed on the SLM, without changing the LR. Although their approach was not implemented in a FINCH configuration, their method can be applied to FINCH-like systems to extend the FD. While their method effectively achieved extended FD imaging, it exhibited two major limitations: the FD was fixed during recording and could not be tuned, and only one imaging mode, either 3D or quasi-infinite depth of field, could be realized in a single acquisition. Despite these significant advances [58, 77–80], a common limitation persists across all imaging methods: the inability to tune AR independently of LR post-recording, which is impossible with existing methods. In all the above methods, imaging characteristics are fixed at the time of recording, and post-recording flexibility remains unachieved.

1.9 Multifunctional DOEs

As discussed in Sections 1.5–1.8, several IDH and CAI methods have evolved to achieve new imaging capabilities. Many of these methods rely critically on multifunctional DOEs or CPMs to implement multiple beam-shaping and modulation functions within a single optical element. The performance and flexibility of these IDH and CAI systems are therefore strongly influenced by the design strategies used to realize such multifunctional DOEs. In this context, the present Section reviews commonly employed approaches for implementing multifunctional DOEs and discusses the associated challenges.

Multifunctional DOEs play a vital role in numerous modern optical technologies, including IDH, CAI, beam shaping, optical trapping, augmented reality,

and virtual reality systems [81–90]. These elements enable compact, lightweight, and highly efficient optical architectures that can perform multiple optical functions simultaneously, such as focusing, beam splitting, or generating structured light, within a single optical element. Despite their versatility, the design and fabrication of multifunctional DOEs remain highly challenging. The fundamental problem in achieving a multifunctional diffractive optical element is discussed. When two or more phase-only functions are combined, for example, $exp(j\phi_1) + exp(j\phi_2)$, the resulting function becomes complex-valued, containing both amplitude and phase variations. In principle, such modulation could be realized, but it requires simultaneous control of amplitude and phase, which is challenging in practical implementations. Most commercial SLMs, such as liquid crystal SLMs, digital mirror devices, etc., are either phase-only or amplitude-only devices. Even with advanced micro/nanofabrication methods, achieving complex-valued modulation typically requires at least two precisely spaced optical layers, which complicates alignment and reduces overall system efficiency compared with single-element configurations. To address these limitations, several strategies have been developed to combine multiple diffractive functions producing a resultant phase-only element that can be physically realized using an SLM or lithographic fabrication. Among these, two widely adopted approaches are the modulo-2π phase addition method and the RM method.

1.9.1 Modulo-2π phase addition

One of the most established approaches for combining multiple diffractive functions into a single DOE is the modulo-2π phase addition technique, expressed as $\phi_T = [\phi_1 + \phi_2]_{2\pi}$. This method is particularly effective for combining grey-scale diffractive functions [83, 85, 90], a greyscale with a binary function [87], or two binary functions [83]. The resulting element can be implemented as either a greyscale or binary DOE, achieving maximum diffraction efficiencies of approximately 1 and 0.4, respectively [91]. The above modulo-2π phase-addition method transfers the far-field intensity and phase distributions of the diffraction patterns of one function to the other. For instance, in microdrilling applications, an array of ring patterns is created by combining a Dammann grating with a diffractive axicon, and the dot patterns generated by the Dammann grating are replaced by the ring patterns of the axicon [92]. The diffraction effects of one element are intertwined with those of the other, resulting in surprising behaviours in certain cases, such as quasi-achromatic focusing of light [83, 93]. However, modulo-2π phase addition cannot create two independent functions.

1.9.2 Random multiplexing

An alternative approach for achieving multifunctionality within a single DOE is the RM method [31, 49]. In this technique, a random mask is generated, and different diffractive functions are encoded into the pixels of the random mask with a certain range of values. By selecting the ratio between the number of pixels assigned to different diffractive functions, it is possible to control the optical power splitting across the diffractive functions effectively. RM enables the coexistence of multiple diffractive functionalities within a single DOE while ensuring independence between them. This property makes RM particularly useful for designing compact, versatile diffractive systems capable of performing multiple optical operations simultaneously. Recently, RM has been used to increase the speed of singular beam generation [94]. As discussed in the earlier Sections 1.5–1.8, some of the notable IDH and CAI methods, such as FINCH [31, 49], scattered Airy beams [78], self-rotating beams [58], and depth of field engineering by Rai and Rosen [79], their implementation relies heavily on the design of multifunctional DOEs, achieved by RM or modulo-2π phase addition approaches. However, one of the challenges with the RM method is the scattering noise it generates.

1.10 Structure of the thesis

The remaining part of the thesis is organized as follows:

- **Chapter 2 – Motivation and Aim of the Thesis:** This chapter presents the motivation behind the research, defines the main objectives, and establishes the scope and significance of the study.
- **Chapter 3 – Methodology:** This chapter describes the computational optical methods and their mathematical analysis.
- **Chapter 4 – Results and Discussion:** This chapter outlines the key simulation and experimental results, followed by a detailed discussion and interpretation of the findings.
- **Chapter 5 – Conclusions and Future Perspectives:** This chapter concludes the main outcomes of the research, highlights the scientific contributions, and outlines potential directions for future work.
- **Chapter 6 – Attached Publications:** This chapter includes the published and submitted research papers that form the core contributions of this thesis.

CHAPTER 2:
MOTIVATION AND AIM OF THE THESIS

2.1 Research Problem and Motivation

From Sections 1.5–1.8 of Chapter 1, it is evident that while notable progress has been made in both IDH and CAI's current state-of-the-art imaging systems, they continue to suffer from a fundamental lack of flexibility in imaging characteristics. In particular, key imaging parameters such as AR and LR remain intrinsically coupled and are typically fixed at the time of recording. Recent studies [58, 77–79] have demonstrated AR tuning without affecting LR. All these techniques are typically limited to real-time control during recording. Moreover, the techniques reported in these studies require complex optical designs and advanced CPM architectures, and also suffer from reconstruction noise. Consequently, there exists a clear knowledge gap for an imaging framework capable of independently tuning image resolutions with high fidelity, low noise, and minimal optical complexity, with post-recording control. This post-recording flexibility is crucial for practical applications where experimental conditions cannot be altered in real-time or cases where post-recording refinement is desirable. A parallel challenge arises in the IDH, particularly in systems such as FINCH. While FINCH and its variants have demonstrated superior performance to DIS in LR and FD, no existing method has explored the post-recording tunability of imaging parameters within the FINCH framework. This limitation restricts the adaptability of FINCH-based systems to advanced imaging applications. *The primary motivation of this doctoral research is therefore to develop imaging frameworks that enable independent post-recording tunability of imaging resolutions, especially AR, without affecting LR, within a unified and computationally efficient platform applicable to both CAI and IDH systems.*

Achieving such post-recording flexibility, however, is not possible within existing IDH and CAI frameworks without addressing an important enabling challenge related to CPM design. Many advanced IDH and CAI systems rely on multifunctional CPMs that combine multiple beam-shaping or modulation functions within a single optical element. As discussed in Section 1.9, existing approaches for realizing such multifunctionality, such as RM and modulo-2π phase addition, introduce significant limitations, including scattering noise, reduced light throughput, limited independence between encoded functionalities, and increased system complexity. These limitations prevent the design of flexible imaging architectures and the realization of post-recording resolution tunability. Consequently, developing a practical, computationally efficient, and experimentally feasible method for designing multifunctional, phase-only CPMs that emulate complex-valued modulation is a prerequisite for addressing the fundamental research problem of this thesis. Motivated by this requirement, the first contribution of this doctoral research is to develop a new computational multifunctional CPM design algorithm that will serve as an enabling foundation for the subsequent development of post-recording adaptive imaging frameworks.

In summary, the overall motivation of this doctoral research is driven by two interconnected and fundamental challenges:

- The main objective of this doctoral thesis is to address the absence of imaging frameworks that enable independent and post-recording tunability of AR without affecting LR, within a unified and computationally efficient platform applicable to both CAI and IDH systems.
- A prerequisite objective, which arises from the main goal, is to overcome the lack of a universal method for designing multifunctional, phase-only DOEs or CPMs equivalent to complex-valued functions. Achieving this is essential because developing advanced CI systems that enable tunable imaging performance fundamentally requires a practical solution for generating the necessary multifunctional CPMs.

2.2 Thesis contribution statement

This doctoral research addresses the fundamental limitations in existing IDH and CAI systems by introducing a new generation of CI techniques. The thesis contributes both theoretical and experimental advancements that collectively address the identified knowledge gaps and provide solutions to the above-mentioned challenges. The key contributions and findings of this thesis research, each addressing one of the identified research problems, are summarized below:

I. *Development of Transport of Amplitude into Phase based on Gerchberg-Saxton Algorithm* (*TAP-GSA*)

   - A multifunctional CPM design algorithm based on the well-known Gerchberg-Saxton Algorithm [95], termed TAP-GSA, was developed to address the fundamental challenges in realizing complex-valued masks in CI experiments.
   - When two phase functions are summed, a complex-valued function is obtained consisting of both amplitude and phase information. TAP-GSA iteratively transfers amplitude information into phase, generating a phase-only function equivalent to a complex-valued function, which can be readily implemented with both SLMs and lithographically fabricated masks.
   - TAP-GSA was implemented in FINCH, and experimental results demonstrated ~200% improvement in light throughput compared to PM and ~150% improvement compared to RM.
   - TAP-GSA provides a universal platform for designing advanced multifunctional DOEs for beam shaping, holography, and imaging applications. It was utilized for subsequent imaging techniques developed later in this thesis.

II. *Development of Incoherent Hybrid Imaging Systems* (*INCHIS*)

- The INCHIS framework was developed to overcome the existing AR-LR interdependency in incoherent imaging systems using a hybridization approach to achieve the primary goal of the thesis. INCHIS-H1 and INCHIS-H2 introduce the capability to engineer AR independently of LR, in real-time and post-recording, respectively, within a unified CI system. In particular, to the best of our knowledge, INCHIS-H2 represents the first demonstration of post-recording AR tuning without affecting LR in the incoherent imaging domain.
- INCHIS-H1 utilizes pre-engineered hybrid CPMs generated by combining two DOEs using TAP-GSA, namely, the diffractive lens and diffractive axicon. This combination generates a spherical and a Bessel beam for every object point that self-interfere to form an incoherent hologram. The AR is tuned in real-time between the AR limits of the lens and the axicon by controlling the relative strength of the two CPMs in the hybrid CPM.
- In INCHIS-H2, a scene is collinearly recorded using two passive refractive/diffractive optical elements, a lens, and an axicon, and combined. The AR is engineered post-recording by applying different weights to the recorded intensity distributions before combining them.
- In both INCHIS-H1 and INCHIS-H2, a library of PSFs is recorded at all possible axial locations and processed under identical conditions. The object information was reconstructed by processing the corresponding PSFs and OIDs using LRRA.
- INCHIS offers LR independent AR control, improved SNR, and reduced optical complexity, making it an efficient and practical solution for imaging applications in fields such as cinematography, smartphone imaging, and microscopy.

III. *Development of Post Ensemble Generation with Airy beams for Spatial and Spectral Switching* (*PEGASASS*)

- PEGASASS introduces a new CAI approach for achieving post-recording AR tuning without affecting LR, which is the central goal of this thesis, using Airy beam ensembles, in contrast to the hybridization-based approach used in INCHIS.
- In PEGASASS, the cubic phase mask acts as the CPM to convert the light from an object point into an Airy beam. Here, the LR and AR correspond to the lateral and axial correlation lengths, respectively. Due to the long propagation-invariant nature of Airy beams, these systems inherently exhibit an unusual high LR-low AR pair. By creating an ensemble of unique Airy intensity distributions post-recording, the propagation

invariance and chaos from relative random shifts between Airy beams can be made to act against one another to achieve tunability of axial correlation length. The lateral correlation length remains dependent on the NA and so remains unaffected when the axial correlation length is varied.

- PEGASASS utilizes four unique CPMs to produce Airy beams with distinct 3D propagation characteristics. After recording, a synthetic ensemble of Airy beams with an Airy intensity distribution was constructed, and the AR was engineered without affecting the LR by controlling the number and relative strengths of the Airy beams in the ensemble.
- As in INCHIS, PSFs are recorded under identical experimental conditions and processed with OIDs using LRRA to retrieve the 3D object information.
- In addition to AR modulation, we have also demonstrated post-recording SR modulation in PEGASASS. To the best of our knowledge, this is the first demonstration of SR control in a CAI system with a monochrome sensor.
- Experimental validations of PEGASASS confirm that as a flexible platform for multidimensional imaging and pave the way for adaptive tuning of AR and SR in next-generation CAI systems.

IV. *Development of Post-Engineering of Axial Resolution in Fresnel Incoherent Correlation Holography* (*PEAR-FINCH*)

- A method termed PEAR-FINCH was developed to introduce post-recording FD engineering in the FINCH framework for the first time, enabling flexible FD control beyond conventional limits of FINCH.
- A library of FINCH holograms was recorded for different self-interference conditions.
- Selected holograms from this library were computationally combined to generate synthetic holograms with engineered axial characteristics, allowing FD tuning to be possible after data acquisition.
- A two-step numerical reconstruction approach comprising Fresnel back-propagation followed by deconvolution using a PSH was employed to recover 3D object information with a high SNR.
- Experimental validation confirmed that PEAR-FINCH extends the FD manifold up to five times beyond conventional FINCH limits, demonstrating its potential for applications in microscopy, biomedical imaging, and holography

2.3 Overall impact and novelty

The four research works developed in this doctoral research, TAP-GSA, INCHIS, PEGASASS, and PEAR-FINCH, collectively establish a unified CI framework for advancing the frontiers of IDH and CAI. Each research work addresses a specific, long-standing limitation in imaging science:

- TAP-GSA provides a universal computational solution to the challenge in designing multiplexed CPM in holography and diffractive optics, enabling the realization of complex-valued CPMs, using engineered phase-only CPMs.
- INCHIS is the first method to offer independent post-recording control of AR without affecting LR, using a simplified, low-cost, and easily implementable optical configuration.
- PEGASASS extends post-recording tunability to multidimensional imaging, achieving control of AR and SR without affecting LR, employing only a monochrome sensor.
- PEAR-FINCH is the first post-engineering approach to FD control within the FINCH framework, surpassing conventional limits of FINCH.

Together, these research works advance the state-of-the-art and the capabilities of computationally adaptive imaging, offering robust, low-complexity, and experimentally feasible solutions. The outcomes of this research provide powerful new tools for real-world applications in biomedical imaging, microscopy, IDH, cinematography, and smartphone imaging.

CHAPTER 3: METHODOLOGY

As discussed in Chapters 1 and 2, the primary objective of this doctoral research is to address the lack of flexibility in existing IDH and CAI systems, particularly their inability to achieve independent post-recording tunability of imaging resolutions. Realizing such flexibility requires CPM engineering, since many incoherent imaging frameworks rely on multiplexing multiple beam-shaping phase functions within a single optical element. However, when two or more pure phase functions are combined, the resulting function becomes complex-valued, containing both amplitude and phase components. Such complex-valued functions cannot be directly realized with phase-only SLMs or conventional lithographic fabrication methods. Existing multiplexing approaches, including modulo-2π phase addition and RM, have limitations such as scattering noise, reduced light throughput, and restricted independence between encoded functionalities. Therefore, a computationally efficient and experimentally feasible strategy is required to synthesize multifunctional CPMs that emulate complex-valued behaviour while remaining phase-only. To address this enabling challenge, the TAP-GSA was developed and serves as the foundational method for CPM design in the subsequent imaging frameworks developed in this thesis.

3.1 TAP-GSA

The TAP-GSA is discussed briefly in the following Sections 3.1.1 and 3.1.2. The implementation of TAP-GSA in FINCH is discussed briefly in Section 3.1.3.

3.1.1 Working principle of TAP-GSA

The schematic representation of the TAP-GSA is shown in **Figure 8**. The algorithm operates in two steps: In the first step, two or more pure phase functions are summed, producing a complex-valued function that represents the ideal function in the mask plane. This complex-valued function is then propagated from the mask plane to the sensor plane using a Fresnel transform, corresponding to the propagation distance used in the optical experiment. The resulting complex amplitude represents the ideal function in the sensor plane. In the second step, TAP-GSA imposes a uniform amplitude distribution constraint with the phase distribution extracted from the ideal complex-valued function at the mask plane. This complex-valued function is propagated to the sensor plane using the Fresnel transform, and the resulting amplitude is replaced by the ideal amplitude obtained earlier at the sensor plane in the first step. The resulting phase at the sensor plane replaces the ideal phase obtained at the sensor plane in the first step for certain pixels. The *degrees of freedom (DoF)* determine the number of pixels replaced in the phase component relative to the total number of pixels, and the percentage of pixel replacement can be chosen according to our requirements on SNR. After

applying these constraints, the resulting complex-valued function at the sensor plane is back-propagated to the mask plane by applying the inverse Fresnel transform. The process is iterated until a non-changing phase-only function is obtained.

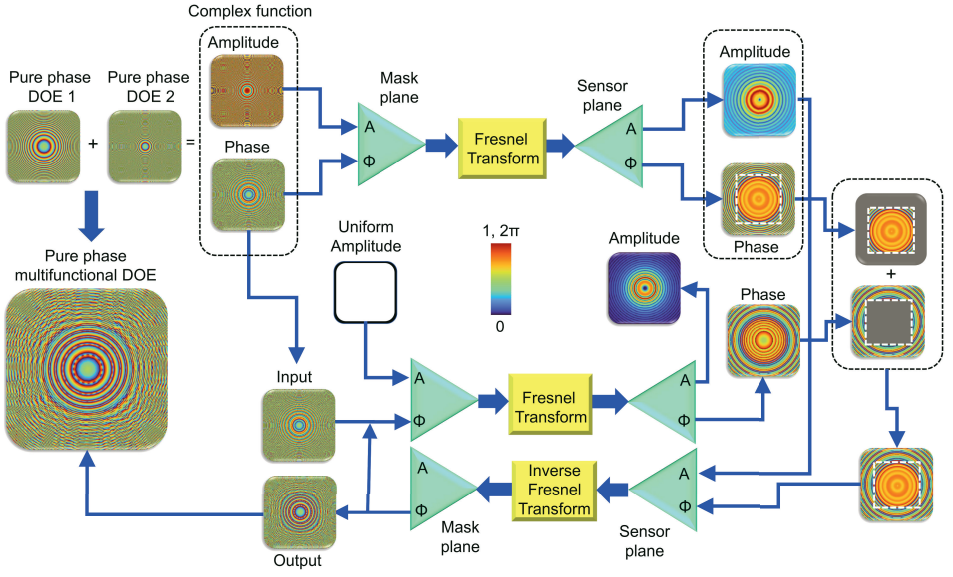

Figure 8. Schematic representation of TAP-GSA. (Adapted from **Publication I**)

3.1.2 Differences between GSA and TAP-GSA

Although TAP-GSA is designed based on conventional GSA, its formulation and objective differ in the context of multifunctional DOE synthesis for incoherent imaging system applications.

- **Objective:** GSA is widely used to calculate the phase distribution at the mask plane that yields a desired intensity distribution at the sensor plane by imposing constraints at both planes. In contrast, TAP-GSA, as the name suggests, is specifically designed to transport amplitude information into phase, converting a complex-valued function into a pure phase-only function while preserving its optical functionality.
- **Constraints:** The GSA is primarily used to achieve a specific intensity distribution while leaving the phase unconstrained in the sensor plane. TAP-GSA, on the other hand, introduces a limited phase constraint at the sensor plane in addition to the amplitude constraint.
- **Application:** While GSA has been widely applied in beam shaping and holographic projection, TAP-GSA is specifically formulated for synthesizing multifunctional phase-only DOEs in IDH and CAI systems that emulate the behaviour of a complex-valued function.

The mathematical formulation of inequality addressed by the TAP-GSA is given below:

Consider two phase-only functions defined at the mask plane,

$$f_1(x,y) = exp\{j\phi_1(x,y)\}, \tag{3}$$

$$f_2(x,y) = exp\{j\phi_2(x,y)\}, \tag{4}$$

where x and y denote the transverse spatial coordinates in the mask plane.

When the two phase-only functions are combined to achieve multifunctionality,

$$F(x,y) = f_1(x,y) + f_2(x,y). \tag{5}$$

Substituting Equations (3) and (4) into Equation (5),

$$F(x,y) = exp\{j\phi_1(x,y)\} + exp\{j\phi_2(x,y)\}. \tag{6}$$

Using Euler's formula, $exp(j\phi) = \cos\phi + j\sin\phi$, Equation (6) can be written as,

$$F(x,y) = \cos\big(\phi_1(x,y)\big) + \cos\big(\phi_2(x,y)\big) + j[\sin(\phi_1(x,y)) + \sin(\phi_2(x,y))]. \tag{7}$$

Therefore, the resultant complex function can be expressed in polar form as,

$$F(x,y) = A(x,y)\, exp\{j\psi(x,y)\}, \tag{8}$$

where $A(x,y)$ and $\psi(x,y)$ denote the amplitude and phase of the resultant function, respectively. Since $A(x,y)$ is generally non-uniform, $F(x,y)$ becomes a complex-valued function containing both amplitude and phase variations. Such a function cannot be implemented directly with either phase-only or amplitude-only SLMs and is also challenging to fabricate using conventional lithographic techniques. The objective of TAP-GSA is to determine a phase-only function,

$$G(x,y) = exp\{j\phi(x,y)\}, \tag{9}$$

such that

$$A(x,y)\, exp\{j\psi(x,y)\} \approx exp\{j\phi(x,y)\}. \tag{10}$$

This is achieved through an iterative procedure in which amplitude information is progressively transferred to the phase distribution. In summary, TAP-GSA adapts the conventional GSA framework, enabling the practical realization of multifunctional phase-only DOEs compatible with modern digital holographic and CI systems.

3.1.3 Implementation of TAP-GSA in FINCH

Two different optical configurations of FINCH were considered in this study, namely FINCH with maximum optical path difference [38] and FINCH with reduced optical path difference [96], as shown in **Figures 9(a) and 9(b)**, respectively. In FINCH, light from an object point is divided into two beams, each modulated by a diffractive lens with a different focal length. The two beams interfere, forming a self-interference hologram. In the in-line configuration, at least three holograms with phase shift values $\theta = 0$, $2\pi/3$, and $4\pi/3$ are recorded and digitally superposed to generate a complex hologram. This hologram is then numerically propagated by different reconstruction distances to obtain the object images at different planes [38].

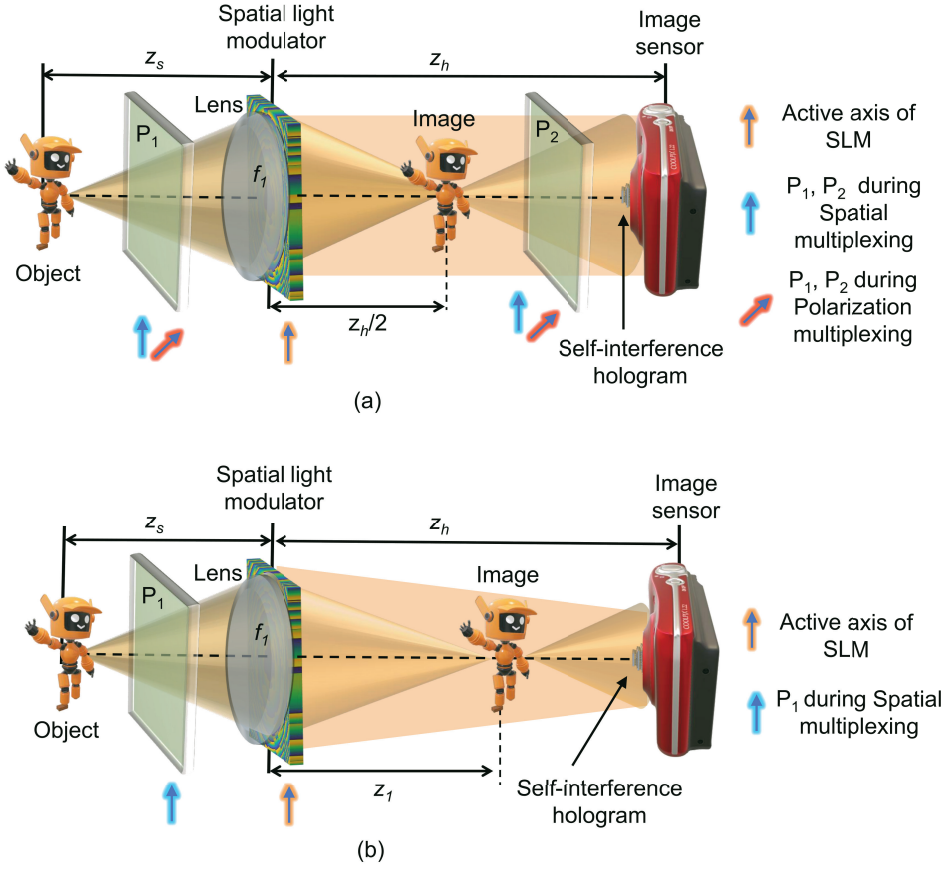

Figure 9. Optical configurations of FINCH. **(a)** Maximum optical path difference. **(b)** Reduced optical path difference. P_1 and P_2 are the two polarizers. z_s and z_h are object and recording distances. f_1 is the focal length of the lens. (Adapted from **Publication I**)

3.1.3.1 Configuration 1 – FINCH with maximum optical path difference

For the first configuration, **Figure 9(a)**, a point object with an amplitude of $\sqrt{I_o}$ is considered. The complex amplitude of the object wave at a distance z_s from the plane of a refractive lens with focal length f_1 is given as $C_1\sqrt{I_o}Q(1/z_s)$, where $Q(a) = exp(i\pi ar^2/\lambda)$, $r = \sqrt{x^2 + y^2}$ and C_1 is a complex constant. For the PM method, the modulation function is expressed as $exp(i\pi r^2/\lambda f_2)$. In this method, only the polarization component of the incident light aligned with the SLM's active axis is modulated, while the orthogonal polarization component remains unmodulated. For the RM method, the phase function displayed on the SLM is given by,

$$\Phi(x,y) = B(x,y) + (\pi r^2/\lambda f_2)\big(1 - B(x,y)\big), \tag{11}$$

where $B(x,y) \in \{0,1\}$ is a binary random function, and $B(x,y)$ does not focus the incoming light, while the second term focuses light at $z_h/2$ when f_2 satisfies the relation $(f_1+f_2)/(f_1f_2) = 1/z_s+2/z_h$. For the case $z_s = f_1$, this simplifies to $f_2 = z_h/2$. The complex amplitude after the SLM becomes $C_2\sqrt{I_o}Q(1/z_s)Q(-1/f_1)exp[-i\Phi(x,y)]$, where C_2 is a complex constant. The intensity (I_{PSH}), which is the PSH, is given as,

$$I_{PSH} = \left|C_2\sqrt{I_o}Q(1/z_s)\,Q(-1/f_1)exp[-i\Phi(x,y)]\otimes Q(1/z_h)\right|^2. \tag{12}$$

As FINCH is a linear, shift-invariant system, the hologram for an object O can be given as $I_{OH} = I_{PSH}\otimes O$. Since FINCH is an in-line holography configuration, to reconstruct the object's image, it is necessary to remove the twin-image and bias terms present in the hologram. This is achieved by a phase-shifting process: three I_{OHs} with phase shifts, θ = 0, 2π/3, and 4π/3, between the interfering beams are recorded and combined to remove the twin-image and bias terms from the holograms. This is achieved by real-time changing of the phase of the multiplexed lens displayed on the SLM. The complex hologram (H_{OH}) can be written as,

$$\begin{aligned} H_{OH} = I_{OH}(\theta = 0)(exp[-i4\pi/3] - exp[-i2\pi/3]) + I_{OH}\left(\theta = \tfrac{2\pi}{3}\right) \\ (1 - exp[-i4\pi/3]) + I_{OH}\left(\theta = \tfrac{4\pi}{3}\right)(exp[-i2\pi/3] - 1). \end{aligned} \tag{13}$$

The image of the object is reconstructed from the complex hologram as

$$I_R = H_{OH}\otimes Q(1/z_r), \tag{14}$$

where z_r is the reconstruction distance. By tuning the reconstruction distance, it is possible to reconstruct different planes of the object. In Configuration 1, three methods were evaluated: (i) PM, (ii) RM, and (iii) TAP-GSA. For the evaluation of the PM method, both polarizers P_1 and P_2, as shown in **Figure 9(a)**, are oriented at 45° relative to the SLM's active axis. For the evaluation of the RM and TAP-GSA methods, the two polarizers are oriented along the SLM's active axis.

3.1.3.2 Configuration 2 – FINCH with reduced optical path difference

For the second configuration, **Figure 9(b)**, the modulation function can be expressed as $exp(i\pi r^2/\lambda f_2)$ for one orientation and $exp(i\pi r^2/\lambda f_3)$ for the other orthogonal orientation. For the RM method and assuming $z_s = f_1$, the phase function displayed on the SLM is given as

$$\Phi(x,y) = (\pi r^2/\lambda f_2)B(x,y) + (\pi r^2/\lambda f_3)\big(1 - B(x,y)\big), \tag{15}$$

where $f_2^{-1} + f_3^{-1} = 2z_h^{-1}$ to satisfy the beam matching condition [96]. The first image is formed at a distance z_1 ($= f_2$ in case $z_s = f_1$) from the SLM. In Configuration 2, the RM and TAP-GSA methods were evaluated. Hence, Configurations 1 and 2 are used to compare the performance of the TAP-GSA method with that of other methods. The results are presented in Chapter 4, Section 4.1.2.

3.2 INCHIS

The optical configurations of INCHIS-H1 and INCHIS-H2 are shown in **Figures 10 and 11**, respectively. The INCHIS framework was developed to overcome the limitation of coupled image resolutions in incoherent CI systems by allowing independent control of the AR without affecting the LR. In INCHIS-H1, the pure optical fields for hybridization are first selected, and the corresponding CPMs are calculated following standard diffractive optical design procedures [91]. The CPMs that generate the individual pure optical fields are then multiplexed into a single hybrid CPM using the TAP-GSA. Although the algorithm can multiplex several phase masks, for INCHIS-H1, only two-phase functions, namely a diffractive lens and a diffractive axicon, are considered. The relative strengths of the two optical fields are controlled by two variables, T_1 and T_2, applied as weights to the pure phase functions of the lens and axicon.

The ideal hybrid complex-valued function corresponding to the lens and axicon can be expressed as $F_H(x,y) = T_1\, exp\{j\phi_L(x,y)\} + T_2\, exp\{j\phi_A(x,y)\}$, where $\phi_L(x,y)$ and $\phi_A(x,y)$ denote the phase functions of the lens and axicon, respectively. Since $F_H(x,y)$ will result in a complex-valued function, TAP-GSA is employed to synthesize a physically realizable phase-only hybrid mask, $G_H(x,y) = exp\{j\phi_H(x,y)\}$, exhibiting the behaviour equivalent to the complex-valued function. The resulting hybrid phase-only mask obtained from TAP-GSA is displayed on an SLM, and the intensity (I_{PSF}) library is recorded at different axial locations using a point object. Then, the point object is replaced by an object, and the OID is recorded under identical experimental conditions. The 3D image of the object is reconstructed by processing the PSF library and OID using LRRA [56]. The AR of the imaging system varies according to the selected values of T_1 and T_2. When the phase mask is pure, either that of a diffractive axicon or a diffractive lens, the system behaves similarly to I-COACH or CAI, since only a

single beam is generated. When a hybrid mask is used, two beams are produced that self-interfere, and the system behaves like FINCH or COACH, thereby enabling tunable AR in real-time. In INCHIS-H2, the light from an object point is divided into two identical beams using a 50–50 beam splitter. These two beams are then modulated by two active or passive optical elements, namely a lens and an axicon, under identical configurations, and the respective PSF intensities ($I_{PSF\text{-}L}$) and ($I_{PSF\text{-}A}$) are recorded. The OID ($I_{OID\text{-}L}$) and ($I_{OID\text{-}A}$) are recorded similarly under identical conditions. The hybrid PSF intensity ($I_{PSF\text{-}H}$) and hybrid OID ($I_{OID\text{-}H}$) are then computed by summing the individual contributions from the lens and axicon after assigning their respective weights, T_1 and T_2, given as $I_{PSF-H} = I_{PSF-L} \times T_1 + I_{PSF-A} \times T_2$ and $I_{OID-H} = I_{OID-L} \times T_1 + I_{OID-A} \times T_2$. The values of T_1 and T_2 are controlled as $0 \leq T_1 \leq 1$ and $0 \leq T_2 \leq 1$. The object's image is reconstructed by processing the $I_{PSF\text{-}H}$ and $I_{OID\text{-}H}$ using the LRRA [56]. By recording a scene collinearly through both the axicon and the lens, using two cameras under identical conditions, the AR can be engineered after recording. This unique capability enables post-recording tunability of AR, a feature not previously demonstrated in incoherent holographic and CI systems.

3.2.1 INCHIS-H1

A point object located at $(\bar{r}_s, z_s)$ and emitting light with an amplitude of $\sqrt{I_s}$ is considered. A hybrid CPM designed by combining the CPMs of a diffractive axicon and a diffractive lens using TAP-GSA is located at a distance of z_s from the point object. The complex amplitude of the hybrid CPM can be approximated as,

$$\psi_{CPM} \approx exp[-i\pi T_1(\lambda f)^{-1}(x^2 + y^2)] + exp\left[-i2\pi T_2 \Lambda^{-1}\sqrt{x^2 + y^2}\right], \qquad (16)$$

where f is the focal length of the diffractive lens, Λ is the period of the diffractive axicon, λ is the illumination wavelength, T_1 and T_2 are controlled as $0 \leq T_1 \leq 1$ and $0 \leq T_2 \leq 1$ and ψ_{CPM} is a phase-only function in the experiment. For simplicity, only a single wavelength λ is considered. The variables T_1 and T_2 control the contributions from a diffractive lens and a diffractive axicon, respectively. When $T_1 = 0$ and $T_2 = 1$, the hybrid CPM reduces to a diffractive axicon, and when $T_1 = 1$ and $T_2 = 0$, the hybrid CPM reduces to a diffractive lens, and for other values of T_1 and T_2, a hybrid CPM is obtained.

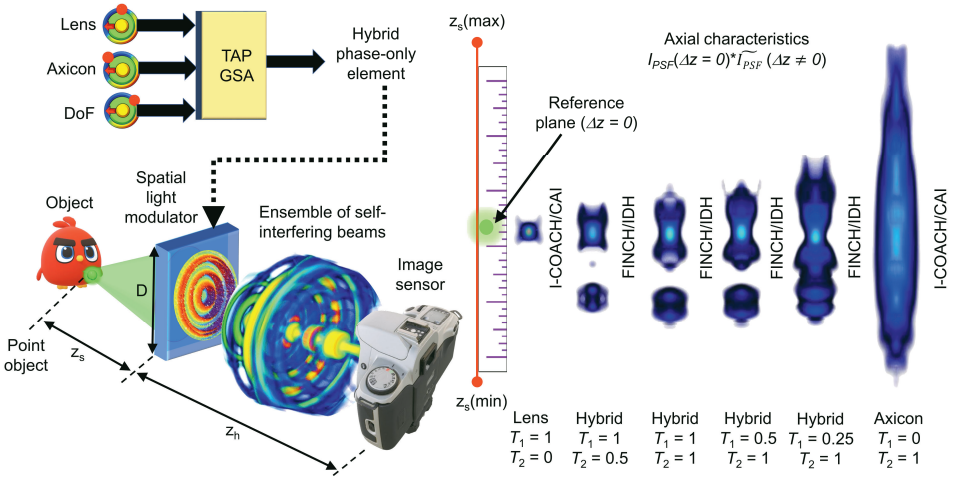

Figure 10. Optical configuration of INCHIS-H1. z_s and z_h are object and recording distances, D is the diameter of the aperture, TAP-GSA – transport of amplitude into phase based on Gerchberg-Saxton algorithm, I_{PSF} – point spread function, $\widetilde{I_{PSF}}$ – phase-only filtered version of I_{PSF}, $\Delta z = 0$ – plane of interest, DoF – degrees of freedom and T_1 and T_2 – strengths of the phase modulators, namely lens and an axicon. The axial distributions were generated using a phase-only filter. (Adapted from **Publication II**)

The complex amplitude after the hybrid phase mask is given as $\sqrt{I_s}C_1 L\left(\frac{\bar{r}_s}{z_s}\right) Q\left(\frac{1}{z_s}\right)\psi_{CPM}$, where L and Q are the linear and quadratic phase functions given as $L\left(\frac{\bar{s}}{z}\right) = exp\left[i2\pi(\lambda z)^{-1}(s_x x + s_y y)\right]$ and $Q(b) = exp[i\pi b\lambda^{-1}(x^2 + y^2)]$, respectively, and C_1 is a complex constant. A self-interference is obtained between the Bessel beam and spherical beam as both are derived from the same object point. The intensity (I_{PSF}) recorded by the image sensor located at a distance of z_h is the PSF, which is given as,

$$I_{PSF}(\bar{r}_0; \bar{r}_s, z_s) = \left|\sqrt{I_s}C_1 L\left(\frac{\bar{r}_s}{z_s}\right) Q\left(\frac{1}{z_s}\right)\psi_{CPM} \otimes Q\left(\frac{1}{z_h}\right)\right|^2 \tag{17}$$

where, $\bar{r}_0 = (u, v)$ is the location vector in the sensor plane. Now substituting for ψ_{CPM} in Equation (17), we obtain,

$$I_{PSF}(\bar{r}_0; \bar{r}_s, z_s) = \left|\sqrt{I_s}C_1 L\left(\frac{\bar{r}_s}{z_s}\right) Q\left(\frac{1}{z_s}\right)\left\{exp[-i\pi T_1(\lambda f)^{-1}(x^2 + y^2)] + exp\left[-i2\pi T_2 \Lambda^{-1}\sqrt{x^2 + y^2}\right]\right\} \otimes Q\left(\frac{1}{z_h}\right)\right|^2. \tag{18}$$

After grouping the individual contributions, we get,

$$I_{PSF}(\bar{r}_0;\bar{r}_s,z_s)=\left|\sqrt{I_s}C_1L\left(\frac{\bar{r}_s}{z_s}\right)Q\left(\frac{1}{z_s}\right)exp[-i\pi T_1(\lambda f)^{-1}(x^2+y^2)]\otimes Q\left(\frac{1}{z_h}\right)\right.$$
$$\left.+\ \sqrt{I_s}C_1L\left(\frac{\bar{r}_s}{z_s}\right)Q\left(\frac{1}{z_s}\right)exp\left[-i2\pi T_2\Lambda^{-1}\sqrt{x^2+y^2}\right]\otimes Q\left(\frac{1}{z_h}\right)\right|^2, \tag{19}$$

$$I_{PSF}(\bar{r}_0;\bar{r}_s,z_s)=|A_{DL}+A_{DA}|^2, \tag{20}$$

where A_{DL} and A_{DA} are the complex amplitudes with diffraction efficiencies corresponding to maximum phases ($2\pi T_1$) and ($2\pi T_2$) generated for the diffractive lens and diffractive axicon, respectively and are a spherical beam given as $Q\left(\frac{1}{z_e}\right)$, where $\frac{1}{z_e}=\frac{1}{z_s}+\frac{1}{z_h}-\frac{1}{f}$ and a Bessel beam of the first kind J_0. The transverse magnification of the system is given by $M_T=z_h/z_s$. The I_{PSF} can be expressed as,

$$I_{PSF}(\bar{r}_0;\bar{r}_s,z_s)=I_{PSF}\left(\bar{r}_0-\frac{z_h}{z_s}\bar{r}_s\,;0\,,z_s\right). \tag{21}$$

A 2D object consisting of M points can be represented as a collection of M Kronecker Delta functions as

$$O(\bar{r}_s)=\sum_j^M a_j\delta\left(\bar{r}-\bar{r}_{s,j}\right), \tag{22}$$

where $a_j's$ are constants. Since only spatially incoherent illumination is considered, the light diffracted from one point does not interfere with light diffracted from another, but their intensities add up in the sensor plane. Therefore, the OID obtained for object (O) can be expressed as,

$$I_{OID}(\bar{r}_0\,;z_s)=\sum_j^M a_j I_{PSF}\left(\bar{r}_0-\frac{z_h}{z_s}\bar{r}_{s,j}\,;0\,,z_s\right). \tag{23}$$

The goal is to reconstruct O from I_{PSF} and I_{OID} given by Equations (21) and (23), respectively. If the autocorrelation of I_{PSF} gives a Delta-like function, then the O can be reconstructed by a cross-correlation between I_{PSF} and I_{OID}. In a recent study, the use of NLR generated a sharp autocorrelation function and therefore effectively reconstructed the intensity distributions of multipoint objects [63]. The reconstructed image by the matched filter is given as

$$\begin{aligned}P(\bar{r}_R)\ &=\iint I_{OID}(\bar{r}_0\,;z_s)I^*_{PSF}(\bar{r}_0-\bar{r}_R\,;z_s)d\bar{r}_0\\ &=\iint\sum_j a_j I_{PSF}\left(\bar{r}_0-\frac{z_h}{z_s}\bar{r}_{s,j}\,;z_s\right)I^*_{PSF}(\bar{r}_0-\bar{r}_R\,;z_s)d\bar{r}_0\\ &=\sum_j a_j\mathfrak{Z}\left(\bar{r}_R-\frac{z_h}{z_s}\bar{r}_{s,j}\right)\approx O\left(\frac{\bar{r}_s}{M_T}\right),\end{aligned} \tag{24}$$

where '$*$' means complex conjugate. For a speckle pattern, $\mathfrak{Z}$ is a Delta-like function. But for most deterministic fields, such as Gaussian, Bessel, Laguerre-

Gaussian beams, etc., ʒ is not a Delta-like function. The reconstruction by NLR generates a Delta-like function for both random and deterministic optical fields. The reconstruction by NLR is given in Equation (2). However, LRRA was developed by combining LRA and NLR, yielding a higher SNR than NLR alone, as seen in recent studies [56, 57, 64]. Hence, the LRRA was used for image reconstruction in INCHIS-H1.

Within the focal depth of the Bessel beam, the A_{DA} remains a constant, while A_{DL} varies. By controlling T_1 and T_2, I_{PSF} can be shifted towards the behaviours of A_{DA} and A_{DL}. When the system is shifted towards A_{DL}, I_{PSF} changes with z_s, and so it is necessary to record I_{PSF} for all values of z_s. On the other hand, when the system is shifted towards A_{DA}, I_{PSF} does not change with z_s, so I_{PSF} recorded for one z_s can be used to reconstruct all, if not most, of the object planes. Unlike the case with A_{DL}, with A_{DA}, the object information is not blurred or unrecognizable but has a low resolution due to suppression of higher spatial frequencies [63, 97].

3.2.2 INCHIS-H2

A point object located at $(\bar{r}_s, z_s)$ is considered. It emits light with an amplitude of $\sqrt{I_s}$. The light from the point object is split into two using a 50–50 beam splitter. One of the two parts was modulated by a lens and another by an axicon, both located at a distance of z_s from the point object. Two identical image sensors are mounted at distances z_h from the lens and the axicon, respectively, such that their optical axes overlap. The complex amplitude after the lens and the axicon are given as $\sqrt{I_s/2}C_1 L\left(\frac{\bar{r}_s}{z_s}\right) Q\left(\frac{1}{z_s}\right) exp[-i\pi(\lambda f)^{-1}(x^2+y^2)]$ and $\sqrt{I_s/2}C_1 L\left(\frac{\bar{r}_s}{z_s}\right) Q\left(\frac{1}{z_s}\right) exp\left[-i2\pi\Lambda^{-1}\sqrt{x^2+y^2}\right]$ respectively. The intensity distributions recorded for a point object for a lens (I_{PSF-L}) and an axicon (I_{PSF-A}) are given as,

$$I_{PSF-L}(\bar{r}_0;\bar{r}_s,z_s) = \left|\sqrt{I_s/2}C_1 L\left(\frac{\bar{r}_s}{z_s}\right) Q\left(\frac{1}{z_s}\right) exp[-i\pi(\lambda f)^{-1}(x^2+y^2)] \otimes Q\left(\frac{1}{z_h}\right)\right|^2, \quad (25)$$

$$I_{PSF-A}(\bar{r}_0;\bar{r}_s,z_s) = \left|\sqrt{I_s/2}C_1 L\left(\frac{\bar{r}_s}{z_s}\right) Q\left(\frac{1}{z_s}\right) exp\left[-i2\pi\Lambda^{-1}\sqrt{x^2+y^2}\right] \otimes Q\left(\frac{1}{z_h}\right)\right|^2. \quad (26)$$

The hybrid PSF of the system is given as,

$$I_{PSF-H}(\bar{r}_0;\bar{r}_s,z_s) = T_1 \times I_{PSF-L}(\bar{r}_0;\bar{r}_s,z_s) + T_2 \times I_{PSF-A}(\bar{r}_0;\bar{r}_s,z_s), \quad (27)$$

where $0 \le T_1 \le 1$ and $0 \le T_2 \le 1$ control the contributions of the lens and the axicon, respectively. The OID can be given by Equation (23), which is simply $I_{OID-L} = I_{PSF-L} \otimes O$ and $I_{OID-A} = I_{PSF-A} \otimes O$ for the lens and the axicon, respectively. The advantage of the INCHIS-H2 is that the AR can be tuned after completing the recording process by tuning T_1 and T_2. It is possible to reconstruct O by processing $I_{OID-L} \times T_1 + I_{OID-A} \times T_2$ and $I_{PSF-L} \times T_1 + I_{PSF-A} \times T_2$, as $(I_{PSF-L} \times T_1 + I_{PSF-A} \times T_2) \otimes O = I_{OID-L} \times T_1 + I_{OID-A} \times T_2$. The LRRA is used for image reconstruction in INCHIS-H2.

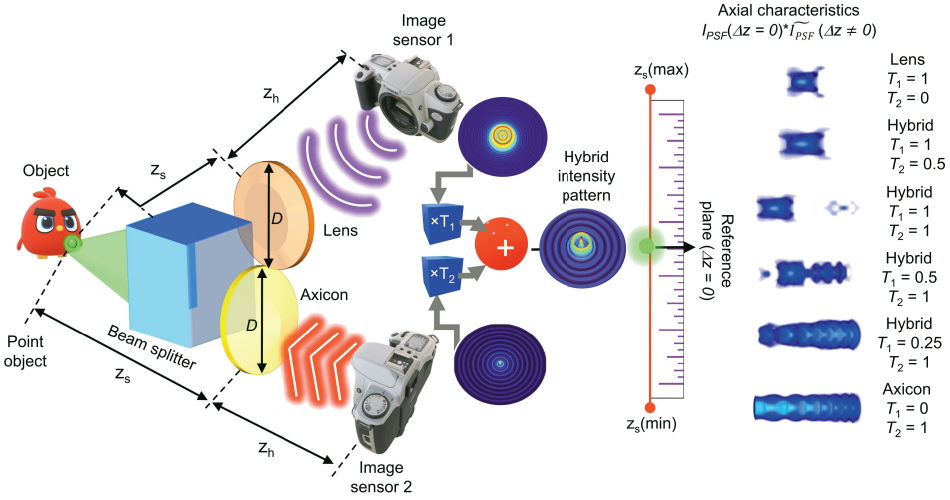

Figure 11. Optical configuration of INCHIS-H2. z_s and z_h are object and recording distances, D is the diameter of the aperture, I_{PSF} – point spread function, $\widetilde{I_{PSF}}$ – phase-only filtered version of I_{PSF}, $\Delta z = 0$ – plane of interest, and T_1 and T_2 – strengths of the intensity distributions, namely lens and an axicon. The axial distributions were generated using a phase-only filter. (Adapted from **Publication II**)

3.3 PEGASASS

The optical configuration of PEGASASS is shown in **Figure 12(a)**. Light from an object point with an amplitude of $\sqrt{I_s}$ reaches a coded mask located at a distance of z_s with a complex amplitude of $\sqrt{I_s} C_1 L\left(\frac{\vec{r}_s}{z_s}\right) Q\left(\frac{1}{z_s}\right)$, where C_1 is a complex constant; $Q(a) = exp[i\pi a\lambda^{-1}(x^2 + y^2)]$ and $L\left(\frac{\vec{s}}{z}\right) = exp\left[i2\pi(\lambda z)^{-1}(s_x x + s_y y)\right]$ are the quadratic and linear phase functions, respectively. The CPM in PEGASASS is a cubic phase mask, which is given as,

$$exp[j\Phi_{CPM}(k)] = exp\left[-j\frac{2\pi}{\lambda}\{\xi_k(x_k + \Delta x_k)^3 + \eta_k(y_k + \Delta y_k)^3\}\right], \quad (28)$$

where the variables, $x_k = x_0 cos\theta_k + y_0 sin\theta_k$ and $y_k = y_0 cos\theta_k - x_0 sin\theta_k$ can be used to rotate the coordinate system, and k is an integer ranging from 1 to M corresponding to times $t_{k=1}$ to $t_{k=M}$, where M is the number of camera recordings. Here, t_k denotes the recording instances in the PEGASASS method and is distinct from the variables T_1 and T_2 used in the INCHIS method. The shift parameters Δx_k, and Δy_k can be used to shift the origin of the CPM, and while ξ_k, and η_k act as scaling factors that control the magnification along the x and y directions, respectively.

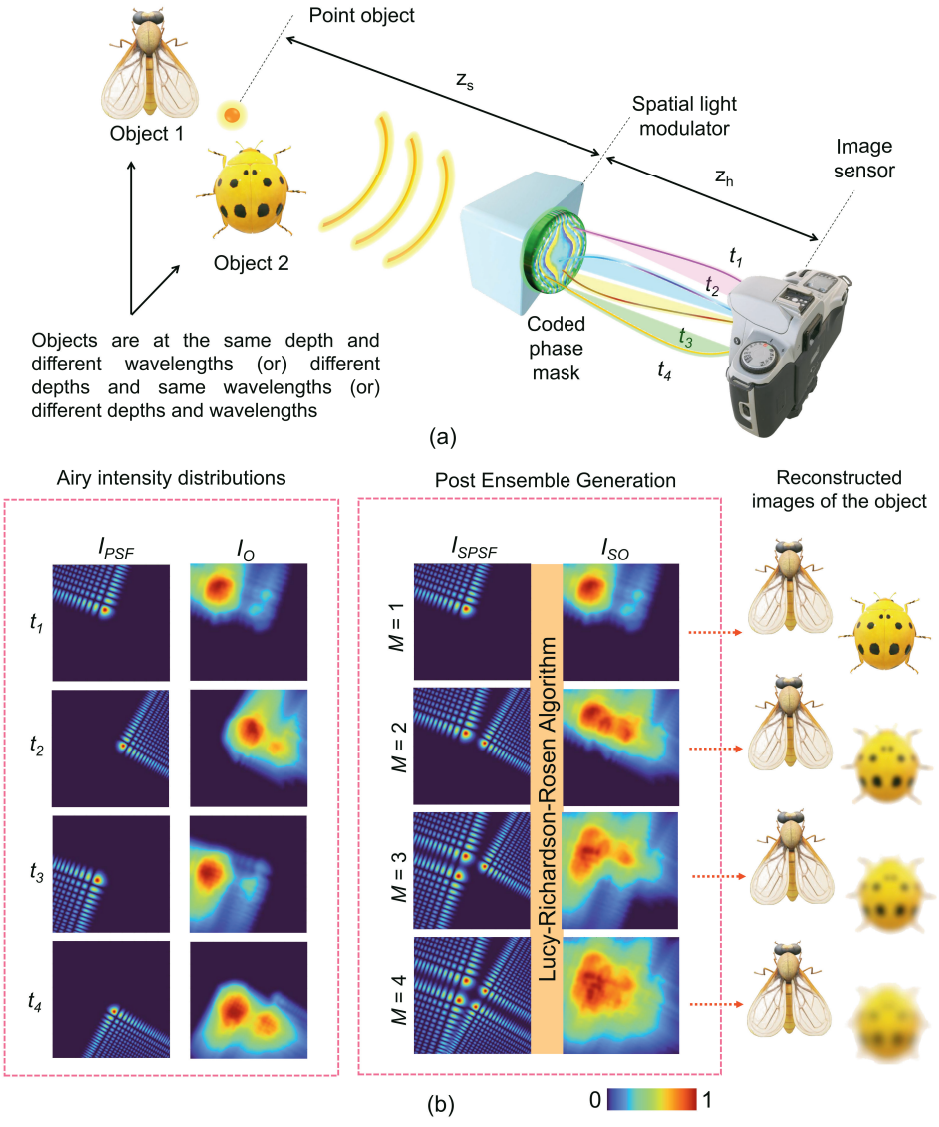

Figure 12. (a) Optical configuration and **(b)** post-engineering process of PEGASASS. z_s and z_h are object and recording distances. t_1, t_2, t_3, and t_4 indicate the four acquisition times at which Airy intensity distributions corresponding to the unique CPMs are recorded. M denotes the number of Airy beams in the ensemble. (Adapted from **Publication III**)

The complex amplitude after the CPM is given as $\sqrt{I_s}C_1 L\left(\frac{\bar{r}_s}{z_s}\right) Q\left(\frac{1}{z_s}\right) exp[j\Phi_{CPM}(k)]$. The intensity ($I_{PSF}$) recorded at a distance of z_h from the CPM is the PSF, which is given as,

$$I_{PSF}(\bar{r}_0; \bar{r}_s, z_s, k) = \left|\sqrt{I_s}C_1 L\left(\frac{\bar{r}_s}{z_s}\right) Q\left(\frac{1}{z_s}\right) exp[j\Phi_{CPM}(k)] \otimes Q\left(\frac{1}{z_h}\right)\right|^2. \quad (29)$$

The above expression can be simplified into,

$$I_{PSF}(k) = \left|Ai_k\left(\frac{x_k}{a_k}, \frac{y_k}{a_k}\right)\right|^2, \quad (30)$$

where Ai is the truncated Airy function, and a_k is the scaling factor of the Airy function. Like most CAI systems, PEGASASS is also a linear shift-invariant system, and therefore, the I_{PSF} can be expressed as

$$I_{PSF}(\bar{r}_0; \bar{r}_s, z_s, k) = I_{PSF}\left(\bar{r}_0 - \frac{z_h}{z_s}\bar{r}_s\,; 0\,, z_s, k\right), \quad (31)$$

where z_h/z_s is the magnification. The OID for a 2D object consisting of N points given as $O(\bar{r}_s) = \sum_p^N b_p \delta(\bar{r} - \bar{r}_{s,p})$ is given as,

$$I_{OID}(\bar{r}_0\,; z_s\,, k) = \sum_p^N b_p I_{PSF}\left(\bar{r}_0 - \frac{z_h}{z_s}\bar{r}_{s,p}\,; 0\,, z_s, k\right). \quad (32)$$

In PEGASASS, *synthetic point spread functions* (*SPSFs*) and *synthetic object intensity distributions* (*SOIDs*) are created by constructing identical ensembles post-recording, given as,

$$I_{SPSF}(\lambda, z) = \sum_{k=1}^M \gamma_k I_{PSF}(\lambda, z, k), \quad (33)$$

$$I_{SOID} = \sum_{k=1}^M \gamma_k I_{OID}(k), \quad (34)$$

where γ_k is the weight of the k^{th} intensity distribution. The image of the object corresponding to a particular pair (λ, z) can be reconstructed by processing I_{SOID} with $I_{SPSF}(\lambda, z)$ using one of the deconvolution methods [56, 63]. The information corresponding to $\lambda' \neq \lambda$ and $z' \neq z$ appears blurred and forms the background. In regular CAI methods, the degree of blur is directly proportional to $\Delta\lambda$ and Δz. This cannot be changed after recording. But in PEGASASS, this degree of blur is tunable post-recording by changing M as shown in **Figure 12(b)**. When M increases, the blur increases, and vice versa. The LRRA has been used for image reconstruction in PEGASASS.

The imaging process in PEGASASS is based on the properties of spatially incoherent illumination and applies to most CAI imaging systems operating under similar conditions. When M = 1, only a single Airy beam is generated, corresponding to a low AR and SR. In this case, imaging a thick object results in the reconstruction of multiple axial planes within the long focal depth due to the Airy

beam's non-diffractive nature. As M increases, each Airy beam in the ensemble maintains its individual non-diffractive nature; however, their collective behaviour deviates from strict propagation invariance. This occurs because each Airy beam exhibits unique spatial shifts and structural variations relative to others, resulting in reduced correlation values for non-matching depths and wavelengths. Consequently, information corresponding to non-matching depths and wavelengths appears more blurred, leading to increased AR and SR. Importantly, for all values of M, LR remains constant since the ensemble variations do not affect the lateral correlation length. Continuous tuning of AR and SR can be achieved by varying M and the weighting parameter γ. For instance, intermediate values of AR and SR between $M = 1$ and $M = 2$ can be achieved by continuously varying γ from 0 to 1. In contrast, previously reported real-time AR tuning methods could not achieve continuous tunability because several AR values required a high intensity contrast between Airy beams [58, 77–79].

The overall imaging process in PEGASASS involves spatially incoherent illumination during optical recording and spatially and temporally incoherent processing during computational reconstruction. In conventional CAI systems using coherent illumination, for a point object, interference occurs between different beams generated by the CPM, leading to both self-interference (from the same point) and mutual interference (between different points). Under spatially incoherent illumination, only self-interference persists for individual points, while intensity addition occurs between different object points. In PEGASASS, for a single point, instead of self-interference, there is only an intensity addition, which makes the system unique. In CAI, for both coherent and spatially incoherent illuminations, for a single point, when there are two Airy beams ψ_1 and ψ_2 generated by the CPM, at the sensor plane, the intensity distribution is given as,

$$I = |\psi_1 + \psi_2|^2, \tag{35}$$

in the region of interaction. For PEGASASS, the case is different, with only an intensity addition given as

$$I = \gamma_1|\psi_1|^2 + \gamma_2|\psi_2|^2. \tag{36}$$

3.4 PEAR-FINCH

The optical configurations of FINCH and PEAR-FINCH are shown in **Figures 13(a) and 13(b)**, respectively. The axial characteristics of FINCH, PEAR-FINCH, and DIS are compared in **Figure 13(c)**. Light from an object point with an amplitude of $\sqrt{I_o}$ is incident on a bifocal lens located at a distance of z_s. The bifocal lens consists of two lenses with focal lengths f_1 and f_2, producing two images. The complex transparency of the bifocal lens is given as $exp(i\Phi_{BFL}) = exp\left(-i\frac{\pi r^2}{\lambda f_1}\right) + exp\left(-i\frac{\pi r^2}{\lambda f_2}\right)$, where $r = \sqrt{x^2 + y^2}$. The complex amplitude incident

on the bifocal lens is given as $C_1\sqrt{I_o}Q(1/z_s)$, where $Q(b) = exp(i\pi br^2/\lambda)$, and C_1 is a complex constant. The complex amplitude after the bifocal lens is given as $C_2\sqrt{I_o}Q(1/z_s)exp\ (i\Phi_{BFL})$, where C_2 is a complex constant. The intensity (I_{PSH}) obtained at the sensor plane located at a distance of z_h is the PSH, which is expressed as,

$$I_{PSH}(\bar{r}_0; z_s) = \left|C_2\sqrt{I_o}Q\left(\frac{1}{z_s}\right)exp\ (i\Phi_{BFL})\otimes Q\left(\frac{1}{z_h}\right)\right|^2$$
$$= C + Q\left(\frac{1}{z_r}\right) + Q\left(\frac{-1}{z_r}\right), \quad (37)$$

where C is a real positive constant. The 3D location information of a single point is present in the distribution of I_{PSH}. A multipoint object consisting of N points can be expressed as,

$$O(\bar{r}) = \sum_{j=1}^{N} a_j \delta(\bar{r} - \bar{r}_j), \quad (38)$$

where a_j is the intensity of the j-th point of the O. FINCH is a linear, shift-invariant system, and therefore, intensity (I_{OH}) is given as,

$$I_{OH} = I_{PSH}\otimes O. \quad (39)$$

Equation (39) can be modified based on Equations (37) – (39) as,

$$I_{OH}(\bar{r}_0; z_s) = \sum_{j=1}^{N} a_j I_{PSH}\left(\bar{r}_0 - \frac{z_h}{z_s}\bar{r}_j; z_s\right). \quad (40)$$

The complex hologram (H_{OH}) is generated as given in Equation (13). This H_{OH} does not contain twin-image and bias noise when numerically backpropagated inside the computer to reconstruct the object. Moreover, for a 2D object located at a distance z_s from the system, H_{OH} is a series of shifted quadratic functions of the form $\sum_j a_j\delta(\bar{r} - z_h\bar{r}_j/z_s)Q(-1/z_r)$. According to the optical configuration, $f_1 = z_s$ and $\frac{1}{f_2} = \frac{1}{z_s} + \frac{2}{z_h}$, so the reconstruction distance is $z_r = z_h/2$. The reconstructed image (I_R) is therefore given as,

$$I_R = \left|H_{OH}\otimes Q\left(\frac{1}{z_r}\right)\right| = \left|\sum_j a_j\delta\left(\bar{r} - \frac{z_h}{z_s}\bar{r}_j\right)Q\left(-\frac{1}{z_r}\right)\otimes Q\left(\frac{1}{z_r}\right)\right| = O\left(\frac{z_h}{z_s}\bar{r}\right). \quad (41)$$

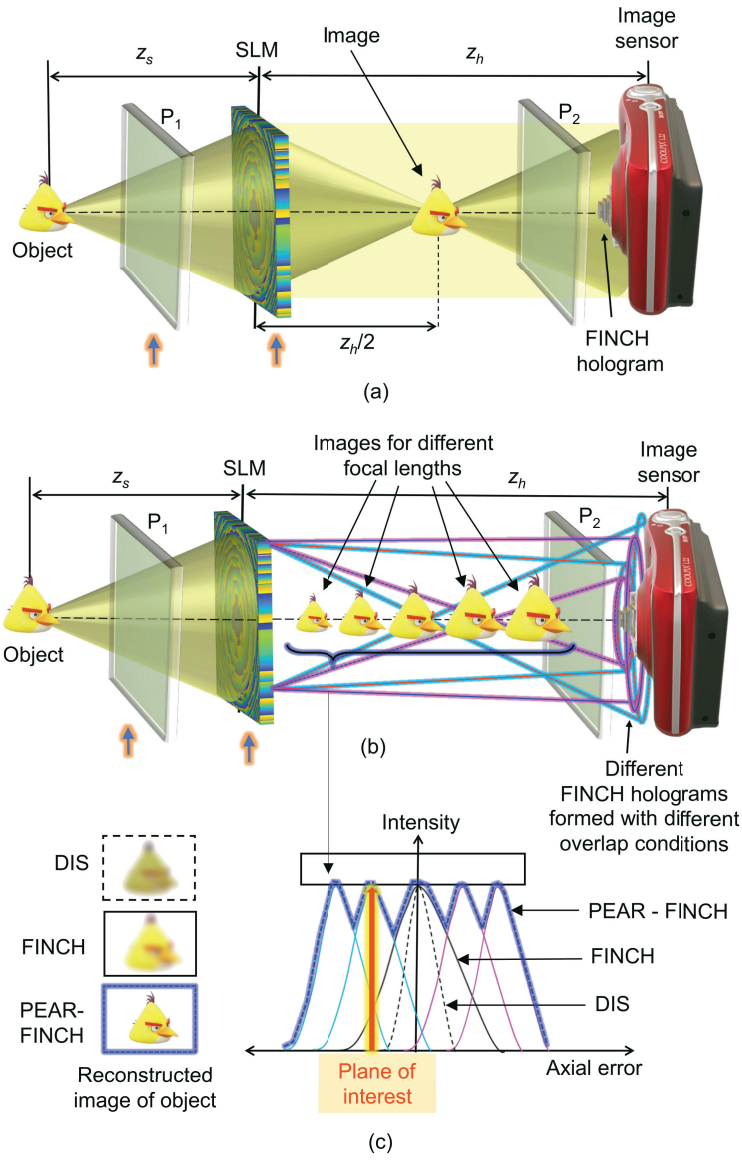

Figure 13. Conceptual illustration of PEAR-FINCH. **(a)** Optical configuration of FINCH. **(b)** Optical configuration of PEAR-FINCH. **(c)** Comparison of the axial characteristics of FINCH, PEAR-FINCH, and DIS. The axial imaging responses for DIS (dashed black line), FINCH (solid black line), and PEAR-FINCH (dashed black line with blue glow) are shown. At the plane of interest, DIS yields the weakest and most blurred result, as it lies outside its axial response curve. FINCH provides a relatively stronger, more focused image than DIS does, since the plane of interest lies within its axial curve, though not at the peak response. PEAR-FINCH enhances imaging by stitching together axial distributions from multiple FINCH focusing conditions, extending the effective FD indicated by the dotted blue-glow line. This results in a highly focused image at the plane of interest, which now aligns with a region of maximal response. The cyan and pink curves represent less optimal focusing regions of FINCH on either side of the optimal condition. z_s and z_h are object and recording distances. P_1 and P_2 are the two polarizers. (Adapted from **Publication IV**)

The FD of FINCH can be described as the allowed tolerance around the calculated value of $z_{r,}$ where the image is reconstructed with a relatively high LR. FINCH, unlike DIS, has a longer FD and a higher LR at the optimal configuration of perfect overlap between the two interfering beams on the sensor plane [98]. When the optical configuration is modified, i.e., when $f_1 \neq z_s$ and $\frac{1}{f_2} \neq \frac{1}{z_s} + \frac{2}{z_h}$, the LR and FD decrease. In the above cases, the magnification of the reconstructed image is also different.

In PEAR-FINCH, a computational stitching approach, involving the summing of the FINCH holograms recorded under different conditions given by the different values of f_2 to extend the FD of FINCH post recording on demand. In PEAR-FINCH, the *synthetic object hologram* (*SOH*) generated by summing the complex holograms is given as,

$$H_{SOH} = \sum_m H_{OH_m}, \tag{42}$$

where m is the index for the hologram number for a particular optical configuration. The H_{SOH} has a long FD, as seen in **Figure 13(c)**, depending upon the number of summed holograms. The above H_{SOH} will generate a reconstruction given as,

$$I_{R1} = |H_{SOH} \otimes Q(1/z_r)| = \left|\sum_m H_{OH_m} \otimes Q(1/z_r)\right| = \left|\sum_m \sum_j a_{m,j} H_{PSH_m} \otimes Q(1/z_r)\right|$$

$$\cong \left|\sum_j a_j \delta\left(\bar{r} - \frac{z_h}{z_s}\bar{r}_j\right) Q(-1/z_r) \otimes Q(1/z_r)\right| + NS(\bar{r}) = \sum_j a_j \delta\left(\bar{r} - \frac{z_h}{z_s}\bar{r}_j\right) + NS(\bar{r})$$

$$= O\left(\frac{z_h}{z_s}\bar{r}\right) + NS(\bar{r}), \tag{43}$$

where $NS(\bar{r})$ is a positive noise distribution created from convolutions between $Q(1/z_r)$ and laterally shifted quadratic phase functions $Q(1/z_{\tilde{r}})$s in which $z_{\tilde{r}} \neq z_r$. Consequently, there are sharp and blurred reconstructions, which are combined, resulting in a lower SNR. This result can be improved by a second step of processing involving the *synthetic point spread hologram* (*SPSH*), which is expressed as,

$$I_{R2} = \left|\left(H_{SOH} \otimes Q(1/z_r)\right) \circledast \left(H_{SPSH} \otimes Q(1/z_r)\right)\right|, \tag{44}$$

where $H_{SPSH} = \sum_m H_{PSH_m}$, and $\circledast$ is a reconstruction operator of one of the reconstruction methods, such as NLR, and LRRA [51, 56]. Under the assumption that a nonlinear correlation can be approximated by a linear correlation, Equation (44) can be written as,

$$
\begin{aligned}
I_{R2} &= \left|\left(\sum_m H_{OH_m} \otimes Q(1/z_r)\right) \circledast \left(\sum_m H_{PSH_m} \otimes Q(1/z_r)\right)\right| \\
&\cong \left|\left(\sum_m H_{OH_m} \circledast \sum_m H_{PSH_m}\right) \otimes [Q(1/z_r) \circledast Q(1/z_r)]\right| \\
&= \left|\left(\sum_m H_{OH_m} \circledast H_{PSH_m} + \sum_m \sum_{n \neq m} H_{OH_m} \circledast H_{PSH_n}\right) \otimes \delta(\bar{r})\right| \\
&= \left|\sum_m \sum_j a_{m,j} H_{PSH_m} \circledast H_{PSH_m}\right| + NS'(\bar{r}) \\
&\cong \sum_m \sum_j a_{m,j} \delta\left(\bar{r} - \frac{z_h}{z_s}\bar{r}_j\right) + NS'(\bar{r}) \\
&\cong M \cdot O\left(\frac{z_h}{z_s}\bar{r}\right) + NS'(\bar{r}),
\end{aligned} \tag{45}
$$

where this time, $NS'(\bar{r})$ is a positive noise distribution created from cross-correlations between OHs and non-corresponding PSHs. Ignoring the scale differences between the various reconstructed images, Equation (45) indicates that the reconstructed image is magnified by a factor of *M,* whereas the noise term $NS'(\bar{r})$ remains approximately the same as in Equation (43), because the sums in Equations (43) and (45) are made over random complex functions distributed uniformly over 2π phase.

CHAPTER 4: RESULTS AND DISCUSSION

4.1 TAP-GSA

The results of simulation studies and optical experiments are presented in the following sections.

4.1.1 Simulation studies

A detailed simulation study of the TAP-GSA was carried out using the *matrix laboratory* (*MATLAB*) [99]. A matrix consisting of 500 × 500 pixels was used, with a pixel size of 10 μm, and illumination wavelength λ = 632.8 nm was used. Since the simulation considered only a single wavelength, there is no distinction between the first and second FINCH configurations. The optical configuration was simulated with parameters z_s = 30 cm, z_h = 60 cm, and $f_1 = \infty$, f_2 = 30 cm, and f_3 = 15 cm. The diameter of the entrance pupil was 2.5 mm. Multiple cases were examined, including RM, PM, and TAP-GSA, with various DoF cases: ~19%, ~36%, ~51%, ~84%, and 100% were evaluated using the ideal phase as the initial guess, and 100% DoF was also tested with a random initial phase. In RM, diffractive lenses with focal distances f_2 and f_3 are multiplied by a binary random matrix [0,1] and its inversion matrix, respectively, and then summed to form the phase matrix. In PM, the ideal complex function, obtained by summing the phases of the two diffractive lenses, was used as the modulation function. In TAP-GSA, a uniform amplitude constraint is applied in the mask plane, and the amplitude obtained at the sensor plane for PM is used as a constraint on the sensor plane. The DoF of the phase constraint at the sensor plane was varied from 100% down to ~19%, and each phase mask was computed after 100 iterations. **Figure 14** shows that increasing the DoF makes the amplitude at the mask plane more uniform, but also increases noise in the hologram. Consequently, reconstructions obtained in higher-DoF cases exhibit stronger noise. A noteworthy observation from **Figure 14** is that minimum DoF cases, although lacking a uniform amplitude at the mask plane, produce a hologram almost identical to the ideal case. This is an interesting observation, as implementing the minimum DoF case does not require PM, yields a higher SNR, and improves light throughput by 200%.

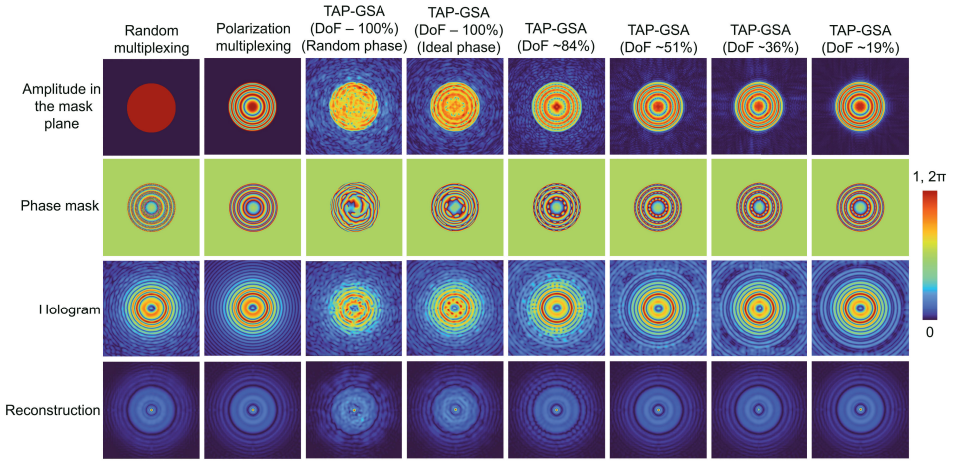

Figure 14. Row 1 – Amplitude in the mask plane, Row 2 – phase mask, Row 3 – hologram, and Row 4 – reconstruction result shown for RM, PM, and TAP-GSA with different DoFs of 100% (random phase), 100% (ideal phase), ~84%, ~51%, ~36%, and ~19%. (Adapted from **Publication I**)

To further validate the approach, simulations were performed on a test object *computational imaging and processing in high resolution* (*CIPHR*). **Figure 15** presents the simulated holograms with phase shift values $\theta = 0$, $2\pi/3$, and $4\pi/3$, the resulting complex hologram magnitude and phase, and the reconstructed images of the object obtained via Fresnel back-propagation for the following cases: PM, RM, and TAP-GSA with a DoF of ~10%. The reconstruction results show that TAP-GSA yields significantly lower reconstruction noise than RM, and the sharpness is slightly lower than that of PM. As expected, the resolution in all FINCH cases is 1.5 times higher than that of DIS, with the same NA.

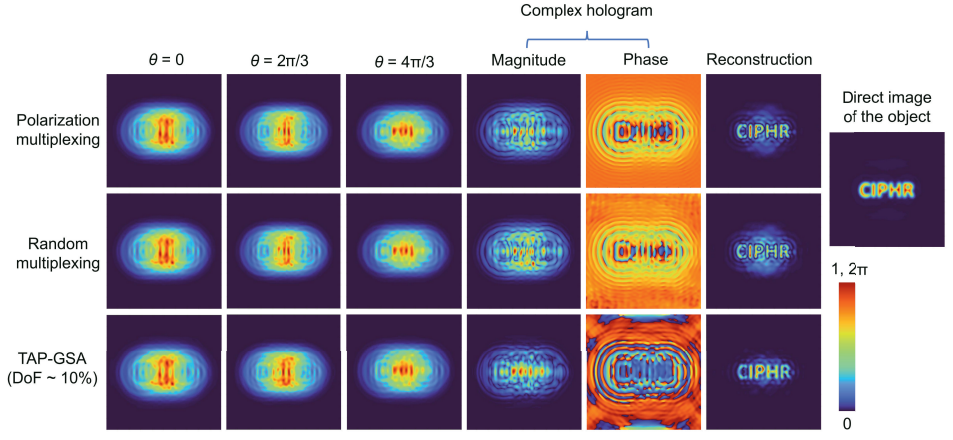

Figure 15. Columns 1 to 3 – Phase-shifted OHs with phase shift values $\theta = 0$, $2\pi/3$, and $4\pi/3$, Columns 4 and 5 – magnitude and phase of the complex hologram, and Column 6 – reconstruction results by Fresnel back-propagation shown for PM, RM, and TAP-GSA. The direct image of the test object 'CIPHR' is shown in the RHS. (Adapted from **Publication I**)

Next, to verify the behaviour of TAP-GSA, the simulations were carried out by changing the simulation parameters for PM, RM, and TAP-GSA with DoFs of 0%, ~25%, ~50%, ~75%, and 100% with the ideal initial guess phase and random initial guess phase. In this simulation, a matrix consisting of 1200×1200 pixels was used with a pixel size of 8 μm and a wavelength λ = 632.8 nm. The optical configuration was z_s = 1000 cm, z_h = 17.8 cm, and f_1 = 1000, f_2 = 8.9 cm. The corresponding simulation results are shown in **Figure 16.** In TAP-GSA, except for the case with an initial guess of a random matrix, all other cases achieved an SNR higher than that of the RM method. This behaviour differs from the results shown in **Figure 14**.

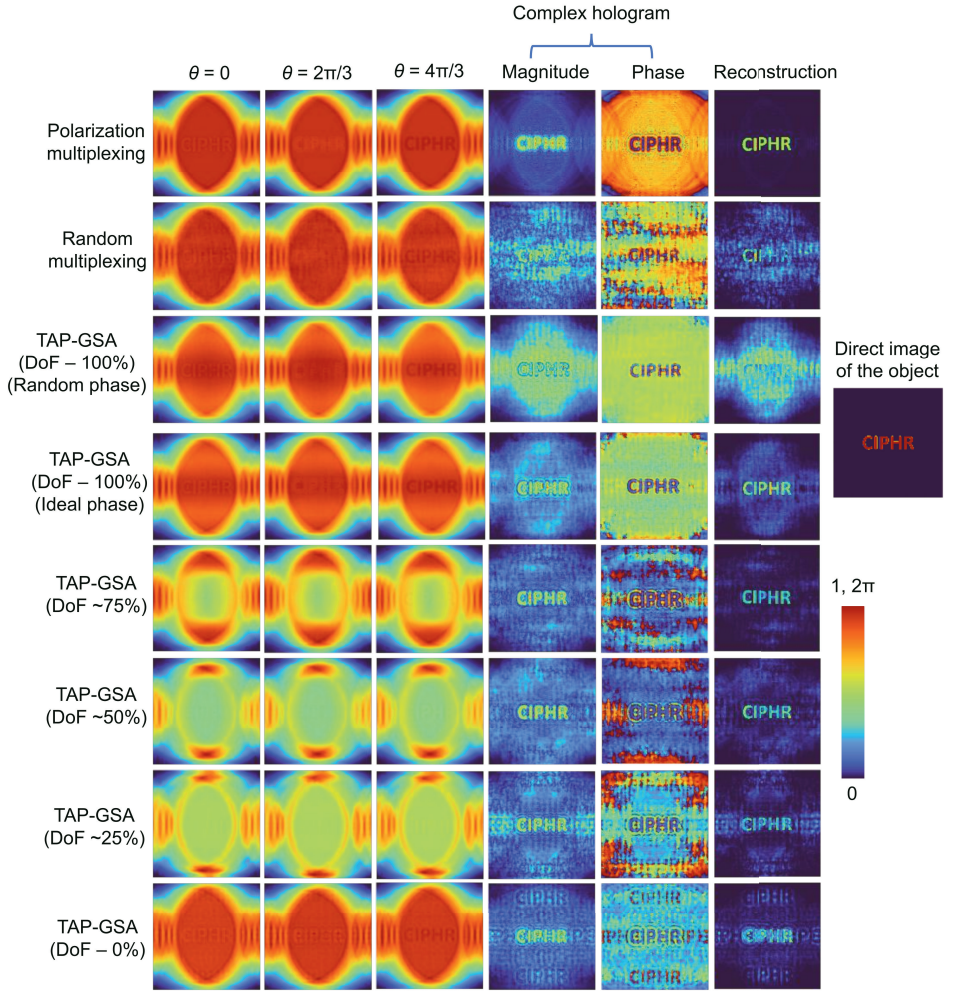

Figure 16. Columns 1 to 3 – Phase-shifted OHs with phase shift values θ = 0, 2π/3, and 4π/3, Columns 4 and 5 – magnitude and phase of the complex hologram, and Column 6 – reconstruction results by Fresnel back-propagation shown for PM, RM, and TAP-GSA with different DoFs of 100% (random phase), 100% (ideal phase), ~75%, ~50%, ~25% and 0%. The direct image of the test object 'CIPHR' is shown in the RHS. (Adapted from **Publication I**)

4.1.2 Experimental studies

The experimental setup for demonstrating the concept of FINCH was constructed on an optical table, and its photograph is shown in **Figure 17**. The setup includes the following optical components from Thorlabs: Element 1 – M660L4 LED with 940 mW power, operating at a wavelength of λ = 660 nm, and a bandwidth of $\Delta\lambda$ = 20 nm; Element 2 – LED power controller; Element 3 – ID50/M standard iris, Ø50.0 mm max aperture; Element 4 – N-BK7 Ø1" biconvex refractive lens with a focal length (f = 5 cm); Element 5 – Ø1" linear polarizer with N-BK7 windows; Element 6 – test object Ø1" pinhole of size (100 µm) or digit '5' with a grating having a line width of 15.63 µm from group 5 in R1DS1N Negative USAF test target; Element 7 – ID20/M standard iris, Ø20.0 mm max aperture; Element 8 – N-BK7 Ø1" biconvex refractive lens with a focal length (f = 5 cm); Element 9 – BS013 50:50 non-polarizing beam splitter cube; Element 10 – Exulus HD2 SLM with 1920 × 1200 pixels and having a pixel size of 8 µm; Element 11 – Ø1" linear polarizer with N-BK7 windows; Element 12 – FLH633-5 band pass filter with a wavelength of λ = 633 nm and a bandwidth of $\Delta\lambda$ = 5 nm and Element 13 – Zelux CS165MU/M monochrome image sensor with 1440 × 1080 pixels and having a pixel size of ~3.5 µm.

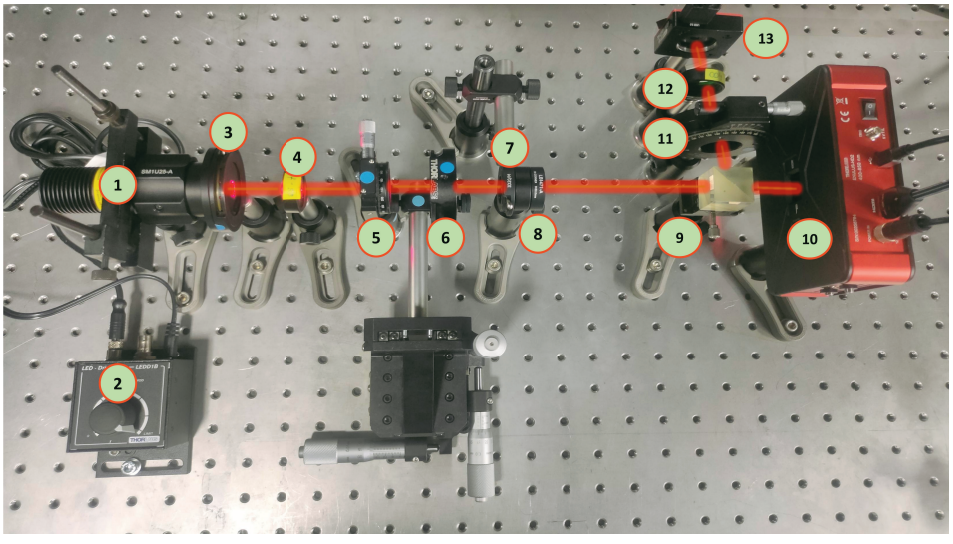

Figure 17. Photograph of the experimental setup used for demonstration. (1) LED, (2) LED power controller, (3) iris, (4) refractive lens (f = 5 cm), (5) first polarizer (P_1), (6) object/pinhole, (7) iris, (8) refractive lens (f = 5 cm), (9) beam splitter, (10) SLM, (11) second polarizer (P_2), (12) bandpass filter, and (13) image sensor. The beam path from the LED to the image sensor is indicated in red. (Adapted from **Publication I**)

The LED light critically illuminated the object through a biconvex refractive lens. An iris placed after the LED controlled the illumination diameter. An optical power controller was used to stabilize and adjust the LED output. Two objects were used for the experiments: a 100 μm pinhole and a digit '5' with a grating. The first polarizer, P_1, was positioned before the SLM. For RM and TAP-GSA, P_1 was aligned with the SLM's active axis. For PM, P_1 was oriented at 45° relative to the SLM active axis. The light from the object was collected by a biconvex refractive lens placed at a distance z_s = 5 cm from the object. An iris was used together with this lens to control the system's effective NA. The collected light was propagated to a beam splitter and then to the SLM. The modulated light reflected from the SLM propagated toward the image sensor. The distance from the SLM to the image sensor is z_h = 17.8 cm. The second polarizer, P_2, was positioned after the SLM, and for PM, it was oriented at 45° relative to the SLM's active axis. For the RM and TAP-GSA cases, P_2 was oriented along the SLM's active axis. To enhance temporal coherence and improve fringe visibility, a narrow bandpass filter was placed before the sensor. A diffractive lens with a focal length of f = 17.8 cm was displayed on the SLM to capture the best focus direct images of the test objects. The phase masks for both FINCH configurations, maximum optical path difference and reduced optical path difference, were computed and displayed on the SLM. For the maximum optical path difference configuration, PM, RM, and TAP-GSA were evaluated. For the reduced optical path difference case, RM and TAP-GSA were compared. For the main experiments, the LED current was set to 0.2 A, and holograms and direct images were recorded using the sensor's full dynamic range (1024 levels). The phase masks shown in **Figures 18, 23, and 25** were designed in MATLAB [99] based on the SLM specifications (operating wavelength range of 400–850 nm, pixel size of 8 μm, and panel resolution of 1920×1200). The designed phase masks were exported as bitmap images compatible with the SLM controller. The SLM was connected directly to the computer and operated using the Thorlabs control software, which allows bitmap phase masks to be loaded and displayed without additional preprocessing. During recording, the phase masks were displayed sequentially. After each mask was displayed on the SLM, a short stabilization period of 2–3 seconds was allowed before capturing the corresponding hologram with the image sensor. This ensured stable SLM rendering and consistent hologram formation. The experimentally recorded data were subsequently processed in MATLAB [99], where the computational reconstruction was performed, and the figures were generated, as shown in the upcoming Sections 4.1.2.1 and 4.1.2.2.

4.1.2.1 Configuration 1 – FINCH with maximum optical path difference

In this configuration, two diffractive lenses with the focal lengths of 8.9 cm and infinity were multiplexed using RM and TAP-GSA (DoF ~10%). The phase shift values $\theta = 0, 2\pi/3$, and $4\pi/3$ were applied to one of the two multiplexed lenses (in this case, the 8.9 cm diffractive lens). For PM, a single diffractive lens with a

focal length of 8.9 cm was designed using phase shifts $\theta = 0$, $2\pi/3$, and $4\pi/3$. The designed phase masks for RM, TAP-GSA (DoF ~10%), and PM, with phase shift values $\theta = 0$, $2\pi/3$, and $4\pi/3$, are shown in **Figure 18**.

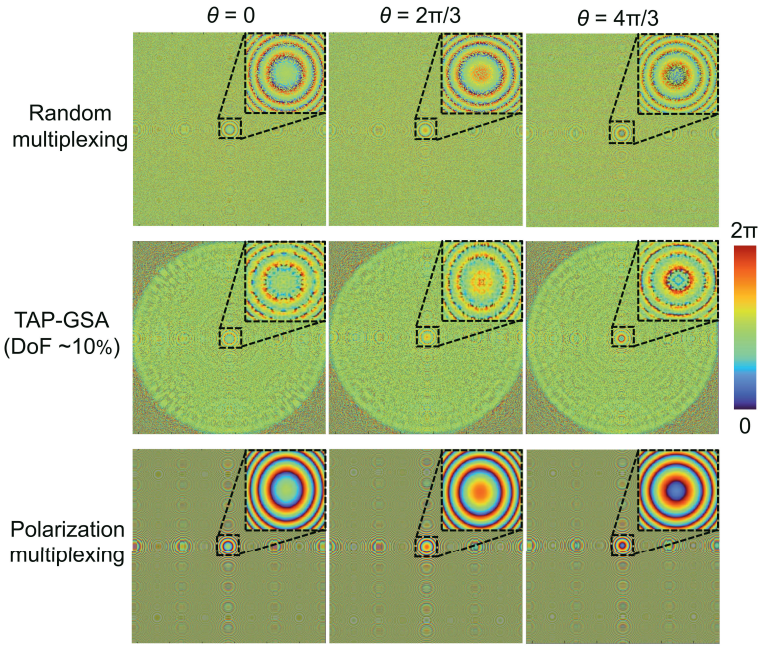

Figure 18. Phase masks for FINCH with maximum optical path difference. Row 1 – RM, Row 2 – TAP-GSA (DoF ~10%), and Row 3 – PM, shown for phase shift values $\theta = 0$, $2\pi/3$, and $4\pi/3$. (Adapted from **Publication I**)

For RM and TAP-GSA (DoF ~10%), both polarizers, P_1 and P_2, used in the experimental setup before and after the SLM, were aligned along the SLM's active axis. For PM, both polarizers, P_1 and P_2, were oriented at 45° relative to the SLM's active axis. The first polarizer, P_1, ensures that approximately 50% of the incident light is modulated by the phase mask displayed on the SLM, while the remaining light remains unmodulated. The second polarizer, P_2, positioned after the SLM, was also aligned at 45° relative to the SLM's active axis. This configuration enables interference between the modulated and unmodulated light, which is essential for FINCH hologram formation. The effective diameter of the SLM is approximately 7 mm. Initially, the 100 μm pinhole is used as the test object. The phase masks shown in **Figure 18** are sequentially displayed on the SLM, and the corresponding OHs are recorded. **Figure 19** presents the experimentally recorded holograms with phase shift values $\theta = 0$, $2\pi/3$, and $4\pi/3$; the resulting complex hologram phase and magnitude; and the reconstructed images of the object obtained via Fresnel back-propagation for the following cases: RM, TAP-GSA (DoF ~10%), and PM. The exposure times required to record the hologram of the test object, a 100 μm pinhole, with a full dynamic range for RM, TAP-GSA (DoF ~10%), and PM were 615, 515, and 983 *ms,* respectively.

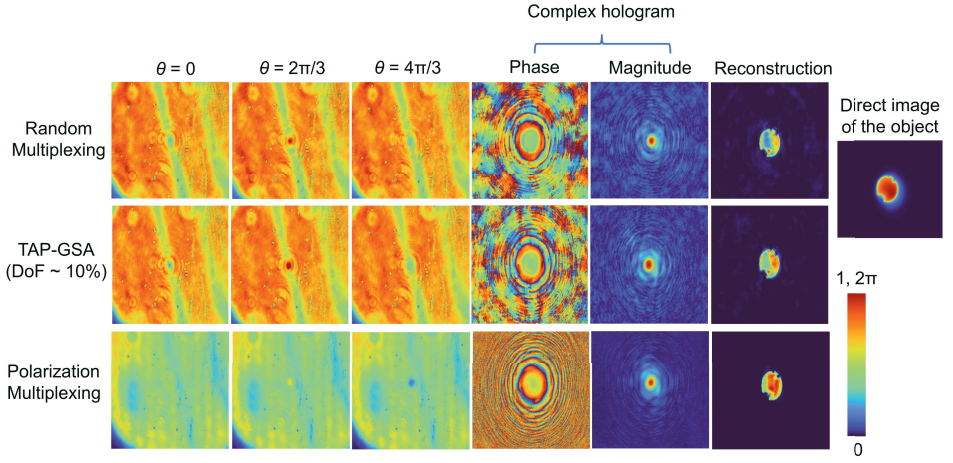

Figure 19. Columns 1 to 3 – Phase-shifted OHs with phase shift values $\theta = 0$, $2\pi/3$, and $4\pi/3$, Columns 4 and 5 – phase and magnitude of the complex hologram, and Column 6 – reconstruction results by Fresnel back-propagation shown for RM, TAP-GSA (DoF ~10%), and PM. The direct image of the test object, a 100 µm pinhole, is shown on the RHS. (Adapted from **Publication I**)

To further validate the approach, experiments were performed using a test object, the digit '5', with a grating. **Figure 20** presents the experimentally recorded holograms with phase shifts $\theta = 0$, $2\pi/3$, and $4\pi/3$, the resulting complex hologram phase and magnitude, and the reconstructed object images obtained via Fresnel back-propagation, for the following cases: RM, TAP-GSA (DoF ~10%), and PM. The exposure times required to record the hologram of the test object digit '5' with a grating at full dynamic range for RM, TAP-GSA (DoF ~10%), and PM were 440, 381, and 861 *ms,* respectively.

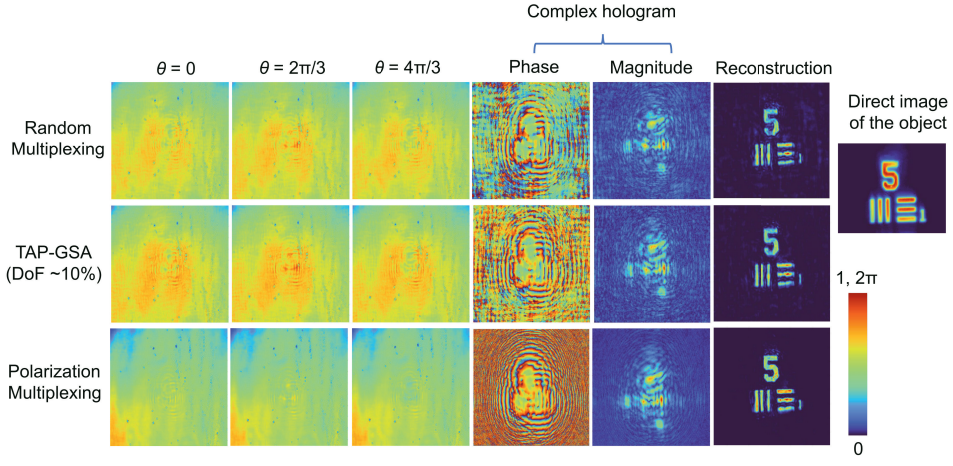

Figure 20. Columns 1 to 3 – Phase-shifted OHs with phase shift values $\theta = 0$, $2\pi/3$, and $4\pi/3$, Columns 4 and 5 – phase and magnitude of the complex hologram, and Column 6 – reconstruction results by Fresnel back-propagation shown for RM, TAP-GSA (DoF ~10%), and PM. The direct image of the test object (the digit '5' with a grating) is shown on the RHS. (Adapted from **Publication I**)

For both test objects, a 100 µm pinhole and digit '5' with a grating, the optimal reconstruction distance for all three multiplexing methods, RM, TAP-GSA (DoF ~10%), and PM, was ~9 cm. The *average background noise* (*ABN*) was estimated in MATLAB [99] using the equation $ABN = \frac{\left\{\sum_{i=1,j=1}^{N,M} I_R(x_i,y_j)\right\}}{N\times M}$, where $I_R(x_i, y_j)$ is the value of pixel (*i,j*) if and only if pixel (*i,j*) is in the background of the image. For the test object, a 100 µm pinhole, the ABN values for RM, TAP-GSA (DoF ~10%), and PM are 3.27×10^{-3}, 2.32×10^{-3}, and 0.41×10^{-3}, respectively. For the test object digit '5' with a grating, the ABN of RM, TAP-GSA (DoF ~10%), and PM are 2.91×10^{-3}, 2.37×10^{-3}, and 0.62×10^{-3}, respectively.

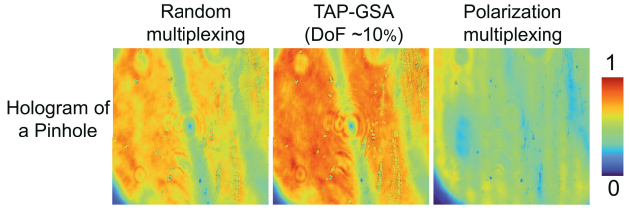

Figure 21. Recorded OHs corresponding to the test object (100 µm pinhole) with an exposure time of 1587.4 *ms*, shown for RM, TAP-GSA (DoF ~10%), and PM. (Adapted from **Publication I**)

Among the three methods, PM provides the lowest ABN and hence the highest SNR, while TAP-GSA consistently outperforms RM. Further, TAP-GSA requires the lowest optical power, making it more efficient than both RM and PM. To compare the light efficiency of all methods under identical conditions, OHs corresponding to the test object (100 µm pinhole) are recorded for RM, TAP-GSA (DoF ~10%), and PM, with the same exposure time of 1587.4 ms, as shown in **Figure 21**. These results clearly demonstrate that RM and PM demand significantly higher optical power than TAP-GSA. The ABN values for the direct images of the two test objects, the 100 µm pinhole and the digit '5' with a grating, were 0.15×10^{-3} and 0.53×10^{-3}, respectively.

One of the main advantages of FINCH over DIS is its capability to image objects with improved resolution. To verify whether this advantage is preserved with the TAP-GSA (DoF ~ 10%), the diameter of the diffractive lens displayed on the SLM was limited to ~ 1.5 mm, ensuring that the two test objects could not be fully resolved by the DIS. The same diameter constraint was applied to the phase mask generated with TAP-GSA (DoF ~10%). The DIS results and the reconstruction results of TAP-GSA (DoF ~10%) for both test objects, a 100 µm pinhole and the digit '5' with a grating, are shown in **Figure 22.** The results clearly demonstrate that the resolution-enhancement characteristic of FINCH is fully preserved with TAP-GSA, confirming that TAP-GSA maintains FINCH's improved-resolution imaging capability compared to DIS.

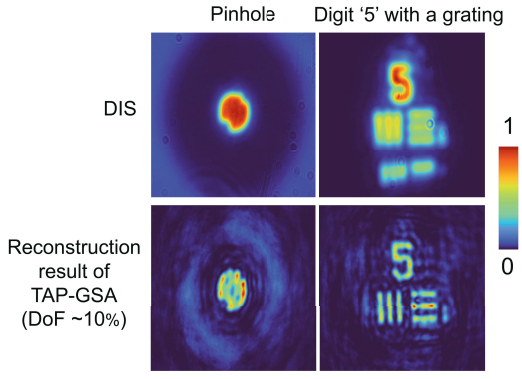

Figure 22. Row 1 – DIS results and Row 2 – reconstruction results of TAP-GSA (DoF ~10%), shown for the test objects 100 µm pinhole and digit '5' with a grating. (Adapted from **Publication I**)

4.1.2.2 Configuration 2 – FINCH with reduced optical path difference

For this configuration, two diffractive lenses with focal lengths of 14 cm and 25 cm were designed and multiplexed using RM and TAP-GSA (DoF ~30%). The phase shift values $\theta = 0$, $2\pi/3$, and $4\pi/3$ are applied to one of the two multiplexed lenses (in this case, a 14 cm diffractive lens). The designed phase masks for RM and TAP-GSA (DoF ~30%) with phase shift values $\theta = 0$, $2\pi/3$, and $4\pi/3$ are shown in **Figure 23**. As RM and TAP-GSA (DoF ~30%) are employed in this configuration, both polarizers, P_1 and P_2, were aligned along the SLM's active axis. Again, the 100 µm pinhole was first used as the test object. The phase masks shown in **Figure 23** are sequentially displayed on the SLM, and the corresponding OHs are recorded.

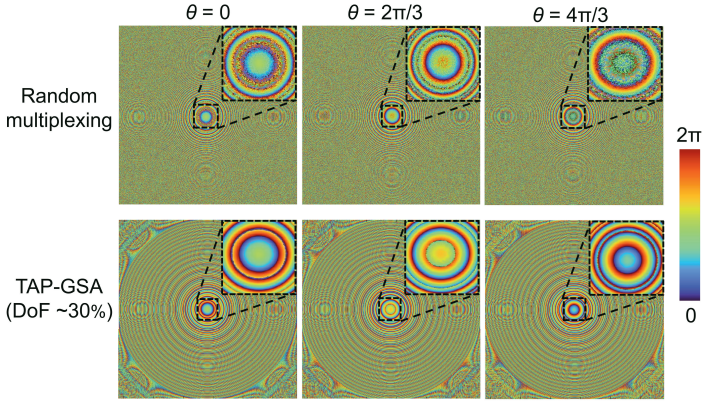

Figure 23. Phase masks of the FINCH with reduced optical path difference. Row 1 – RM and Row 2 – TAP-GSA (DoF ~30%) shown for phase shift values $\theta = 0$, $2\pi/3$, and $4\pi/3$. (Adapted from **Publication I**)

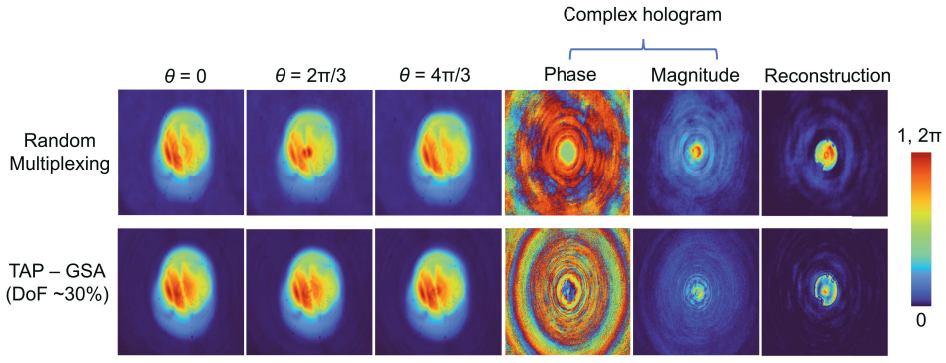

Figure 24. Columns 1 to 3 – Phase-shifted OHs with phase shift values $\theta = 0$, $2\pi/3$, and $4\pi/3$, Columns 4 and 5 – phase and magnitude of the complex hologram, and Column 6 – reconstruction results by Fresnel back-propagation shown for RM and TAP-GSA (DoF ~30%). (Adapted from **Publication I**)

Figure 24 presents the experimentally recorded holograms with phase shift values $\theta = 0$, $2\pi/3$, and $4\pi/3$, the resulting phase and magnitude of the complex hologram, and the reconstructed images of the object obtained via Fresnel back-propagation, for the following cases: RM and TAP-GSA (DoF ~30%). For both multiplexing approaches, RM and TAP-GSA (DoF ~30%), the optimal reconstruction distance was ~7 cm. The exposure times required to record the hologram of the test object, a 100 μm pinhole with the same dynamic range for RM and TAP-GSA (DoF ~30%), were 71 and 42 *ms,* respectively, representing an improvement of ~1.7 times. The ABNs are 2.36×10^{-3} and 2.26×10^{-3} for RM and TAP-GSA (DoF ~30%), respectively.

To further evaluate performance, the recording configuration was modified by selecting diffractive lenses with focal lengths of 11 cm and 46 cm and multiplexing them using RM and TAP-GSA, with the following DoF cases: ~30%, ~56%, ~75%, ~89%, and ~98%. For each DoF case, the phase mask is synthesized after 100 iterations. As expected, the similarity between the TAP-GSA-generated phase masks and the ideal phase function decreases with increasing DoF. The designed phase masks of RM and TAP-GSA for DoF cases of ~30%, ~56%, ~75%, ~89%, and ~98%, with phase shift values $\theta = 0$, $2\pi/3$, and $4\pi/3$, are shown in **Figure 25**.

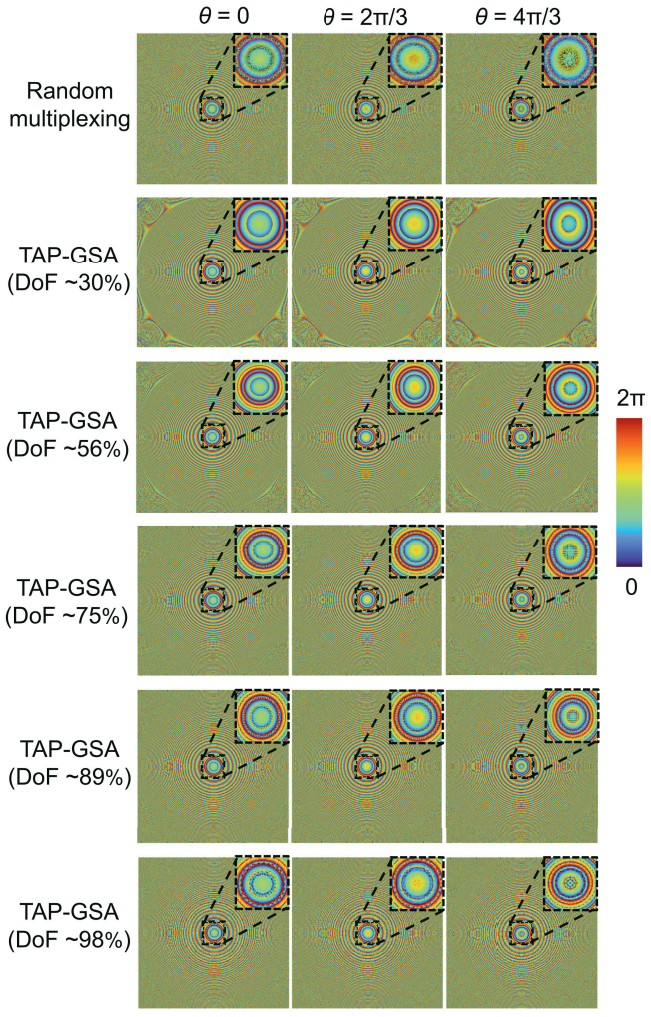

Figure 25. Phase masks of the FINCH with reduced optical path difference. Column 1 – phase shift value $\theta = 0$, Column 2 – phase shift value $\theta = 2\pi/3$, and Column 3 – phase shift value $\theta = 4\pi/3$ shown for RM, and TAP-GSA with DoF cases ~30%, ~56%, ~75%, ~89%, and ~98%. (Adapted from **Publication I**)

For this evaluation, the digit '5' with a grating is used as the test object. The phase masks shown in **Figure 25** are sequentially displayed on the SLM, and the corresponding OHs are recorded. **Figure 26** presents the experimentally recorded holograms with phase shift values $\theta = 0$, $2\pi/3$, and $4\pi/3$, the resulting complex hologram phase and magnitude, and the reconstructed images of the object obtained via Fresnel back-propagation, for the following cases: RM and TAP-GSA with DoF cases ~30%, ~56%, ~75%, ~89%, and ~98%. The optimal reconstruction distance for RM and TAP-GSA with different DoF cases was approximately 30 cm. The exposure times required to record the hologram of the test object digit '5' with a grating, using the same dynamic range for RM and TAP-GSA in

different DoF cases, were 72 and 48 *ms,* respectively. In TAP-GSA, varying the DoF resulted in only mild to no change in exposure time. The ABN values for RM and TAP-GSA with DoF cases of ~30%, 56%, 75%, 89%, and 98% were 22.9×10^{-3}, 4.8×10^{-3}, 2.3×10^{-3}, 1.7×10^{-3}, 4.0×10^{-3}, and 5.3×10^{-3}, respectively.

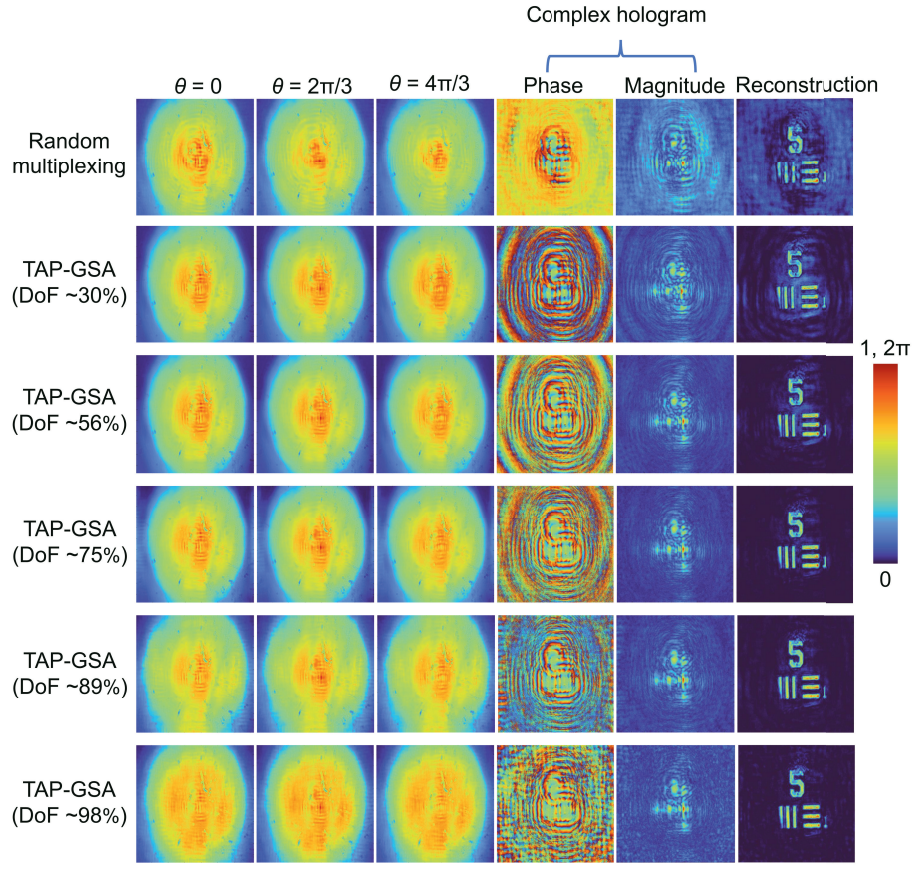

Figure 26. Columns 1 to 3 – Phase-shifted OHs with phase shift values $\theta = 0$, $2\pi/3$, and $4\pi/3$, Columns 4 and 5 – phase and magnitude of the complex hologram, and Column 6 – reconstruction results by Fresnel back-propagation shown for RM and TAP-GSA with DoF cases ~30%, ~56%, ~75%, ~89%, and ~98%. (Adapted from **Publication I**)

Considering the reconstruction results for both test objects, a 100 µm pinhole and the digit '5' with a grating, it is found that TAP-GSA consistently offers a significant improvement in SNR compared to RM, with a lower ABN. Since a significant difference in noise levels between RM and TAP-GSA was observed for a small object, such as a 100 µm pinhole, the noise difference is expected to increase for more complex objects. While ABN increased for RM when the object complexity increased, TAP-GSA maintained the same noise level. The values of the exposure time and ABN for FINCH with reduced optical path difference and maximum optical path difference, and DIS for both the test objects, a 100 µm pinhole and digit '5' with a grating, are summarized in **Tables 1 and 2**.

Table 1. Exposure time and ABN for FINCH with reduced and maximum path optical differences for RM, TAP-GSA, and PM, and DIS for a 100 µm pinhole test object. (Adapted from **Publication I**)

Properties	**FINCH reduced optical path difference (100 µm pinhole)**		**FINCH maximum optical path difference (100 µm pinhole)**			**DIS (100 µm pinhole)**
	RM	TAP-GSA (DoF ~30%)	RM	TAP-GSA (DoF ~10%)	PM	
Exposure time (*ms*)	71	42	615	515	983	2
ABN ($\times 10^{-3}$)	2.36	2.26	3.27	2.32	0.41	0.15

Table 2. Exposure time and ABN for FINCH with reduced and maximum path optical differences for RM, TAP-GSA, and PM, and DIS for the digit '5' with a grating test object. (Adapted from **Publication I**)

Properties	**FINCH reduced optical path difference (digit '5' with a grating)**						**FINCH maximum optical path difference (digit '5' with a grating)**			**DIS (digit '5' with a grating)**
	RM	TAP-GSA (DoF ~30%)	TAP-GSA (DoF ~56%)	TAP-GSA (DoF ~75%)	TAP-GSA (DoF ~89%)	TAP-GSA (DoF ~98%)	RM	TAP-GSA (DoF ~10%)	PM	
Exposure time (*ms*)	72	48	48	48	48	48	440	381	861	3
ABN ($\times 10^{-3}$)	22.9	4.8	2.3	1.7	4	5.3	2.91	2.37	0.62	0.53

4.1.2.3 Fabrication and testing of phase masks

The phase masks designed in MATLAB [99] for FINCH with reduced optical path difference (f_1 = 14 cm and f_2 = 25 cm) were first binarized with a pixel size of 8 µm and a length of 9.6 mm. The binary phase masks were then converted from bitmap file format to *Graphic Design System* (*GDSII*) file format using the trial version of LinkCAD software [91]. The binary phase masks corresponding to RM and TAP-GSA (DoF ~30%) are shown in Row 1 of **Figure 27**. The photoresist thickness 't' was optimized for a wavelength of λ = 650 nm using $t = \lambda/2(n\text{-}1)$, where n is the refractive index of the photoresist. Device fabrication was performed using standard photolithography in an ISO 5 cleanroom. The exposure was carried out with a Maskless Aligner (Heidelberg Instruments, µMLA 100, Germany) using a light source at 390 nm with dose control. A positive photoresist (AR-P 3510T, Allresist, Germany) was spin-coated on precleaned glass substrates (4000 rpm, 60 s) and softly baked on a hot plate at 100 °C for 60 s. An adhesion promoter (AR 300-80 new, Allresist, Germany) was applied before coating, and the developer AR 300-44 (Allresist, Germany) was used to develop the UV-irradiated structures.

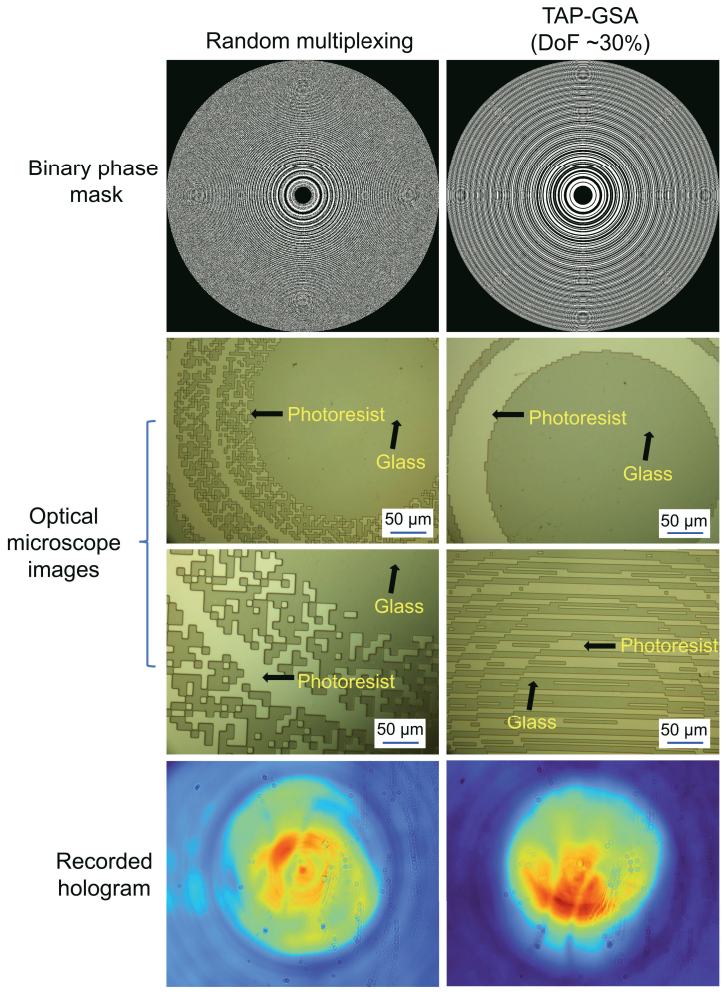

Figure 27. Row 1 – Binary phase mask corresponding to FINCH with reduced optical path difference, Rows 2 and 3 – optical microscope images of the binary phase mask, and Row 4 – Recorded OHs corresponding to the test object (100 µm pinhole) shown for RM and TAP-GSA (DoF ~30%). (Adapted from **Publication I**)

Optical microscope images of the fabricated RM and TAP-GSA (DoF ~30%) masks are shown in Rows 2 and 3 of **Figure 27**, respectively. The fabricated devices were tested in the same optical setup shown in **Figure 17**. In this setup, the beam splitter before the SLM divides the incoming beam into two paths. The fabricated devices were mounted perpendicular to the SLM position, and the image sensor was moved to record the corresponding OHs. The recorded OHs for the test object, a 100 µm pinhole, for RM and TAP-GSA (DoF ~30%) are shown in Row 4 of **Figure 27**. The experimental results clearly demonstrate that TAP-GSA (DoF ~30%) exhibits a higher light concentration than the RM. Since each fabricated mask produces only a single-shot OH, phase-shift-based reconstruction cannot be performed in this experiment. Nevertheless, the similarity of

the OH corresponding to TAP-GSA (DoF ~30%) to the OHs of a 100 μm pinhole shown in Row 2 of **Figure 24** is higher than the similarity of the OH corresponding to RM to the OHs of a 100 μm pinhole shown in Row 1 of **Figure 24**. This confirms that the optical performance of the fabricated devices with TAP-GSA more closely matches the results obtained using the SLM.

4.2 INCHIS

The results of simulation studies and optical experiments of INCHIS are presented in the following sections.

4.2.1 Simulation studies

4.2.1.1 INCHIS-H1

Simulation studies were performed in MATLAB with a matrix size of 500 × 500 pixels, pixel size $\Delta = 8$ μm, wavelength $\lambda = 632.8$ nm, and $z_h = 30$ cm [99]. Two test objects, the logo of CIPHR and the *University of Tartu* (*UT*), were used, as shown in **Figure 28**. In this simulation study, these objects will be referred to as O1 and O2, respectively. The objects O1 and O2 were positioned at two different axial locations, $z_s = 30$ cm and $z_s = 27$ cm. A diffractive FZP was designed with a focal length that intentionally violates the imaging condition $\frac{1}{f} \neq \frac{1}{z_s} + \frac{1}{z_h}$. Next, a diffractive axicon with a period of 96 μm was designed to generate a Bessel beam. The CPMs of lens and axicon were combined with different strengths using the variables T_1 and T_2 to generate the hybrid CPMs. Five combinations of mask strengths were simulated by varying T_1 and T_2: (T_1, T_2) = (1, 0), (0.75, 0.25), (0.5, 0.5), (0.25, 0.75), (0, 1), representing a continuous shift from pure lens to pure axicon characteristics. The first and last cases correspond to the pure lens and pure axicon, while the intermediate combinations represent hybrid states. The corresponding amplitude and phase distributions of the five cases are shown in **Figure 29**. As observed, the hybrid cases contain both amplitude and phase components, whereas the pure axicon and pure lens are phase-only elements.

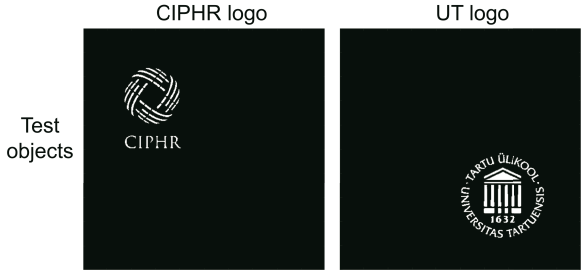

Figure 28. Logos of **(a)** CIPHR, and **(b)** UT, used as test objects O1 and O2 located at $z_s = 30$ cm and $z_s = 27$ cm, respectively. (Adapted from **Publication II**)

The 3D simulation results of INCHIS-H1 are shown in **Figure 30**. The I_{PSF} (z_s = 30 cm), I_{PSF} (z_s = 27 cm), I_{OID} and their reconstruction results at the two axial locations I_R (z_s = 30 cm) and I_R (z_s = 27 cm) using LRRA for (T_1 = 1, T_2 = 0), (T_1 = 0.75, T_2 = 0.25), (T_1 = 0.5, T_2 = 0.5), (T_1 = 0.25, T_2 = 0.75) and (T_1 = 0, T_2 = 1) are shown in rows 1–5 respectively in **Figure 30(a)**. Comparing the reconstruction results for the different cases, it is observed that as the values of T_1 and T_2 are tuned to transform the lens into an axicon through hybrid states, the AR decreased. For I_R (z_s = 30 cm), it is observed that O2 is defocused with a pure lens, but the focus improves as the system is shifted towards a pure axicon. The same can be observed for I_R (z_s = 27 cm), where the object O1 appears defocused with a pure lens, and gradually improves as the system is shifted towards a pure axicon.

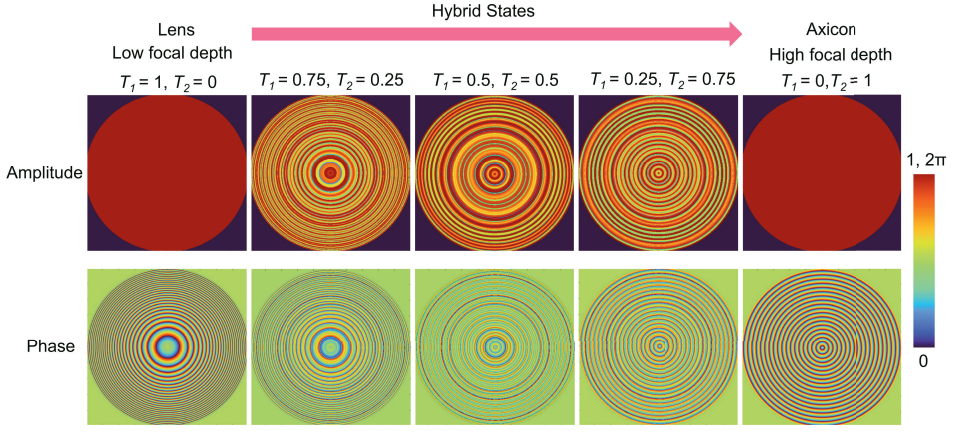

Figure 29. Row 1 – Amplitude and Row 2 – phase of the CPMs corresponding to the lens, hybrid states, and axicon, respectively. (Adapted from **Publication II**)

The above effect can also be achieved by increasing the number of beams with distinct axial characteristics, rather than tuning the strengths of the two interfering beams. The optimal values for reconstruction using LRRA, for the above cases, were $\alpha = 0$, $0.5 \leq \beta \leq 0.6$, and $4 \leq n \leq 10$. Axial intensity distributions were calculated by correlating the I_{PSF} (z_s = 30 cm) with I_{PSF} (20 cm $\leq z_s \leq$ 30 cm) in steps of 1 mm. NLR with parameters $\alpha = 0$ and $\beta = 1$ was used for this calculation. NLR was chosen since it is computationally stable and does not require calibration for varying intensity distributions, unlike LRRA. The resulting axial profiles for the five cases are plotted and shown in **Figure 30(b)**. As observed in the plot, AR varies nonlinearly with T_1 and T_2. The axial distribution for the case (T_1 = 0, T_2 = 1) resembled the typical axial intensity distribution of an axicon [100, 101]. The axial distribution for the case (T_1 = 1, T_2 = 0) resembled that of a lens. In between these two cases, mixed axial properties formed by the combination of different degrees of lens and axicon are obtained. The area under the axial curve is inversely related to the AR. The normalized areas under the axial curves for different T_1 and T_2 combinations are plotted as a bar chart, as

shown in **Figure 30(c)**. The plot quantitatively shows the difference in AR for different combinations of T_1 and T_2, with a maximum AR for a lens (T_1 = 1, T_2 = 0) and a minimum AR for an axicon (T_1 = 0, T_2 = 1).

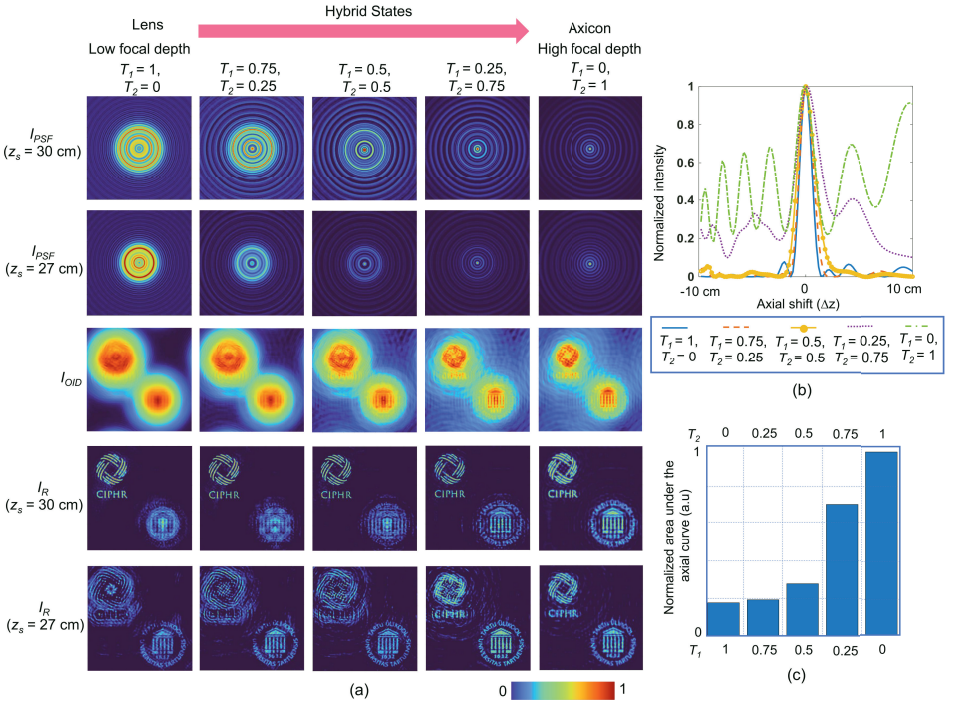

Figure 30. INCHIS-H1: (a) Row 1 – $I_{PSF}(z_s = 30$ cm), Row 2 – $I_{PSF}(z_s = 27$ cm), Row 3 – I_{OID}, and Row 4 and Row 5 reconstruction results by LRRA at the two axial locations I_R (z_s = 30 cm) and I_R (z_s = 27 cm), shown for lens, hybrid states, and axicon, respectively. **(b)** Axial intensity distributions and **(c)** Bar plot of normalized area under the curve for lens, hybrid states, and axicon, respectively. (Adapted from **Publication II**)

4.2.1.2 INCHIS-H2

INCHIS-H2, as described in Section 3.2.2, is a purely post-processing approach in which two independently recorded images or videos, one obtained using a lens and the other using an axicon, are combined after recording by applying appropriate weights using the variables T_1 and T_2, by which hybrid OIDs with intermediate axial characteristics can be produced. The hybrid PSFs obtained with identical conditions are used to reconstruct images/videos with a desired AR. The 3D simulation results of INCHIS-H2 are shown in **Figure 31**. The I_{PSF} ($z_s = 30$ cm), $I_{PSF}(z_s = 27$ cm), I_{OID} and their reconstruction results at the two axial locations I_R (z_s = 30 cm) and I_R (z_s = 27 cm) using LRRA for (T_1 = 1, T_2 = 0), (T_1 = 0.75, T_2 = 0.25), (T_1 = 0.5, T_2 = 0.5), (T_1 = 0.25, T_2 = 0.75) and (T_1 = 0, T_2 = 1) are shown in rows 1–5 respectively in **Figure 31(a)**. Comparing the reconstruction results for different cases, as in INCHIS-H1, it is observed that as T_1 and T_2 are tuned to transform the lens into an axicon through hybrid states, the

AR decreases. For $I_R(z_s = 30\text{ cm})$, it is observed that O2 is defocused with a pure lens, but the focus improves as the system is shifted towards a pure axicon. The same can be observed for $I_R(z_s = 27\text{ cm})$, where the object O1 appears defocused with a pure lens, and gradually improves as the system is shifted towards a pure axicon. The optimal values of reconstruction using LRRA, for the above cases, were $\alpha = 0$, $0.6 \leq \beta \leq 0.7$, and $4 \leq n \leq 10$. Axial intensity distributions were again calculated by correlating the $I_{PSF}(z_s = 30\text{ cm})$ with $I_{PSF}(20\text{ cm} \leq z_s \leq 30\text{ cm})$ in steps of 1 mm using the NLR with parameters $\alpha = 0$ and $\beta = 1$. The resulting axial profiles for the five cases are plotted and shown in **Figure 31(b)**. As observed in the plot, the gradual increase in focal depth with increasing T_2 and decreasing T_1 is as expected. The normalized areas under the axial curves for different T_1 and T_2 combinations are plotted as a bar chart, as shown in **Figure 31(c)**. The plot quantitatively shows the difference in AR for different combinations of T_1 and T_2, with a maximum AR for a lens ($T_1 = 1$, $T_2 = 0$) and a minimum AR for an axicon ($T_1 = 0$, $T_2 = 1$).

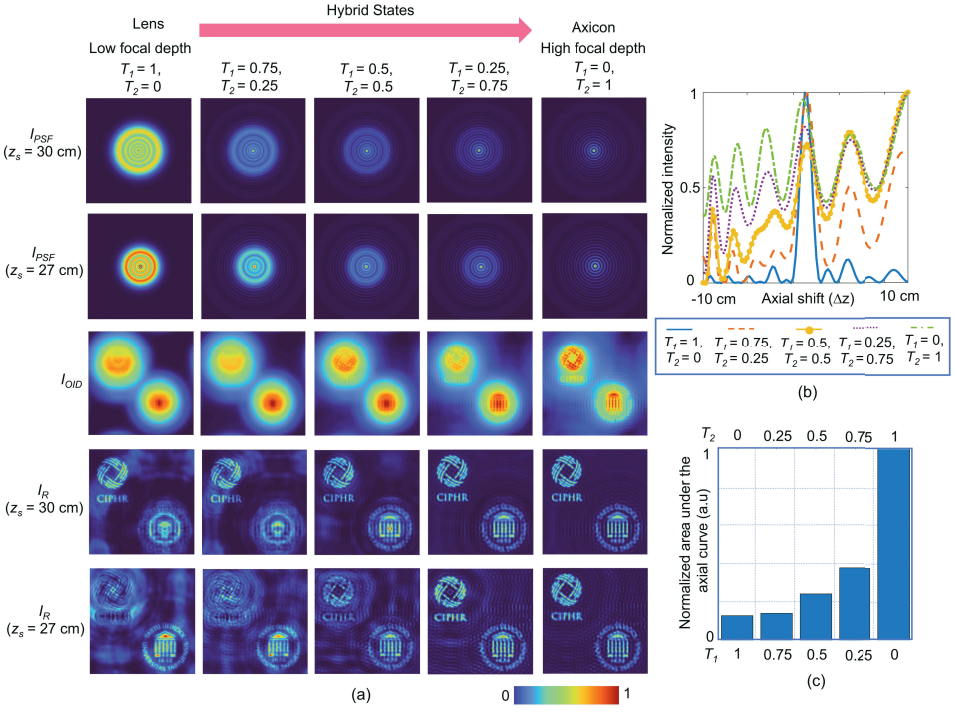

Figure 31. INCHIS-H2: (a) Row 1 – $I_{PSF}(z_s = 30\text{ cm})$, Row 2 – $I_{PSF}(z_s = 27\text{ cm})$, Row 3 – I_{OID}, and Row 4 and Row 5 reconstruction results by LRRA at the two axial locations $I_R(z_s = 30\text{ cm})$ and $I_R(z_s = 27\text{ cm})$, shown for lens, hybrid states, and axicon, respectively. **(b)** Axial intensity distributions and **(c)** Bar plot of normalized area under the curve for lens, hybrid states, and axicon, respectively. (Adapted from **Publication II**)

4.2.2 Experimental studies

The photograph of the experimental setup used for demonstrating the concept of INCHIS-H1 is shown in **Figure 32**. The setup includes the following optical components from Thorlabs: Element 1 – M660L4 LED with 940 mW power, operating at a wavelength of λ = 660 nm, and a bandwidth of $\Delta\lambda$ = 20 nm; Element 2 – ID50/M standard iris, Ø50.0 mm max aperture; Element 3 – N-BK7 Ø1" biconvex refractive lens with a focal length (f = 5 cm); Element 4 – Ø1" pinhole (50 µm) or test objects digit '1' and '3' from group 5 in R1DS1N Negative USAF test target; Element 5 – ID20/M standard iris, Ø20.0 mm max aperture; Element 6 – N-BK7 Ø1" biconvex refractive lens with a focal length (f = 5 cm); Element 7 – Ø1" linear polarizer with N-BK7 windows; Element 8 – BS013 50:50 non-polarizing beam splitter cube; Element 9 – Exulus HD2 SLM with 1920 × 1200 pixels and having a pixel size of 8 µm and Element 10 – Zelux CS165MU/M monochrome image sensor with 1440 × 1080 pixels and having a pixel size of ~3.5 µm.

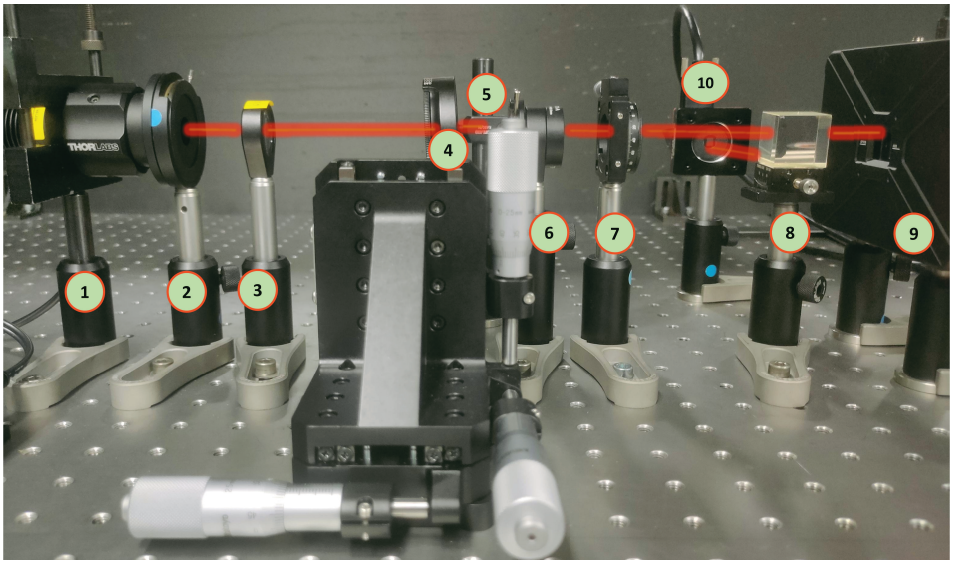

Figure 32. Photograph of the experimental setup used for demonstration. (1) LED, (2) iris, (3) refractive lens (f = 5 cm), (4) object/pinhole, (5) iris, (6) refractive lens (f = 5 cm), (7) polarizer, (8) beam splitter, (9) SLM, and (10) image sensor. The beam path from the LED to the image sensor is indicated in red. (Adapted from **Publication II**)

The LED light critically illuminated the object through a biconvex refractive lens. An iris placed after the LED controlled the illumination diameter. Two objects were used for the experiments: the digits '3' and '1'. The object digits '3' and '1' were placed at the axial locations z_s = 5 cm and z_s = 5.6 cm, respectively. The light from the object was collected by a biconvex refractive lens. An iris was used together with this lens to control the system's effective NA. The collimated light from the object was passed through a polarizer aligned with the active axis of the

SLM, then propagated to a beam splitter and then to the SLM. On the SLM, the CPMs shown in column 1 of **Figure 33** were displayed one after the other sequentially, and the corresponding OIDs were recorded by the image sensor. The entire process is repeated by replacing the object with a 50 μm pinhole, and the PSFs were recorded at the same two axial locations. The imaging distance from the SLM to the image sensor was z_h = 17.8 cm. The hybrid CPMs were engineered with a DoF < ~10% using TAP-GSA. The CPMs shown in column 1 of **Figures 33(a) and 35(a)** were designed in MATLAB [99] based on the SLM specifications (operating wavelength range 400–850 nm, pixel size 8 μm, and panel resolution 1920 × 1200). The designed phase masks were exported as bitmap images compatible with the SLM controller. The SLM was connected directly to the computer and operated using the Thorlabs control software, which allows bitmap phase masks to be loaded and displayed without additional pre-processing. During recording, the phase masks were displayed sequentially. After each mask was displayed on the SLM, a short stabilization period of 2–3 seconds was allowed before capturing the corresponding intensity distribution with the image sensor. This ensured stable SLM rendering and consistent formation of the intensity distribution. The experimentally recorded data were subsequently processed in MATLAB [99], where the computational reconstruction was performed, and the figures were generated, as shown in the upcoming Sections 4.2.2.1, 4.2.2.2, 4.2.3, and 4.2.4.

4.2.2.1 INCHIS-H1

The 3D experimental results of INCHIS-H1 are shown in **Figure 33**. The CPMs, $I_{PSF}(z_s = 5\text{ cm})$, $I_{PSF}(z_s = 5.6\text{ cm})$, I_{OID} and their reconstruction results at the two axial locations $I_R(z_s = 5\text{ cm})$ and $I_R(z_s = 5.6\text{ cm})$ using LRRA for ($T_1 = 0$, $T_2 = 1$), ($T_1 = 0.25$, $T_2 = 0.75$), ($T_1 = 0.5$, $T_2 = 0.5$), ($T_1 = 0.75$, $T_2 = 0.25$) and ($T_1 = 1$, $T_2 = 0$) are shown in columns 1–6 respectively of **Figure 33(a)**. The direct image of the test objects digits '1' and '3' when they were located at the same axial location is shown in **Figure 33(b)**. Comparing the reconstruction results for the different cases, it is seen that as the values of T_1 and T_2 were tuned to transform the axicon into a lens through hybrid states, the AR increased. For $I_R(z_s = 5\text{ cm})$, it is seen that the object digit '1' is focused in the case of a pure axicon, but the focus reduces as the system is shifted towards a pure lens. The same can be observed for $I_R(z_s = 5.6\text{ cm})$, where the object digit '3' appears focused in the case of a pure axicon, and the blur gradually increases as the system is shifted towards a pure lens. This confirms that INCHIS-H1 demonstrates variation in AR without affecting LR. To quantitatively show the variation of AR for different cases of (T_1, T_2), namely (1,0), (0.75,0.25), (0.5,0.5), (0.25,0.75), and (0,1), the normalized ratio between the average intensity values at the two axial locations given as $S = \frac{\mu_{I_R}(O_1)}{\mu_{I_R}(O_2)}$, where O_1 is the object that is out of focus and O_2 is the object that is in focus during reconstruction, is plotted as bar plot using MATLAB [99] and it is shown in **Figure 33(c)**. As observed from the plot, the value of S

increases as the system transitions from a lens ($T_1 = 1$, $T_2 = 0$), with high AR, to an axicon ($T_1 = 0$, $T_2 = 1$), with low AR, while intermediate (T_1, T_2) values yield mixed axial characteristics.

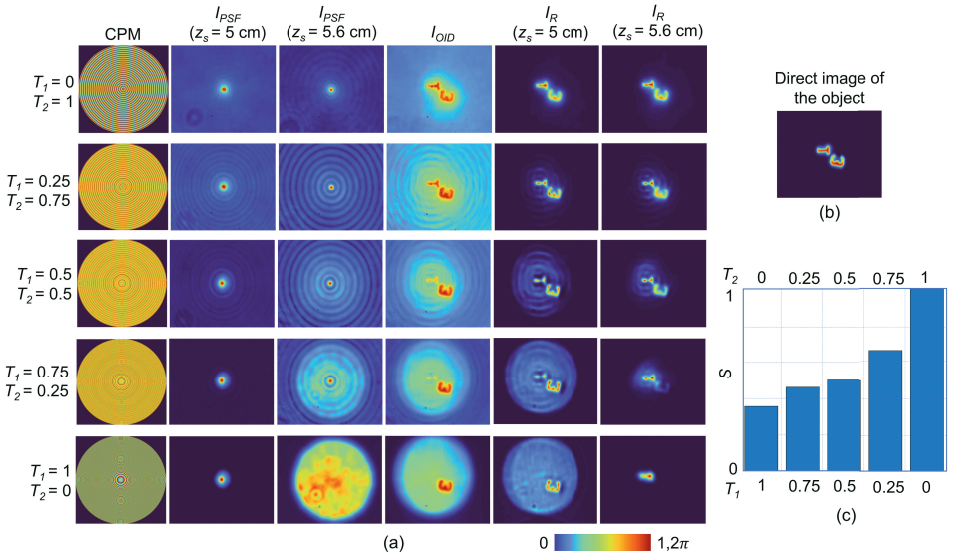

Figure 33. INCHIS-H1: (a) Column 1 – CPM, Column 2 – I_{PSF} (z_s = 5 cm), Column 3 – I_{PSF} (z_s = 5.6 cm), Column 4 – I_{OID}, and Column 5 and Column 6 reconstruction results by LRRA at the two axial locations I_R (z_s = 5 cm) and I_R (z_s = 5.6 cm), shown for axicon, hybrid states and lens respectively. **(b)** Direct image of the test objects when located at the same axial location **(c)** Normalized ratio S for lens, hybrid states, and axicon, respectively. (Adapted from **Publication II**)

4.2.2.2 INCHIS-H2

In INCHIS-H2, the PSFs and OIDs recorded independently with a lens and an axicon were combined computationally with different weights using T_1 and T_2 to generate the hybrid cases. In the first step, the PSF of a particular axial location (z_s = 5 cm) of the lens and axicon were taken, and the weights T_1 = 0.25 and T_2 = 0.75 were applied and summed to obtain the hybrid PSF for the second case (T_1 = 0.25, T_2 = 0.75). Similarly, the OID of axicon and lens were taken, and the weights T_1 = 0.25 and T_2 = 0.75 were applied and summed to obtain the OID for the second case (T_1 = 0.25, T_2 = 0.75). This process was repeated by applying different weights to PSF and OID for the other cases. The 3D experimental results of INCHIS-H2 are shown in **Figure 34**. The I_{PSF} (z_s = 5 cm), I_{PSF} (z_s = 5.6 cm), I_{OID} and their reconstruction results at the two axial locations I_R (z_s = 5 cm) and I_R (z_s = 5.6 cm) using LRRA for (T_1 = 0, T_2 = 1), (T_1 = 0.25, T_2 = 0.75), (T_1 = 0.5, T_2 = 0.5), (T_1 = 0.75, T_2 = 0.25) and (T_1 = 1, T_2 = 0) are shown in columns 1–5 of **Figure 34(a)** respectively. Comparing the reconstruction results across the different cases, it is observed that as the values of T_1 and T_2 are tuned to transform the axicon into a lens through hybrid states, the AR increased similarly to

INCHIS-H1. For $I_R(z_s = 5\text{ cm})$, it is seen that the object digit '1' is focused in the case of a pure axicon, but the focus reduces as the system is shifted towards a pure lens. The same can be observed for $I_R(z_s = 5.6\text{ cm})$, where the object digit '3' appears focused in the case of a pure axicon, and the blur gradually increases as the system is shifted towards a pure lens. This confirms that INCHIS-H2 demonstrates variation in AR without affecting LR. To quantitatively show the variation of AR for different cases of (T_1, T_2), namely (1,0), (0.75,0.25), (0.5,0.5), (0.25,0.75), and (0,1), the normalized ratio S between the average intensity values at the two axial locations, is plotted as bar plot using MATLAB [99] and it is shown in **Figure 34(b)**. As observed from the plot, the value of S increases as the system transitions from a lens ($T_1 = 1$, $T_2 = 0$), with high AR, to an axicon ($T_1 = 0$, $T_2 = 1$), with a low AR, while intermediate (T_1, T_2) values yield mixed axial characteristics. In the experimental studies of INCHIS-H1 and INCHIS-H2, LRRA was operated with $0.3 \leq \alpha \leq 0.6$, $\beta = 1$ and $25 \leq n \leq 35$.

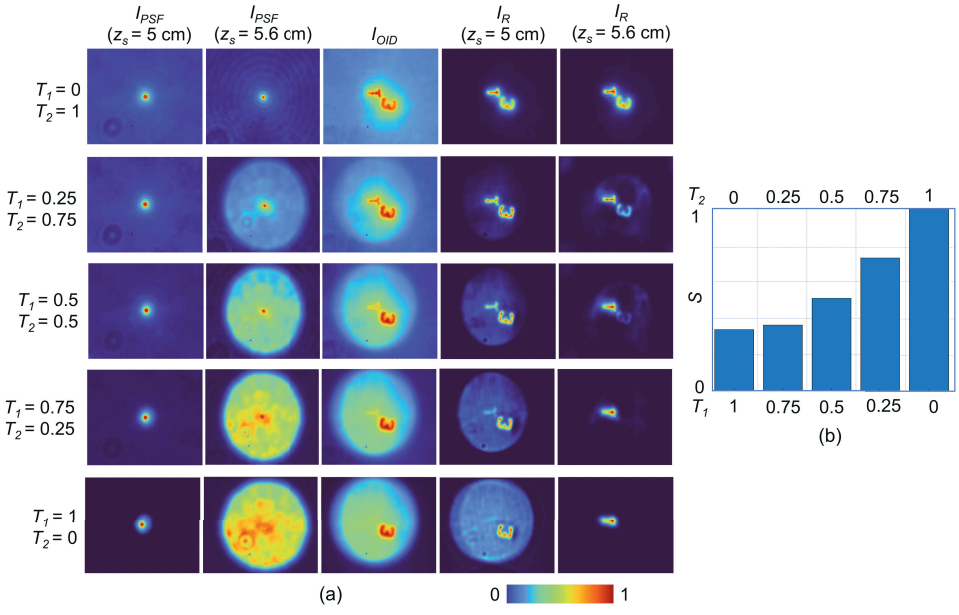

Figure 34. INCHIS-H2: (a) Column 1 – $I_{PSF}(z_s = 5\text{ cm})$, Column 2 – $I_{PSF}(z_s = 5.6\text{ cm})$, Column 3 – I_{OID}, and Column 4 and Column 5 reconstruction results by LRRA at the two axial locations $I_R(z_s = 5\text{ cm})$ and $I_R(z_s = 5.6\text{ cm})$, shown for axicon, hybrid states, and lens, respectively. **(b)** Normalized ratio S for lens, hybrid states, and axicon, respectively. (Adapted from **Publication II**)

4.2.3 Additional experimental studies with synthetic dot-pattern objects

The additional experiments with synthetic dot-pattern objects were conducted using the same experimental setup shown in **Figure 32** to further verify the capabilities of INCHIS-H1 and INCHIS-H2. Synthetic dot-pattern objects corresponding to the letters 'Z' and 'N' were used. These objects were generated by laterally shifting a 10 µm pinhole in 20 µm steps along both the horizontal and vertical directions, resulting in 50 discrete point locations. The object letters 'Z' and 'N' are placed at the axial locations $z_s = 5$ cm and $z_s = 5.15$ cm, respectively. For this particular study, binary CPMs were designed for the following cases of T_1 and T_2: (T_1, T_2) = (0, 1), (0.25, 0.75), (0.5, 0.5), (0.75, 0.25), (0.875, 0.125), (1, 0), as shown in column 1 of **Figure 35(a)**.

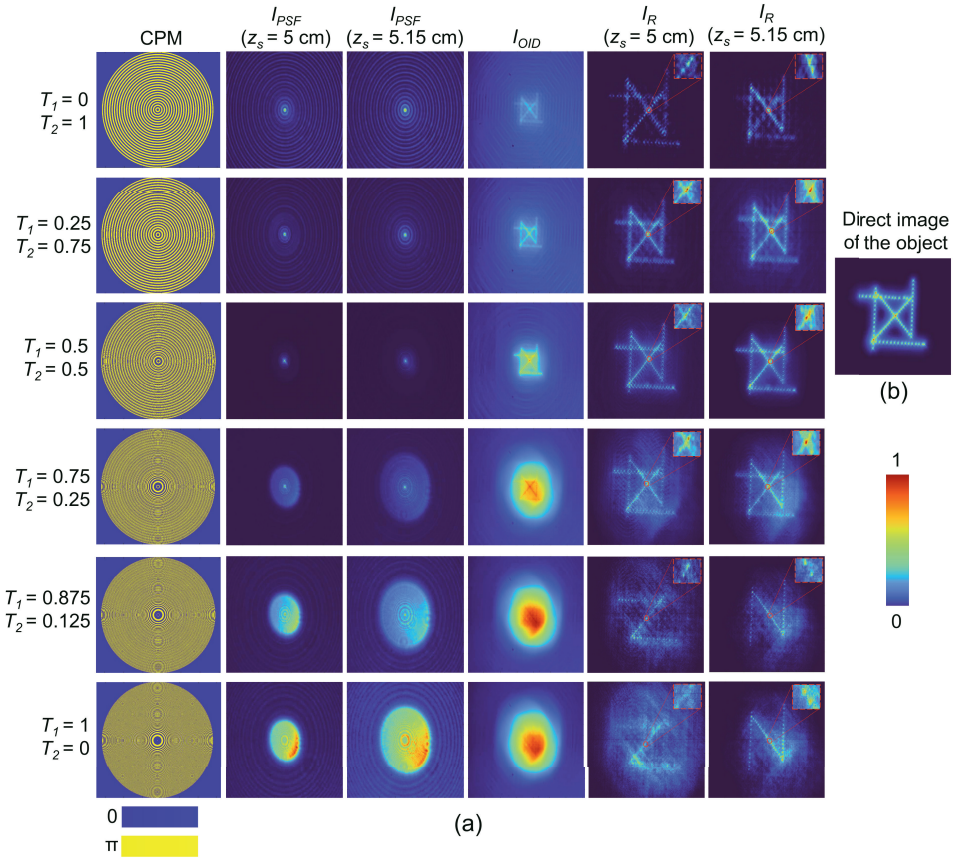

Figure 35. INCHIS-H1: (a) Column 1 – Binary CPM, Column 2 – I_{PSF} (z_s = 5 cm), Column 3 – I_{PSF} (z_s = 5.15 cm), Column 4 – I_{OID}, and Column 5 and Column 6 reconstruction results by LRRA at the two axial locations I_R (z_s = 5 cm) and I_R (z_s = 5.15 cm), shown for axicon, hybrid states and lens respectively. **(b)** Direct image of the synthetic objects letters 'Z' and 'N' when located at the same axial location. (Adapted from **Publication II**)

These binary CPMs were designed using TAP-GSA with DoF < ~10%. The 3D experimental results of INCHIS-H1 with synthetic objects are shown in **Figure 35**. The binary CPMs, I_{PSF} (z_s = 5 cm), I_{PSF} (z_s = 5.15 cm), I_{OID} and their reconstruction results at the two axial locations I_R (z_s = 5 cm) and I_R (z_s = 5.15 cm) using LRRA for (T_1 = 0, T_2 = 1), (T_1 = 0.25, T_2 = 0.75), (T_1 = 0.5, T_2 = 0.5), (T_1 = 0.75, T_2 = 0.25), (T_1 = 0.875, T_2 = 0.125) and (T_1 = 1, T_2 = 0) are shown in columns 1–6 respectively of **Figure 35(a)**. The direct images of both synthetic objects, the letters 'Z' and 'N', when located at the same axial location, are shown in **Figure 35(b)**. Comparing the reconstruction results for the different cases, it is seen that as the values of T_1 and T_2 are tuned to transform the axicon into a lens through hybrid states, the AR increased. For I_R (z_s = 5 cm), it is seen that the synthetic object letter 'N' is focused in the case of a pure axicon, but the focus reduces as the system is shifted towards a pure lens. The same can be observed for I_R (z_s = 5.15 cm), where the synthetic object letter 'Z' appears focused in the case of a pure axicon, and the blur gradually increases as the system is shifted towards a pure lens. This again confirms the variation in AR without affecting LR, as observed with INCHIS-H1.

In INCHIS-H2, the PSFs and OIDs, recorded independently with a lens and an axicon, were combined computationally after applying different weights, T_1 and T_2, to generate the hybrid cases. In the first step, the PSF of a particular axial location (z_s = 5 cm) of the lens and axicon were taken, and the weights T_1 = 0.25 and T_2 = 0.75 were applied and summed to obtain the hybrid PSF for the second case (T_1 = 0.25, T_2 = 0.75). Similarly, the OID of axicon and lens were taken, and the weights T_1 = 0.25 and T_2 = 0.75 were applied and summed to obtain the OID for the second case (T_1 = 0.25, T_2 = 0.75). This process was repeated by applying different weights to PSF and OID for the other cases. The 3D experimental results of INCHIS-H2 with synthetic objects are shown in **Figure 36**.

The I_{PSF} (z_s = 5 cm), I_{PSF} (z_s = 5.15 cm), I_{OID} and their reconstruction results at the two axial locations I_R (z_s = 5 cm) and I_R (z_s = 5.15 cm) using LRRA for (T_1 = 0, T_2 = 1), (T_1 = 0.25, T_2 = 0.75), (T_1 = 0.5, T_2 = 0.5), (T_1 = 0.75, T_2 = 0.25), (T_1 = 0.875, T_2 = 0.125) and (T_1 = 1, T_2 = 0) are shown in columns 1–5 respectively. Comparing the reconstruction results for the different cases, it is seen that as the values of T_1 and T_2 were tuned to transform the axicon into a lens through hybrid states, the AR increased similarly to that of INCHIS-H1. For I_R (z_s = 5 cm), it is seen that the synthetic object letter 'N' is focused in the case of a pure axicon, but the focus reduces as the system is shifted towards a pure lens. The same can be observed for I_R (z_s = 5.15 cm), where the synthetic object letter 'Z' appears focused in the case of a pure axicon, and the blur gradually increases as the system is shifted towards a pure lens. This again confirms the variation in AR without affecting LR by INCHIS-H2. In the experimental studies with synthetic test objects, LRRA was operated with $\alpha = 0$, $0.8 \leq \beta \leq 1$ and $4 \leq n \leq 6$.

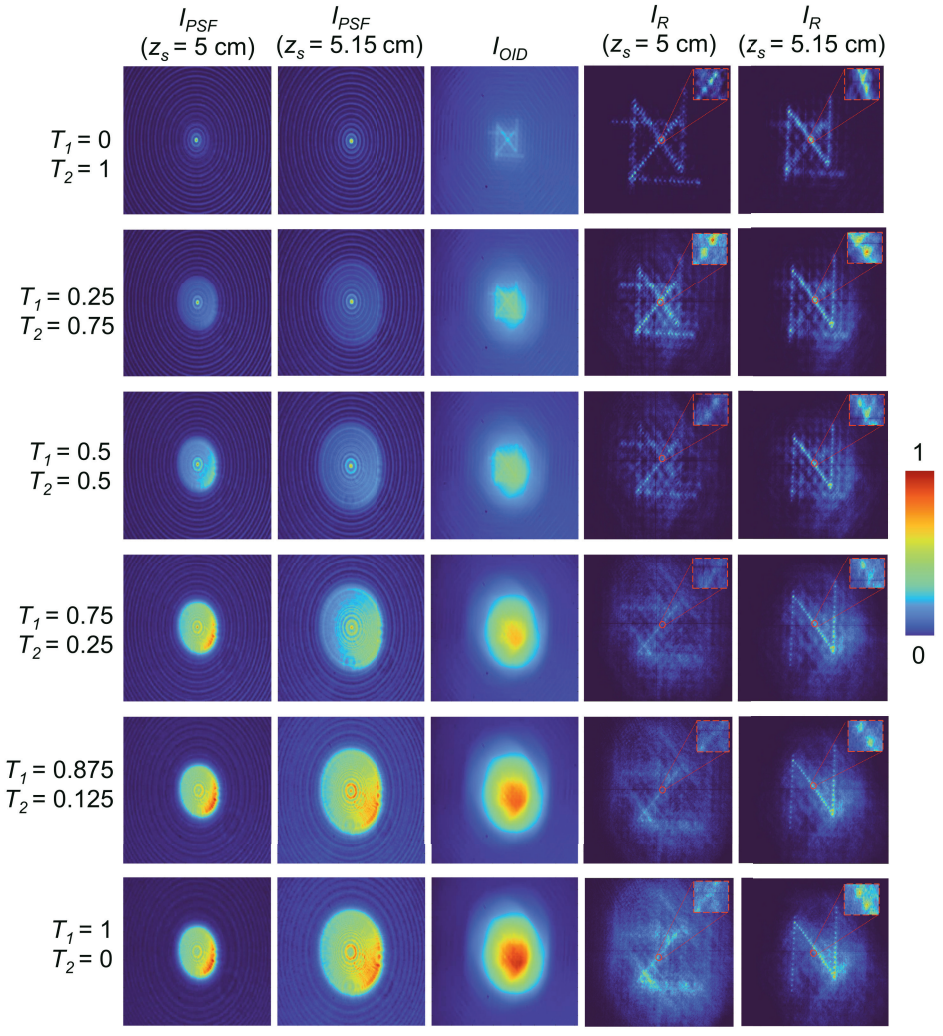

Figure 36. INCHIS-H2: (a) Column 1 – I_{PSF} (z_s = 5 cm), Column 2 – I_{PSF} (z_s = 5.15 cm), Column 3 – I_{OID}, and Column 4 and Column 5 reconstruction results by LRRA at the two axial locations I_R (z_s = 5 cm) and I_R (z_s = 5.15 cm), shown for axicon, hybrid states, and lens, respectively. (Adapted from **Publication II**)

4.2.4 Demonstration of INCHIS-H2 using passive refractive optical elements

The photograph of the INCHIS-H2 experimental setup used for demonstrating the concept of INCHIS-H2 is shown in **Figure 37**. The setup includes the following optical components from Thorlabs:Element 1 – M660L4 LED with 940 mW power, operating at a wavelength of λ = 660 nm, and a bandwidth of Δλ = 20 nm; Element 2 – LED power controller; Element 3 – N-BK7 Ø1" biconvex refractive lens with a focal length (f = 5 cm); Element 4 – Ø1" pinhole (50 µm);

Element 5 – N-BK7 Ø1" biconvex refractive lens with a focal length (f = 10 cm); Element 6 – BS031 50:50 non-polarizing beam splitter cube; Element 7 – N-BK7 Ø1" biconvex refractive lens with a focal length (f = 10 cm); Element 8 – Zelux CS165MU/M monochrome image sensor 1 with 1440 × 1080 pixels and having a pixel size of ~3.5 µm; Element 9 – Ø1" refractive axicon (base angle –2.5 degrees, thickness – 1 cm) and Element 10 – Zelux CS165MU/M monochrome image sensor 2 with 1440 × 1080 pixels and having a pixel size of ~3.5 µm.

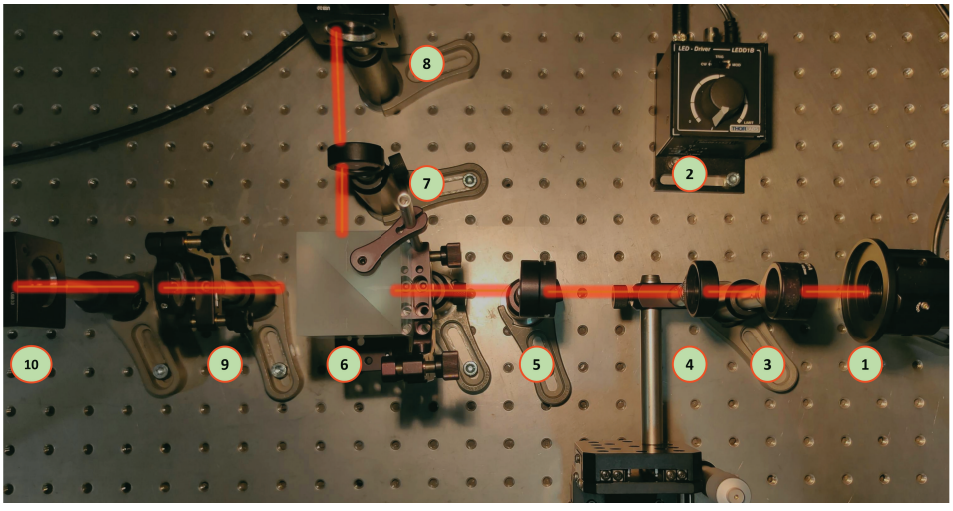

Figure 37. Photograph of the experimental setup of INCHIS-H2 using passive refractive optical elements – lens and axicon. (1) LED, (2) LED power controller, (3) refractive lens (f = 5 cm), (4) object/pinhole, (5) refractive lens (f = 10 cm), (6) beam splitter, (7) refractive lens (f = 10 cm), (8) image sensor 1, (9) refractive axicon and (10) image sensor 2. The beam path from the LED to the image sensors is indicated in red. (Adapted from **Publication II**)

The LED light critically illuminated the object through a biconvex refractive lens. The 50 µm pinhole is used to record the PSF. A synthetic two-point object is generated by shifting the same 50 µm pinhole left and right from the center in the horizontal direction, which is considered as object 1, and it is placed at the axial location z_s = 10 cm. Another two-point object is generated by shifting the 50 µm pinhole again up and down from the center in the vertical direction, which is considered as object 2, and it is placed at the axial location z_s = 11.7 cm. The light from the pinhole/object was collected by another biconvex refractive lens. The collimated light from the pinhole/object is propagated to a beam splitter. The beam splitter divides the beam into two. The first beam from the beam splitter was incident on the refractive lens, and the second beam from the beam splitter was incident on the refractive axicon. Initially, the PSFs and OIDs for object 1 at the axial location z_s = 10 cm, corresponding to the refractive lens (Element 7) and the refractive axicon (Element 9), are recorded collinearly by two image sensors (Elements 8 and 10), respectively. Then again, the PSFs and OIDs corresponding

to object 2, placed at the axial location $z_s = 11.7$ cm corresponding to the refractive lens (Element 7) and the refractive axicon (Element 9), are recorded collinearly by two image sensors (Elements 8 and 10) respectively. The two image sensors (elements 8 and 10) were placed 15 cm from the beam splitter (Element 6). The hybrid PSFs and OIDs were generated by applying different weight combinations as ($T_1 = 0.25$; $T_2 = 0.75$), ($T_1 = 0.5$; $T_2 = 0.5$), ($T_1 = 0.75$; $T_2 = 0.25$), and ($T_1 = 0.875$; $T_2 = 0.125$) to the recorded PSFs and OIDs corresponding to the lens and axicon.

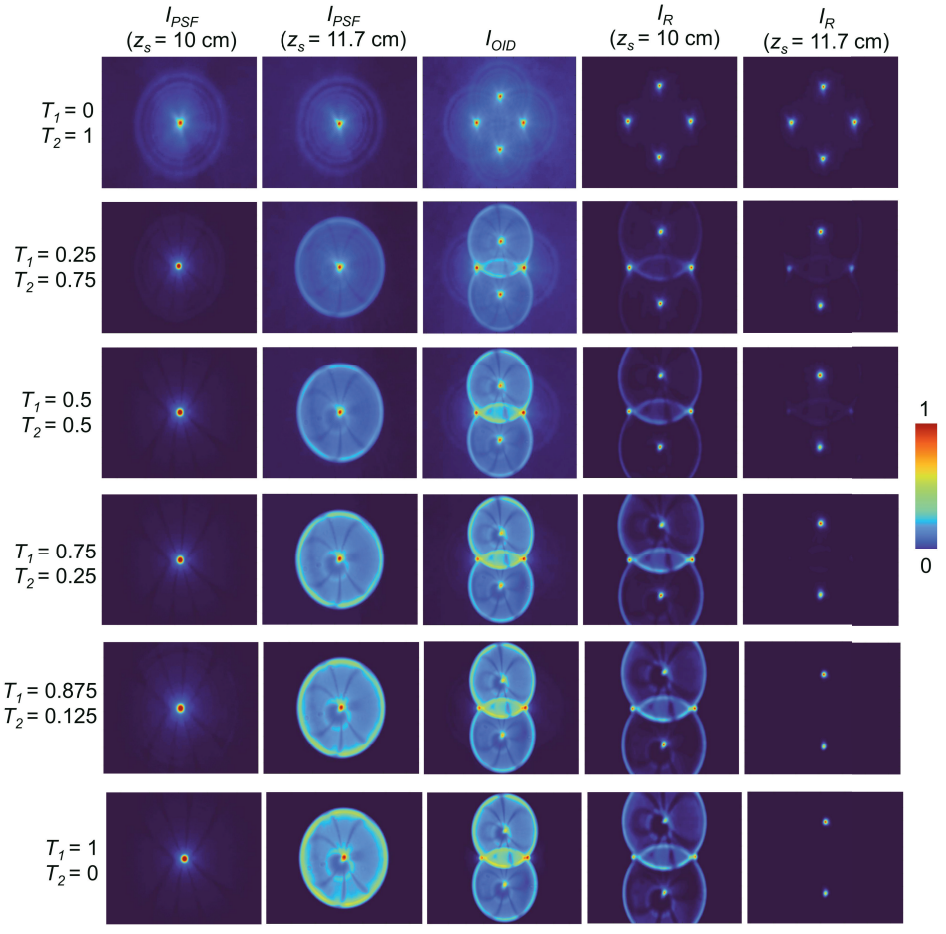

Figure 38. INCHIS-H2: Column 1 – I_{PSF} (z_s = 10 cm), Column 2 – I_{PSF} (z_s = 11.7 cm), Column 3 – I_{OID}, and Column 4 and Column 5 reconstruction results by LRRA at the two axial locations I_R (z_s = 10 cm) and I_R (z_s = 11.7 cm), shown for axicon, hybrid states, and lens, respectively. (Adapted from **Publication II**)

The 3D experimental results of INCHIS-H2 using passive refractive optical elements – lens and axicon are shown in **Figure 38**. The $I_{PSF}(z_s = 10\text{ cm})$, $I_{PS}(z_s = 11.7\text{ cm})$, I_{OID} and their reconstruction results at the two axial locations $I_R(z_s = 10\text{ cm})$ and $I_R(z_s = 11.7\text{ cm})$ using LRRA for ($T_1 = 0$, $T_2 = 1$), ($T_1 = 0.25$, $T_2 = 0.75$), ($T_1 = 0.5$, $T_2 = 0.5$), ($T_1 = 0.75$, $T_2 = 0.25$), ($T_1 = 0.875$, $T_2 = 0.125$) and ($T_1 = 1$, $T_2 = 0$) are shown in columns 1–5 respectively. Comparing the reconstruction results across the different cases, it is observed that as the values of T_1 and T_2 are tuned to transform the axicon into a lens through hybrid states, the AR increases similarly to that observed in previous INCHIS-H1 and INCHIS-H2 studies. For $I_R(z_s = 10\text{ cm})$, it is seen that the 'object 2' is focused in the case of a pure axicon, but the focus reduces as the system is shifted towards a pure lens. The same can be observed for $I_R(z_s = 11.7\text{ cm})$, where the 'object 1' appears focused in the case of a pure axicon, and the blur gradually increases as the system is shifted towards a pure lens. This again confirms the variation in AR without affecting LR when using INCHIS-H2 with passive optical elements. In the experimental studies with passive optical elements, LRRA was operated with $0.2 \leq \alpha \leq 0.5$, $\beta = 1$, and $3 \leq n \leq 10$.

4.2.5 Discussion

Two hybrid imaging methods, namely INCHIS-H1 and INCHIS-H2, were developed to address the long-standing challenge of tuning AR independently of LR in incoherent imaging systems. INCHIS-H1 was inspired by [75] but is more advanced than [75] in all aspects of imaging and implementation. The method proposed in [75] was based on FINCH and COACH, and so it was necessary to convert every object point into at least three beams: spherical, plane, and chaotic, and at least three camera shots were required. In the proposed INCHIS-H1, every object point is converted into two beams: spherical and Bessel, and a single camera shot is sufficient. In a way, the INCHIS-H1 can be considered FINCH or IDH, where self-interference occurs between a Bessel beam and a spherical beam instead of between two spherical beams. By tuning the ratios T_1 and T_2, INCHIS-H1 can be tuned from I-COACH or CAI with a lens as a coded aperture to I-COACH or CAI with an axicon as a coded aperture through FINCH. Further, the SNR of the INCHIS-H1 is higher than that reported in [75]. The above is partially due to the nature of the self-interfering beams: in INCHIS-H1, the intensity distributions have higher energy density due to deterministic optical fields, compared to a scattered beam in COACH. The second reason for a better SNR in INCHIS-H1 compared to COACH is the lower photon budget requirement due to a smaller number of beams in INCHIS-H1 than in COACH. Finally, TAP-GSA is used in INCHIS-H1 for multiplexing CPMs instead of RM. Finally, in [75], when the AR is tuned, the LR is also changed, unlike in both INCHIS methods. In all the hybrid cases, the DoF of TAP-GSA was maintained low to avoid any loss of light due to scattering.

4.2.5.1 Comparison of INCHIS-H1 with existing methods

A broader comparison with existing AR-tunable methods further highlights the advantages of INCHIS-H1. Precursors to INCHIS-H1 include the FINCH-COACH system [75] and recent I-COACH implementations employing Bessel, Airy, and self-rotating beams, where it is possible to tune AR [58, 77, 78].

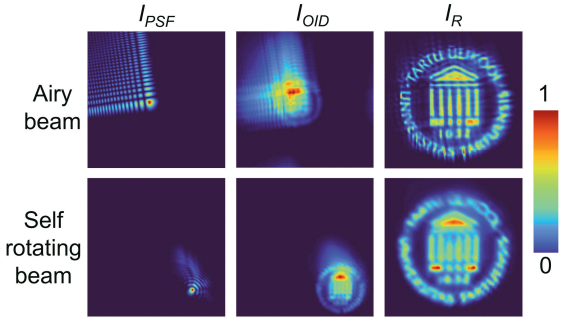

Figure 39. Column 1 – I_{PSF}, Column 2 – I_{OID}, and Column 3 – I_R by LRRA, shown for Airy beam and self-rotating beam, respectively. (Adapted from **Publication II**)

The FINCH-COACH system requires multiple beams and multiple camera shots, and additionally suffers from LR variation when AR is tuned [75]. On the other hand, I-COACH systems based on Airy and self-rotating beams exhibit improper object sampling, resulting in non-optimal reconstructions when high focal depths are required [58, 77, 78]. The simulated PSFs, OIDs, and reconstruction results for a single Airy beam and a self-rotating beam using a test object logo of 'University of Tartu' are shown in **Figure 39**. The results show that the object is improperly sampled by Airy and self-rotating beams, resulting in distorted reconstructions. Therefore, the above solutions are not optimal for the extreme case of maximum focal depth. Again, when the number of beams is increased, a higher photon budget is needed as in [75]. The performances of the FINCH-COACH system, I-COACH with Bessel, Airy, and self-rotating beams, and INCHIS-H1 are compared in **Table 3** on the following categories: number of beams required for tuning AR, number of camera shots, LR dependency on AR, and sampling problems. The number of beams required is inversely related to the SNR: as the number of beams increases, energy is distributed, causing the intensity levels to reach the detector's noise level when recording PSFs. From **Table 3**, it is clear that INCHIS-H1 is better than existing methods. There are no reported cases of tuning AR after recording, so it is not possible to compare INCHIS-H2 with existing methods.

Table 3. Comparison of the performance of COACH-FINCH, I-COACH, with Bessel, Airy, self-rotating beams, and INCHIS-H1. (Adapted from **Publication II**)

No.	Indirect imaging system (IIS)	Optical beams needed for tuning AR	Number of camera shots	LR dependency of AR	Sampling problems
1	COACH-FINCH system	Three beams: spherical, scattered, and plane beam	3	Changes with ARP	No
2	I-COACH with an ensemble of Bessel beams	One to four beams	1	Constant	No
3	I-COACH with an ensemble of Airy beams	One to four beams	1	Constant	Yes (Single beam)
4	I-COACH with an ensemble of self-rotating beams	One to four beams	1	Constant	Yes (Single beam)
5	INCHIS-H1	One to two beams	1	Constant	No

4.2.5.2 Anomalous axial regions

Ideally, as the CPM is tuned from a pure lens ($T_1 = 1$, $T_2 = 0$) to a pure axicon ($T_1 = 0$, $T_2 = 1$), the focal depth is expected to improve, resulting in a systematic reduction of AR. While this trend is observed on average, certain anomalous axial regions appear in INCHIS-H1 where the trend does not follow, as seen from the axial response plots in **Figure 30(b)**. In these regions, a CPM with a higher lens contribution yields better reconstruction quality than one with a higher axicon contribution than lens when reconstructed using an I_{PSF} recorded at a different plane. These anomalous axial regions are more prominent when binary CPMs are used, primarily due to the presence of higher diffraction orders as seen from the results of **Figure 35(a)**. This effect is also illustrated in **Figure 40**, where the axial profiles for different combinations ($T_1 = 1$, $T_2 = 0$), ($T_1 = 0.75$, $T_2 = 0.25$), ($T_1 = 0.5$, $T_2 = 0.5$), ($T_1 = 0.25$, $T_2 = 0.75$) and ($T_1 = 0$, $T_2 = 1$) are plotted using MATLAB [99] for a binary phase element and the anomalous regions are highlighted. In these regions, the variation in AR for different cases does not follow the expected trend. These anomalous axial regions need to be addressed in future studies.

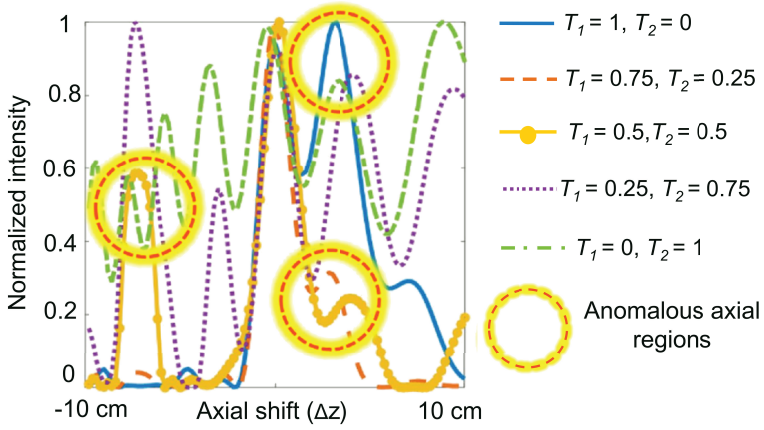

Figure 40. Axial intensity distributions for ($T_1 = 1$, $T_2 = 0$), ($T_1 = 0.75$, $T_2 = 0.25$), ($T_1 = 0.5$, $T_2 = 0.5$), ($T_1 = 0.25$, $T_2 = 0.75$) and ($T_1 = 0$, $T_2 = 1$) for a binary phase element. The anomalous axial regions are indicated by a red dotted circle with a yellow glow. (Adapted from **Publication II**)

INCHIS-H2 is more elegant and more powerful than INCHIS-H1. The post-processing of the recorded OIDs, which involves adding the intensity distributions weighted by T_1 and T_2, does not create any anomalous axial regions, as observed in simulation studies (**Figure 31(b)**). In simulation studies, the values of T_1 and T_2 used to create the hybrid I_{PSF} and I_O were identical. In the experiment, however, it was necessary to adjust T_1 and T_2 to compensate for changes in exposure time and light intensity during recording. The principal advantage of INCHIS-H2 is its ability to tune the AR of recorded images and videos after data acquisition, a capability not previously reported in the literature. As with any new method, the advantage often comes with a penalty, and INCHIS-H2 is not an exception. While this flexibility of INCHIS-H2 comes at the cost of recording two images or two videos instead of one, the penalty is modest when compared to most in-line holography methods, which typically require at least three camera shots.

4.3 PEGASASS

The results of simulation studies and optical experiments are presented in the following sections.

4.3.1 Experimental studies

The photograph of the experimental setup used for demonstrating the concept of PEGASASS is shown in **Figure 41**. The setup includes the following optical components from Thorlabs: Element 1 – M660L4 red LED with 940 mW power, operating at a wavelength of $\lambda = 660$ nm, and a bandwidth of $\Delta\lambda = 20$ nm; Element 2 – LED power controller; Element 3 – ID50/M standard iris, Ø50.0 mm

max aperture; Element 4 – Ø1” Ground Glass Diffuser (220 GRIT); Element 5 – N-BK7 Ø1" biconvex refractive lens with a focal length (f = 5 cm); Element 6 – Ø1" linear polarizer with N-BK7 windows; Element 7 – N-BK7 Ø1" biconvex refractive lens with a focal length (f = 5 cm); Element 8 – Ø1" pinhole (50 µm) or test objects digit ‘4’ and ‘1’ from group 3 in R1DS1N Negative USAF test target; Element 9 – N-BK7 Ø1" biconvex refractive lens with a focal length (f = 5 cm); Element 10 – ID20/M standard iris Ø20.0 mm max aperture; Element 11 – BS013 50:50 non-polarizing beam splitter cube; Element 12 – Exulus HD2 SLM with 1920 × 1200 pixels and having a pixel size of 8 µm; Element 13 – FLH633-5 band pass filter with a wavelength of $\lambda = 633$ nm and a bandwidth of $\Delta\lambda = 5$ nm and Element 14 – Zelux CS165MU/M monochrome image sensor with 1440 × 1080 pixels and having a pixel size of ~3.5 µm.

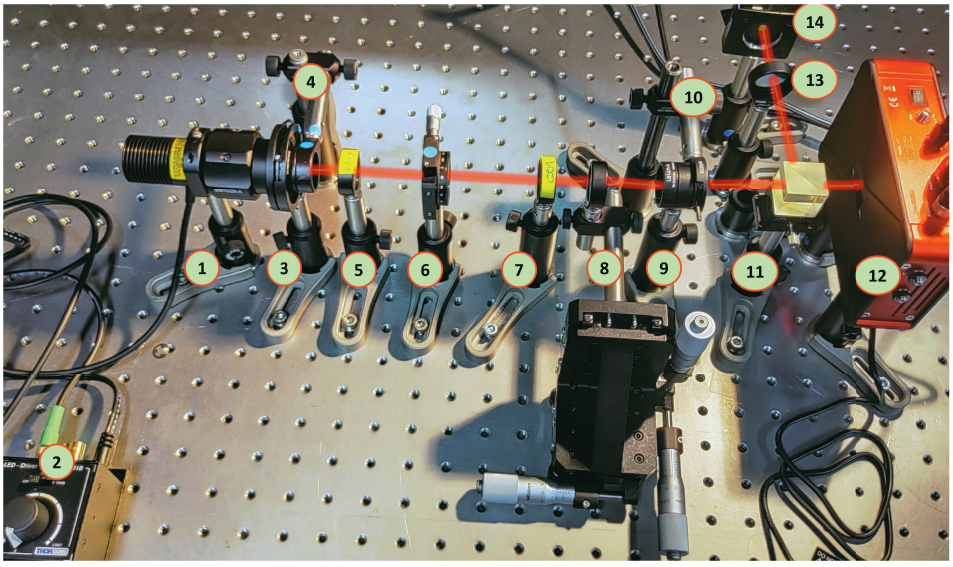

Figure 41. Photograph of the experimental setup used for demonstration. (1) LED, (2) LED power controller, (3) iris, (4) diffuser, (5) refractive lens (f = 5 cm), (6) polarizer, (7) refractive lens (f = 5 cm), (8) object/pinhole, (9) refractive lens (f = 5 cm), (10) iris, (11) beam splitter, (12) SLM, (13) bandpass filter, and (14) image sensor. The beam path from the LED to the image sensor is indicated in red. (Adapted from **Publication III**)

An iris controlled the LED’s light, which was then passed through a diffuser. This diffuser was used to remove the grating-line image and other noise from the LED light. The diffused light was collimated using another biconvex refractive lens and then passed through a polarizer aligned with the SLM’s active axis. The object was critically illuminated by a biconvex refractive lens. An iris placed after the LED controlled the illumination diameter. Two objects were used for the experiments: the digits ‘4’ and ‘1’. The object digits ‘4’ and ‘1’ were placed at the axial locations z_s = 5 cm and z_s = 5.3 cm, respectively. The light from the object was collected by a biconvex refractive lens. An iris was used together with

this lens to control the system's effective NA. The collimated light from the object was propagated to a beam splitter and then incident on the SLM. On the SLM, the four CPMs shown in **Figure 42** were displayed one after the other, and the corresponding OIDs were recorded by the image sensor. The entire process was repeated by replacing the object with a 50 μm pinhole, and the PSFs were recorded at the same two axial locations. The imaging distance from the SLM to the image sensor was z_h = 17.8 cm. A bandpass filter was used to improve the visibility of the recorded OIDs and PSFs. The CPMs shown in **Figure 42** were designed in MATLAB [99] based on the SLM specifications (operating wavelength range of 400–850 nm, pixel size of 8 μm, and panel resolution of 1920 × 1200). The designed phase masks were exported as bitmap images compatible with the SLM controller. The SLM was connected directly to the computer and operated using the Thorlabs control software, which allows bitmap phase masks to be loaded and displayed without additional pre-processing. During recording, the phase masks were displayed sequentially. After each mask was displayed on the SLM, a short stabilization period of 2–3 seconds was allowed before capturing the corresponding intensity distribution with the image sensor. This ensured stable SLM rendering and consistent formation of the intensity distribution. The experimentally recorded data were subsequently processed in MATLAB [99], where the computational reconstruction was performed, and the figures were generated, as shown in the upcoming part of this section.

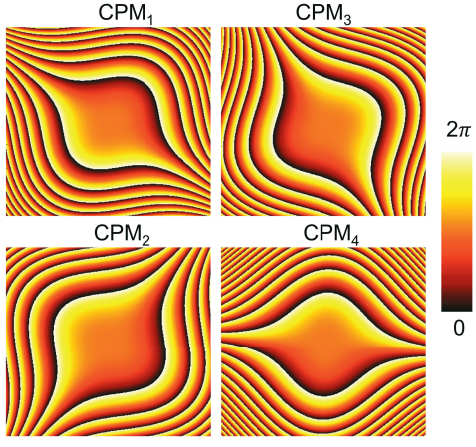

Figure 42. Images of the four CPMs used in PEGASASS. (Adapted from **Publication III**)

The experimental results of 3D imaging (x, y, z) with AR control post-recording are shown in **Figure 43(a)**. The $I_{SPSF}(z_s = 5\text{ cm})$, $I_{SPSF}(z_s = 5.3\text{ cm})$, I_{SOID}, and their reconstruction results at the two axial locations $I_R(z_s = 5\text{ cm})$ and $I_R(z_s = 5.3\text{ cm})$ using LRRA for M = 1 to 4 and γ incremented by 0.5 are shown in columns 1–5, respectively, of **Figure 43(a)**. The direct images of the test objects digits '4' and '1' when located at the same axial location is shown in **Figure 43(b)**. Comparing the reconstruction results across the different cases, it is observed that as M

increases, AR increases. When M = 1, corresponding to a single Airy beam, reconstruction using the I_{SPSF} of either axial location results in both objects ('4' and '1') appearing perfectly focused, despite their axial-separation. This behaviour indicates a low AR. When M = 2 and γ_2 = 0.5, reconstruction using I_{SPSF} corresponding to z_s = 5 cm results in a perfect reconstruction of object '4', while object '1' is slightly blurred. Conversely, reconstruction using the I_{SPSF} of z_s = 5.3 cm yields a perfect reconstruction of object '1' and object '4' exhibiting partial blur. This behaviour indicates an increase in AR. As M is increased further, the blur associated with objects located at non-matching axial locations becomes progressively stronger. This trend clearly demonstrates that increasing the number of Airy beams in the ensemble reduces the effective axial correlation length, thereby improving AR. Importantly, throughout this process, the LR remains constant, confirming that PEGASASS enables independent tuning of AR.

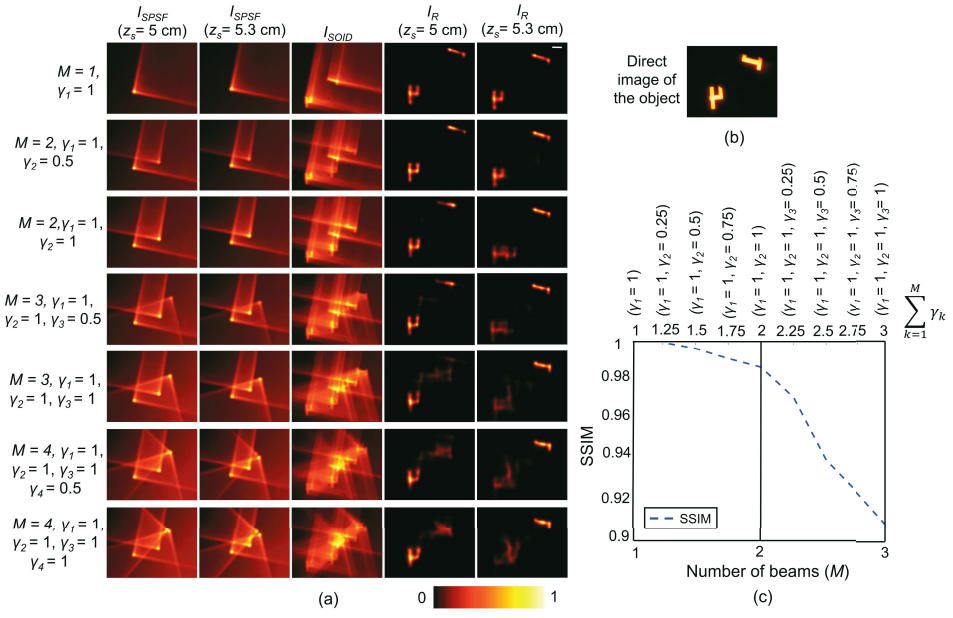

Figure 43. Experimental results of PEGASASS (AR engineering post-recording): Column 1 – I_{SPSF} (z_s = 5 cm), Column 2 – I_{SPSF} (z_s = 5.3 cm), Column 3 – I_{SOID}, and Column 4 and Column 5 reconstruction results by LRRA at the two axial locations I_R (z_s = 5 cm) and I_R (z_s = 5.3 cm), shown for M =1 to 4 and λ = 633 nm, respectively. **(b)** Direct image of objects when located at the same axial location, and **(c)** Plot of SSIM for different number of beams. Scale bar – 100 µm. (Adapted from **Publication III**)

To quantitatively assess the variation in AR, the degree of blur in the reconstructed images was evaluated using the *structural similarity index measure (SSIM)*. The SSIM was calculated using MATLAB's built-in SSIM(A, *ref*) function [99], where A represents the reconstructed image being evaluated and *ref* denotes the reference image. The SSIM values were calculated for the reconstructed images when k > 1 with respect to the reference when k = 1. The

variation of SSIM, indicating the variation of AR with respect to k, is shown in **Figure 43(c)**. As the number of beams increased, the blur increased, leading to a decrease in SSIM and an improvement in AR.

In addition to post-recording AR tuning, we have also demonstrated SR tuning without affecting LR in PEGASASS. To demonstrate this capability experimentally, the PSFs and OIDs were recorded again under modified illumination and filtering conditions. Specifically, Element 1 (red LED, λ = 660 nm, 940 mW) in the setup was replaced with a green LED (Thorlabs, λ = 554 nm, 650 mW), and Element 13 (bandpass filter with λ = 633 nm and Δλ = 5 nm) was replaced with a bandpass filter (Thorlabs FLH532-4, λ = 532 nm and Δλ = 4 nm). In this experiment, the axial location was kept constant for both objects at z_s = 5.3 cm, while the illumination wavelength was varied such that object '4' was illuminated with green light and object '1' with red light. The experimental results of 3D imaging (x, y, λ) with SR control post-recording are shown in **Figure 44(a)**.

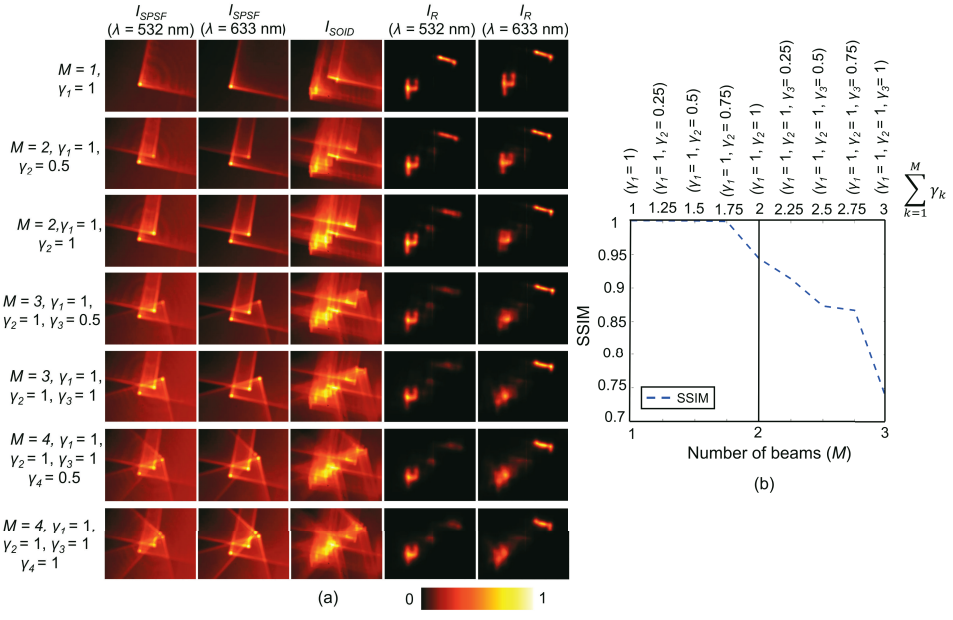

Figure 44. Experimental results of PEGASASS (SR engineering post-recording): Column 1 – I_{SPSF} (λ = 532 nm), Column 2 – I_{SPSF} (λ = 633 nm), Column 3 – I_{SOID}, and Column 4 and Column 5 reconstruction results by LRRA corresponding to two wavelengths I_R (λ = 532 nm) and I_R (λ = 633 nm), shown for M =1 to 4 and z_s = 5.3 cm, respectively. **(b)** Plot of SSIM for different number of beams. (Adapted from **Publication III**)

The I_{SPSF} (λ = 532 nm), I_{SPSF} (λ = 633 nm), $I_{SOID,}$ and their reconstruction results corresponding to two wavelengths, I_R (λ = 532 nm) and I_R (λ = 633 nm), using LRRA for M = 1 to 4 and γ incremented by 0.5, are shown in columns 1–5, respectively, of **Figure 44(a)**. Comparing the reconstruction results across the different cases, it is observed that as M increases, the SR increases. When M = 1, corresponding to a single Airy beam in the ensemble, reconstruction using the I_{SPSF} of either wavelength results in both objects ('4' and '1') appearing perfectly focused, despite being illuminated by different wavelengths.

This behaviour indicates a low SR. When M = 2 and γ_2 = 0.5, reconstruction using I_{SPSF} corresponding to a given wavelength results in a perfect reconstruction of the object illuminated at that wavelength, while the object illuminated at the other wavelength begins to blur. This behaviour indicates an increase in SR compared to the M = 1 case. As M is increased further, the blurring of information from non-matching wavelengths becomes progressively stronger, clearly demonstrating improvement in SR. To quantitatively assess the variation in SR, the degree of blur in the reconstructed images was evaluated using the SSIM. The variation of SSIM, indicating the variation of SR with respect to k, is shown in **Figure 44(b)**. Once again, when the number of beams increased, the blur increased, resulting in a decrease in SSIM, demonstrating an improvement in SR.

The PEGASASS experimental results of 4D imaging (x, y, z, λ) with simultaneous control of AR and SR post-recording are shown in **Figure 45**. The I_{SPSF} (z_s = 5 cm, λ = 532 nm), I_{SPSF} (z_s = 5.3 cm, λ = 633 nm), I_{SPSF} (z_s = 5.3 cm, λ = 532 nm), and I_{SPSF} (z_s = 5 cm, λ = 633 nm) for M = 1 to 4, and γ_k = 1 for all k are shown in rows 1–4 respectively of **Figure 45**. The I_{SOID} was obtained by combining OIDs corresponding to digit '4' (z_s = 5 cm, λ = 532 nm) and digit '1' (z_s = 5.3 cm, λ = 633 nm) for M = 1 to 4, and γ_k = 1 is shown in row 5 of **Figure 45**.

The reconstruction results by LRRA corresponding to different axial locations and wavelengths I_R (z_s = 5 cm, λ = 532 nm), I_R (z_s = 5.3 cm, λ = 633 nm), I_R (z_s = 5.3 cm, λ = 532 nm) and I_R (z_s = 5 cm, λ = 633 nm) for M = 1 to 4, and γ_k = 1 are shown in rows 6–9 respectively of **Figure 45**. From the reconstruction results, trends similar to those observed in **Figures 43 and 44** are evident. As the number of intensity distributions increased, the object information corresponding to non-matching depths and wavelengths became progressively blurred, while the object information corresponding to the matched depth and wavelength remained in focus. This demonstrates that depth-specific and wavelength-specific object information can be selectively extracted from the I_{SOID} shown in row 5 of **Figure 45**. The strengths of the object information from other depths and wavelengths can be tuned post-recording by tuning M. For the entire experimental study of PEGASASS, the typical range of values of α, β, and n used in LRRA were 0.2 to 0.4, 1, and 20 to 80, respectively.

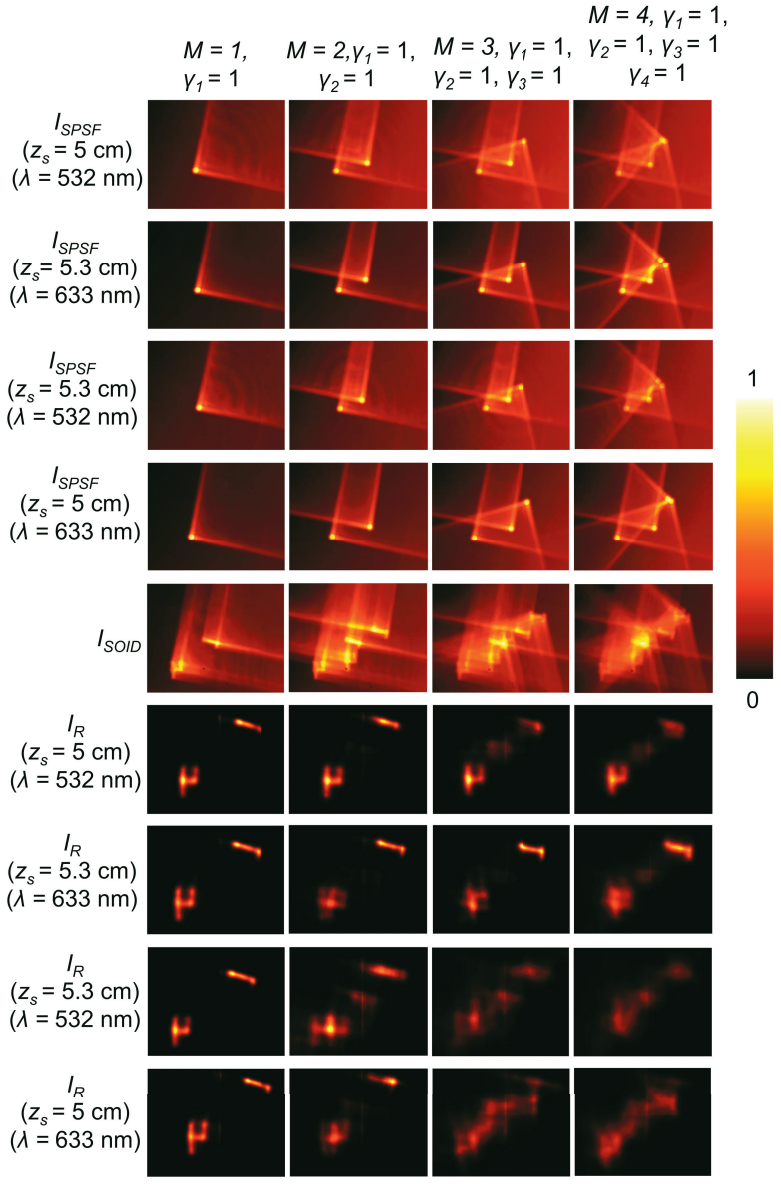

Figure 45. Experimental results of PEGASASS (Both AR and SR engineering post-recording): Row 1 – I_{SPSF} (z_s = 5 cm, λ = 532 nm), Row 2 – I_{SPSF} (z_s = 5.3 cm, λ = 633 nm), Row 3 – I_{SPSF} (z_s = 5.3 cm, λ = 532 nm), and Row 4 – I_{SPSF} (z_s = 5 cm, λ = 633 nm) shown for M = 1 to 4, and γ_k = 1, respectively. Row 5 – I_{SOID} corresponding to the objects digit '4' at (z_s = 5 cm, λ = 532 nm) and digit '1' at (z_s = 5.3 cm, λ = 633 nm) shown for M = 1 to 4, and γ_k = 1, respectively. Rows 6 to 9 – reconstruction results by LRRA corresponding to different axial locations and wavelengths I_R (z_s = 5 cm, λ = 532 nm), I_R (z_s = 5.3 cm, λ = 633 nm), I_R (z_s = 5.3 cm, λ = 532 nm) and I_R (z_s = 5 cm, λ = 633 nm) shown for M = 1 to 4, and γ_k = 1 respectively. (Adapted from **Publication III**)

4.4 PEAR-FINCH

The results of simulation studies and optical experiments are presented in the following sections.

4.4.1 Simulation studies

4.4.1.1 FINCH baseline simulations

Simulation studies were carried out for FINCH, PEAR-FINCH, and DIS using MATLAB [99]. A matrix size of 500 × 500 pixels was used, with a sampling size of $\Delta = 10$ μm. The illumination wavelength was set to $\lambda = 650$ nm. The optical configuration parameters were chosen as $z_s = 40$ cm, $z_h = 80$ cm, $f_1 = 40$ cm, and $f_2 = 20$ cm as per the equations presented in Section 3.4 of the methodology. As a first step, baseline simulations were conducted to validate the well-established advantage of FINCH over DIS in both LR and AR. Since the reconstruction plane of FINCH corresponds to the image plane of the lens with focal length $f_2 = 20$ cm, the recording plane for DIS is matched to this plane. Since the distance z_s is the same for DIS and FINCH, the baseline experiment is expected to be accurate, with the entrance pupils of DIS and FINCH exposed to the same spatial frequencies. As it is well established from previous FINCH studies, the LR in FINCH is unique because of the improvement in the response to higher spatial frequencies in the modulation transfer function without any change in the bandwidth, i.e., the maximum values of F_x and F_y, where F_x and F_y are the spatial frequencies along the x and y directions. This first simulation study was conducted to validate FINCH's higher two-point resolution compared to DIS. The PSHs of FINCH for the phase shift values $\theta = 0$, $2\pi/3$, and $4\pi/3$ are shown in **Figures 46(a)–(c)**, respectively. The magnitude and phase of the complex PSH are shown in **Figures 46(d) and 46(e)**, respectively. The reconstructed object point is shown in **Figure 46(f)**. According to the optical configuration, the resolution limit of DIS is given as $\sim \lambda z_s / D \approx 50$ μm, where $D = 5\times10^3$ μm. The two points are placed 60 μm apart, so they should be barely resolved by the DIS. The FINCH OHs for two points separated by a distance of 60 μm for phase shift values $\theta = 0$, $2\pi/3$, and $4\pi/3$ are shown in **Figures 46(g) – 46(i)**, respectively. The magnitude and phase of the complex FINCH OH are shown in **Figures 46(j) and 46(k)**, respectively. The reconstruction result of FINCH obtained by propagating the complex FINCH OH by $z_r = 40$ cm is shown in **Figure 46(l)**. The DIS result of the two points at $z_h = 40$ cm from the lens is shown in **Figure 46(m)**. The normalized plots of the line data of **Figures 46(l) and 46(m)** are shown in **Figure 46(n)**. As shown in **Figures 46(l) – 46(n)**, the superior LR of FINCH is validated.

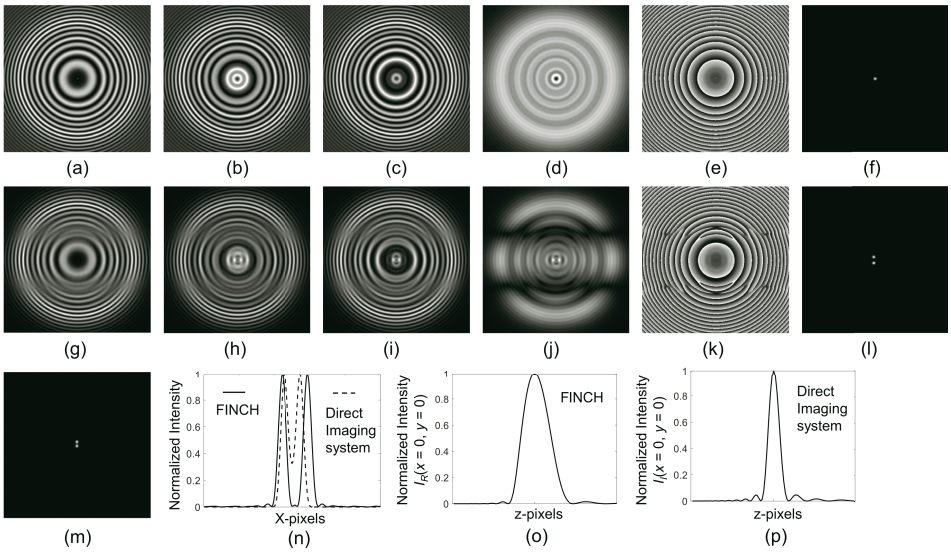

Figure 46. Baseline simulation studies of FINCH: PSHs of FINCH for **(a)** $\theta = 0$ radians, **(b)** $\theta = 2\pi/3$ radians, and **(c)** $\theta = 4\pi/3$ radians. **(d)** Magnitude and **(e)** phase of the complex PSH generated from (a)–(c). **(f)** Reconstructed point image by numerical back-propagation. OHs of FINCH for **(g)** $\theta = 0$ radians, **(h)** $\theta = 2\pi/3$ radians, and **(i)** $\theta = 4\pi/3$ radians. **(j)** Magnitude and **(k)** phase of the complex PSH generated from (g)–(i). **(l)** Reconstructed point image by numerical back-propagation. **(m)** DIS results of the two points. **(n)** Plots of the line data of the imaging results of FINCH (l) and DIS (m). **(o)** Plot of $I_R(x = 0, y = 0)$ with respect to the error in the axial location z_s for FINCH. **(p)** Plot of $I_I(x = 0, y = 0)$ with respect to the error in the axial location z_s for DIS. (Adapted from **Publication IV**)

The second simulation study was conducted to validate the longer FD of FINCH compared with that of DIS. For this simulation study, a single-point object located at the origin was considered. The object location was varied from $z_s = 20$ cm to 60 cm in 4 mm steps. For each object position, FINCH holograms were obtained and numerically combined into a complex hologram, which was then backpropagated to the same reconstruction distance, $z_r = 40$ cm. At each location of z_s, the intensity value $I_R(x = 0, y = 0)$ was obtained and plotted after normalization, as shown in **Figure 46(o)**. The same simulation procedure was repeated for the DIS under identical axial conditions, with the object position again varied from $z_s = 20$ cm to 60 cm. The plot of $I_I(x = 0, y = 0)$ for different values of z_s for DIS is shown in **Figure 46(p)**. As shown in **Figures 46(o) and 46(p)**, the greater FD of FINCH is validated. These baseline experiments confirm FINCH's performance in the simulation approach.

4.4.1.2 Focal depth of FINCH for different optical configurations

In the third simulation study, the FD of FINCH under non-optimal configurations is compared with that of the optimal configuration corresponding to the highest LR. For the study, the axial response $I_R(x = 0, y = 0)$ for the optimal configuration with $f_2 = 20$ cm is combined with the axial responses of the non-optimal configurations $\Delta f_2 = \pm 0.5$ cm and $\Delta f_2 = \pm 1$ cm. These axial responses are shown in **Figure 47**. **Figure 47(a)** presents the axial distributions $I_R(x = 0, y = 0)$ for $f_2 = 19$ cm to 21 cm in steps of 0.5 cm. In all cases, the reconstruction distance z_r was maintained at the optimal value of $z_r = 40$ cm. This is a crucial requirement, as when considering holograms from different cases, reconstruction can be carried out for only one plane of interest at a time. Interestingly, the axial curves start to have more than one peak when z_r and f_2 are not matched in the non-optimal cases, as is the case for the optimal configuration.

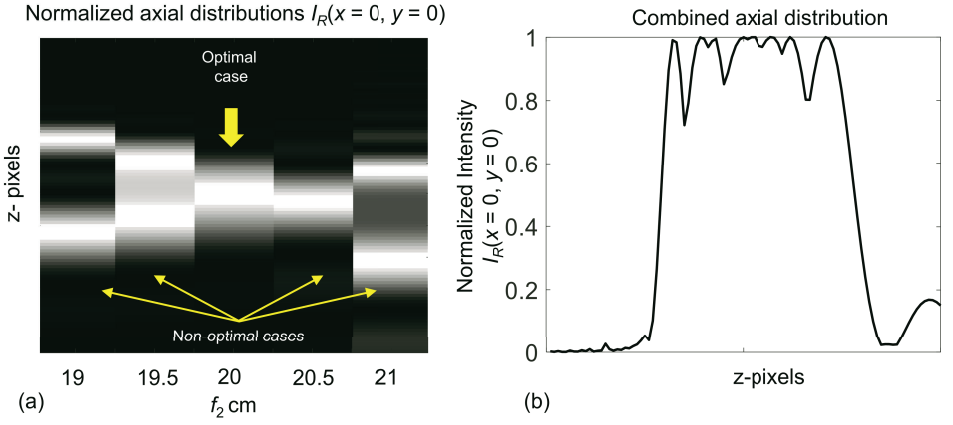

Figure 47. FD of FINCH for different optical configurations: (a) Images of normalized axial distributions $I_R(x = 0, y = 0)$ for $\Delta f_2 = 0$, $\Delta f_2 = \pm 0.5$ cm, and $\Delta f_2 = \pm 1$ cm. **(b)** Plot of the combined axial distribution. (Adapted from **Publication IV**)

The combined axial distribution, obtained by taking the global maxima of each curve, is shown in **Figure 47(b)**. The resulting axial distribution is almost uniform, with a high response for a range of axial location errors. The final distribution is obtained by stitching the axial curves from different FINCH configurations. Since, with every new configuration, a new hologram with a unique axial curve can be obtained, the axial distribution can be precisely tailored, given the larger basis of holograms with diverse axial distributions. The main advantage is that the proposed sculpting of the axial distribution can be performed after the FINCH recording is complete.

4.4.2 Experimental studies

The photograph of the experimental setup used for demonstrating the concept of PEAR-FINCH is shown in **Figure 48**. The setup includes the following optical components from Thorlabs: (1) M660L4 light-emitting diode (LED) with 940 mW power, operating at a wavelength of $\lambda = 660$ nm, and a bandwidth of $\Delta\lambda = 20$ nm; (2) ID50/M standard iris, Ø50.0 mm max aperture; (3) DG05-220 grit – Ø1/2" N-BK7 ground glass diffuser; (4) N-BK7 Ø1" biconvex refractive lens with a focal length (f = 7.5 cm); (5) ID50/M standard iris, Ø50.0 mm max aperture; (6) Ø1" linear polarizer with N-BK7 windows; (7) ID20/M standard iris, Ø20.0 mm max aperture; (8) N-BK7 Ø1" biconvex refractive lens with a focal length (f = 5 cm); (9) Ø1" pinhole of size (50 µm) or test object (digit '2' or digit '4') from group 3 in R1DS1N Negative USAF test target, (10) N-BK7 Ø1" bi-convex lens refractive lens with a focal length (f = 5 cm), (11) ID20/M standard iris, Ø20.0 mm max aperture, (12) BS031 50:50 non-polarizing beam splitter cube, (13) Exulus HD2 SLM with 1920 × 1200 pixels and having a pixel size of 8 µm, (14) Ø1" linear polarizer with N-BK7 windows, (15) FLH633-5 band pass filter with a wavelength of $\lambda = 633$ nm and a bandwidth of $\Delta\lambda = 5$ nm and (16) Zelux CS165MU/M monochrome image sensor with 1440 × 1080 pixels and having a pixel size of ~3.5 µm.

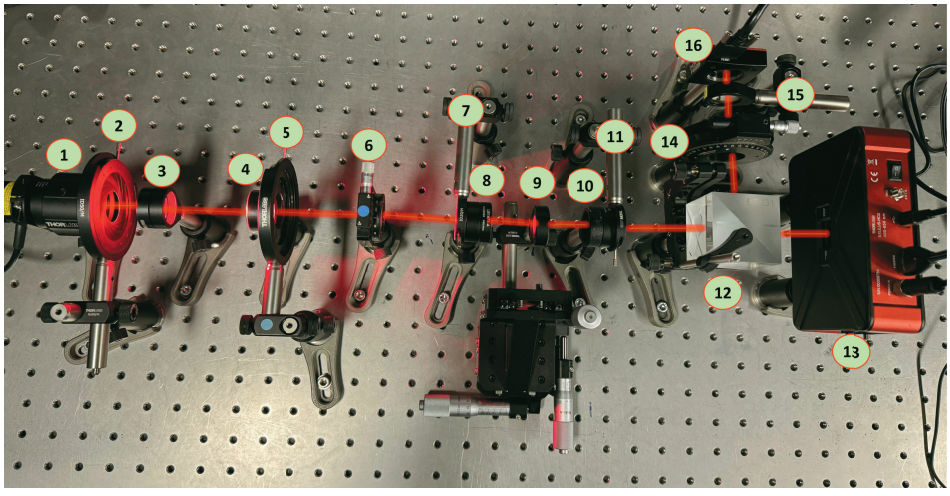

Figure 48. Photograph of the experimental setup used for demonstration. (1) LED ($\lambda = 660$ nm), (2) iris, (3) diffuser, (4) refractive lens (f = 7.5 cm), (5) iris, (6) first polarizer (P_1), (7) iris, (8) refractive lens (f = 5 cm), (9) object/pinhole, (10) refractive lens (f = 5 cm), (11) iris, (12) beam splitter, (13) SLM, (14) second polarizer (P_2), (15) bandpass filter, (16) monochrome image sensor. The beam path from the LED to the image sensor is indicated in red. (Adapted from **Publication IV**)

The experimental setup consists of a high-power LED source, whose beam diameter is controlled with an iris, and then directed onto a diffuser. The diffused light is collected by a refractive lens (f = 7.5 cm) and then passed through the first polarizer, P_1, which is aligned with the SLM's active axis. Two irises placed

before and after the first polarizer, P_1, suppress stray light entering the recording unit. The object/pinhole was critically illuminated using a refractive lens (f = 5 cm), and the transmitted light from the object was collected by a second refractive lens (f = 5 cm). An iris was used to control the beam size such that the collimated beam passing through the beam splitter illuminates the central region of the SLM. The phase masks for DIS, FINCH, and PEAR-FINCH **Figure 49(b–d)** were designed in MATLAB [99] based on the SLM specifications (operating wavelength range of 400–850 nm, pixel size of 8 µm, panel resolution of 1920×1200). The designed phase masks were exported as bitmap images compatible with the SLM controller. The SLM was connected directly to the computer and operated using the Thorlabs control software, which allows bitmap phase masks to be loaded and displayed without additional pre-processing. During recording, the phase masks were displayed sequentially. For DIS, the single diffractive lens mask shown in **Figure 49(b)** was displayed. For FINCH and PEAR-FINCH, the three phase-shifted masks (θ = 0, 2π/3, 4π/3) associated with each focal-length configuration, as shown in **Figures 49(c) and 49(d)**, were displayed one after another. After each mask was displayed on the SLM, a short stabilization period of 2–3 seconds was allowed before capturing the corresponding hologram with the image sensor. This ensured stable SLM rendering and consistent hologram formation. The second polarizer, P_2, is also aligned with the SLM's active axis and placed after the SLM. A bandpass filter was used to improve fringe visibility in the recorded holograms. The imaging distance from the SLM to the image sensor was z_h = 20 cm. The experimentally recorded data were subsequently processed in MATLAB [99], where the computational reconstruction was performed, and the figures were generated, as shown in the upcoming part of this section.

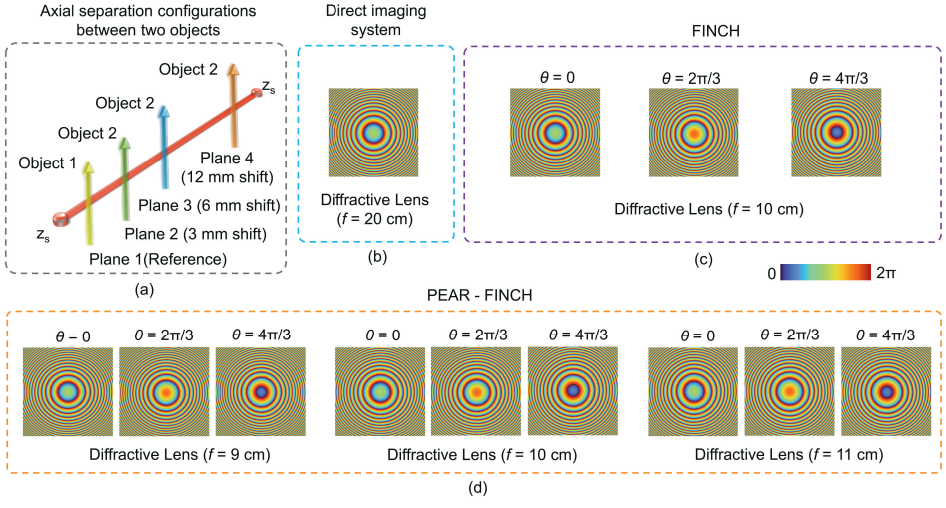

Figure 49. (a) Axial-separation configurations between two objects. **(b)** Phase mask for DIS – diffractive lens (f = 20 cm). **(c)** Phase masks for FINCH – diffractive lens (f = 10 cm) with phase shift values θ = 0, 2π/3, and 4π/3. **(d)** Phase masks for the PEAR-FINCH diffractive lens (f = 9, 10, and 11 cm) with phase shift values θ = 0, 2π/3, and 4π/3. (Adapted from **Publication IV**)

Two standard test objects, digits '2' and '4', were used and are referred to as Object 1 and Object 2, respectively. To demonstrate the core concept of PEAR-FINCH, four object planes with different axial separations were selected as shown in **Figure 49(a)**. Plane 1 served as the reference plane, where Object 1 was fixed. Object 2 was placed sequentially at three additional planes: Plane 2, Plane 3, and Plane 4, located at axial distances of 3 mm, 6 mm, and 12 mm from Plane 1, respectively. These axial separations were chosen intentionally to evaluate and compare the FD performance of DIS, FINCH, and PEAR-FINCH. When Object 2 is positioned at Plane 2 (3 mm axial shift), DIS failed to resolve Object 2 due to its limited FD. In contrast, FINCH reconstructed Object 2 because FINCH typically exhibits a larger FD than DIS. Therefore, Plane 2 was used to validate the expected behaviour of the DIS and FINCH experimentally. The larger axial separations of 6 mm (Plane 3) and 12 mm (Plane 4) were selected to test the PEAR-FINCH concept under conditions in which neither DIS nor conventional FINCH can reliably resolve Object 2, thereby making these configurations suitable for demonstrating FD extension through post-engineering. In addition, the object shown in element 9 of **Figure 48(b)** was mounted on a 3-axis translation stage, and Plane 4 (12 mm shift) corresponds to the maximum achievable axial displacement from Plane 1 within the mechanical travel range of the 3-axis translation stage. Thus, the chosen planes reflect both the conceptual requirements for validating FD behaviour and the practical constraints of the experimental system. A diffractive lens with a focal length $f = 20$ cm, as shown in **Figure 49(b)**, was displayed on the SLM to record direct images of the objects.

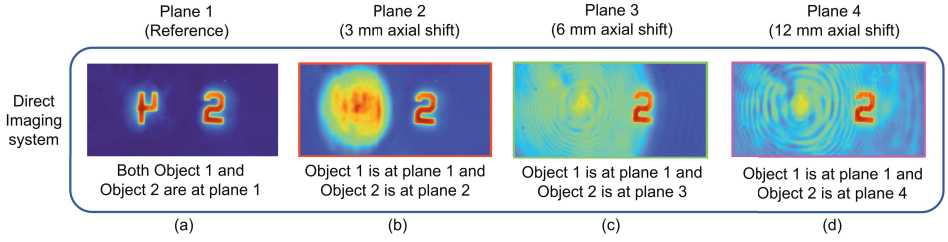

Figure 50. DIS results for the different axial-separation configurations **(a)** Both Objects are placed at plane 1 (reference), Object 1 (digit '2') is placed at plane 1 (reference), and Object 2 (digit '4') is placed at planes: **(b)** plane 2 (3 mm axial shift), **(c)** plane 3 (6 mm axial shift), and **(d)** plane 4 (12 mm axial shift). (Adapted from **Publication IV**)

As a preliminary step, the FD of the DIS was evaluated by recording images of the objects placed at different axial planes. The DIS results are shown in **Figure 50**. When both objects were positioned on plane 1, they appeared in perfect focus, as shown in **Figure 50(a)**. When Object 1 remained at plane 1 and Object 2 was shifted to plane 2, Object 2 became blurred as seen in **Figure 50(b)**. As Object 2 was further displaced to planes 3 and 4, the degree of blurring increased progressively, as observed in **Figures 50(c) and 50(d)**, respectively. These results clearly indicate that in conventional DIS, the object information is resolved only when

the object lies at the focal plane. Even a small axial displacement results in noticeable blurring due to DIS's limited FD.

In the next step, FINCH's FD performance was evaluated. FINCH was implemented using the PM configuration. Accordingly, the polarizers P_1 and P_2, placed before and after the SLM in the setup, were oriented at 45° relative to the SLM's active axis. The first polarizer, P_1, ensured that approximately 50% of the incident light was modulated by the diffractive lens displayed on the SLM, while the remaining light remained unmodulated. The second polarizer, P_2, was also oriented at 45°, enabling interference between the modulated and unmodulated beams, which is essential for FINCH hologram formation. The phase masks shown in **Figure 49(c)** were sequentially displayed on the SLM, and the corresponding phase-shifted FINCH OHs were recorded.

The 3D imaging results of FINCH for different axial-separation configurations are shown in **Figure 51**. In these experiments, Object 1 (digit '2') was fixed at plane 1, which served as the reference plane, while Object 2 (digit '4') was placed sequentially at plane 2 (3 mm axial shift), plane 3 (6 mm axial shift), and plane 4 (12 mm axial shift). The phase-shifted OHs corresponding to phase shift values $\theta = 0$, $2\pi/3$, and $4\pi/3$, along with the magnitude and phase of the resulting complex OHs for the axial combinations plane 1 + plane 2, plane 1 + plane 3, and plane 1 + plane 4 (corresponding to $f = 10$ cm), are shown in **Figure 51(a)**. The reconstruction results obtained by numerical back-propagation are shown in **Figure 51(b)**, with plane 1 + plane 2 (outlined in red), plane 1 + plane 3 (outlined in green), and plane 1 + plane 4 (outlined in magenta). In all three reconstruction cases, the reconstruction distance was kept constant and corresponds to plane 1 ($z_r = 10$ cm).

In the first reconstruction result (outlined in red), both Object 1 and Object 2 appear in focus, even though Object 2 was located 3 mm away from plane 1. This demonstrates the relatively higher FD provided by FINCH compared to that of DIS. When Object 2 was shifted to plane 3 (6 mm axial-separation), it began to appear blurred, as shown in the reconstruction result outlined in green. When Object 2 was further shifted to plane 4 (12 mm axial-separation), it became significantly blurred, as shown in the reconstruction outlined in magenta. In all these cases, Object 1 remained focused because the reconstruction distance matched its location on plane 1. These results indicate that although FINCH offers an improved FD compared to DIS, its effective FD remains limited, and object information located beyond this range cannot be reliably resolved. This limitation motivated the development of the PEAR-FINCH method to extend the effective FD beyond FINCH's conventional limits.

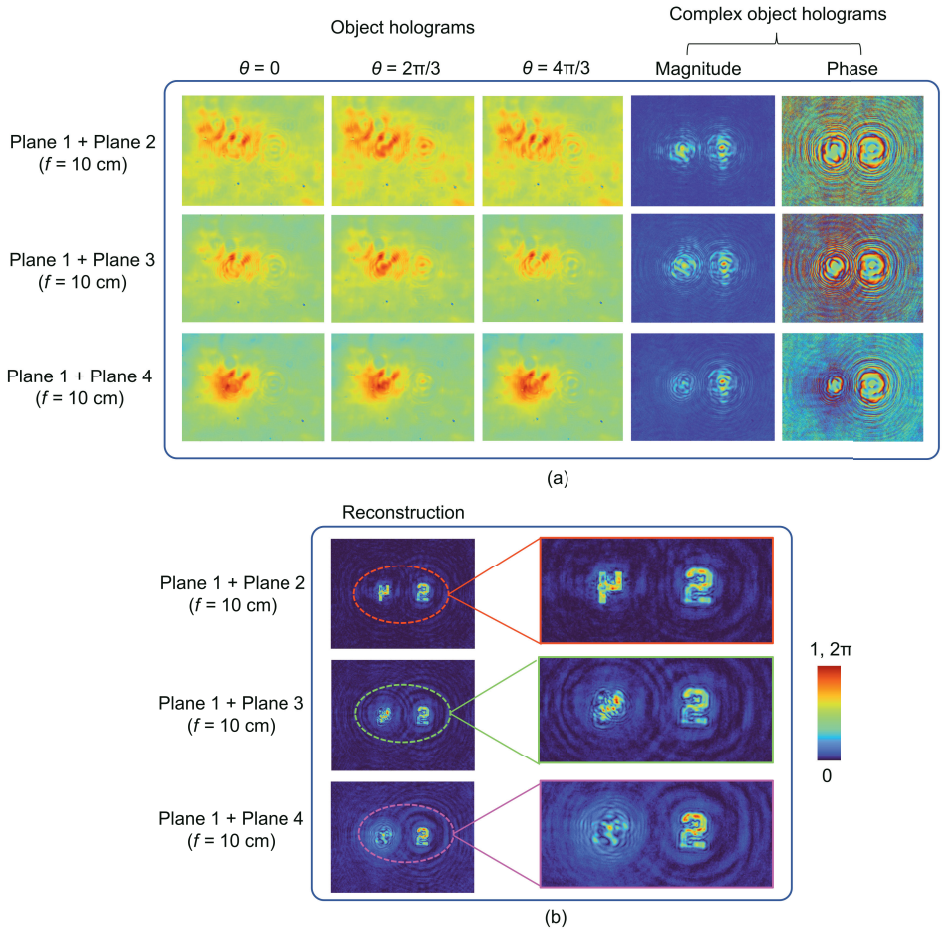

Figure 51. FINCH 3D imaging results for the different axial-separation configurations where Object 1 (digit '2') was placed at plane 1 (reference) and Object 2 (digit '4') was placed at planes 2 (3 mm axial shift), 3 (6 mm axial shift), and 4 (12 mm axial shift). **(a)** Phase-shifted OHs corresponding to phase shift values θ = 0, 2π/3, and 4π/3, the magnitude and phase of the resulting complex OHs for plane1 (f = 10 cm) + plane 2 (f = 10 cm), plane 1 (f = 10 cm) + plane 3 (f = 10 cm), and plane 1 (f = 10 cm) + plane 4 (f = 10 cm). **(b)** The reconstruction results by numerical back-propagation to z_r = 10 cm, for plane 1 + plane 2 (outlined in red), plane 1 + plane 3 (outlined in green), and plane 1 + plane 4 (outlined in magenta). (Adapted from **Publication IV**)

Now the goal of the PEAR-FINCH method is to reconstruct the information of Object 2 when it is located at plane 3, which is axially separated by 6 mm from the reference plane 1, a condition where conventional FINCH and DIS fail to resolve Object 2. In PEAR-FINCH, this is achieved by varying the focal length of the diffractive lenses displayed on the SLM and recording the corresponding OHs. These OHs collectively covered the depth range of interest in our experiment, thereby extending the effective FD beyond those of FINCH and DIS. The focal length f =10 cm corresponds to the optimal FINCH configuration and

primarily provides axial distribution near the reference plane. To extend the FD beyond this FINCH limit, two additional focal lengths, $f = 9$ cm and $f = 11$ cm, were selected. Under these modified focal length conditions, the two interfering beams do not overlap perfectly at the sensor plane, resulting in distinct axial intensity distributions, reconstruction distances, and FDs for each configuration. The spacing between the focal lengths was chosen carefully: if the focal lengths are too close, their axial responses overlap significantly, making the additional holograms redundant; if they are too far apart, the axial distributions do not overlap sufficiently, leaving gaps in depth coverage. The selected focal lengths, therefore, generate complementary axial distributions which, when combined, enable the SOH to exhibit an extended effective FD as observed from Section 4.4.1.2.

So, initially, the SOH was reconstructed using numerical back-propagation to the reconstruction distance corresponding to plane 1 (z_r = 10 cm), where both objects are in focus. However, this reconstruction exhibits a low SNR because the SOH contains contributions from multiple OHs with different axial characteristics. As a result, reconstruction at a specific distance includes both sharp and blurred components, which, when combined, lead to low SNR. To improve the SNR, an SPSH is obtained under identical conditions, but recorded only at plane 1, using diffractive lenses with focal lengths $f = 9$ cm, $f = 10$ cm, and $f = 11$ cm. A cross-correlation is then performed between the reconstructed image of the object and the reconstructed image of the point object using the LRRA. This process enhances the SNR and improves the quality of the final reconstructed image. Accordingly, in addition to the OH recorded at planes 1 and 3 using three diffractive phase-shifted lenses with a focal length of $f = 10$ cm, six additional phase-shifted OHs were recorded using diffractive lenses with focal lengths of $f = 9$ cm and $f = 11$ cm, as shown in **Figure 49(d)**. For each focal length condition, the phase-shifted OHs were first superposed to generate the individual complex OH. These complex OHs are then summed to generate the SOH, which exhibits an extended FD due to the combination of multiple distinct axial distributions. The object information was reconstructed from the SOH in two stages: first, by numerical back-propagation to the desired reconstruction distance, and second, by the deconvolution using LRRA with the SPSH, which was recorded and processed under identical conditions. This two-step reconstruction produces the final image with extended FD and improved SNR.

The 3D imaging results of PEAR-FINCH for the axial-separation configuration where Object 1 (digit '2') was placed at plane 1 and Object 2 (digit '4') was placed at plane 3 (6 mm axial shift) are shown in **Figure 52**. The phase-shifted OHs corresponding to phase shift values $\theta = 0$, $2\pi/3$, and $4\pi/3$, the magnitude and phase of the complex OHs for plane 1 ($f = 9$ cm) + plane 3 ($f = 9$ cm), plane 1 ($f = 10$ cm) + plane 3 ($f = 10$ cm), and plane 1 ($f = 11$ cm) + plane 3 ($f = 11$ cm) are shown in **Figure 52(a)**. The phase-shifted PSHs corresponding to phase shift values $\theta = 0$, $2\pi/3$, and $4\pi/3$, and the magnitude and phase of the complex PSHs for plane 1 for $f = 9$, 10, and 11 cm are shown in **Figure 52(b)**. The magnitude and phase of the complex SOH and SPSH are shown in **Figure 52(c)**.

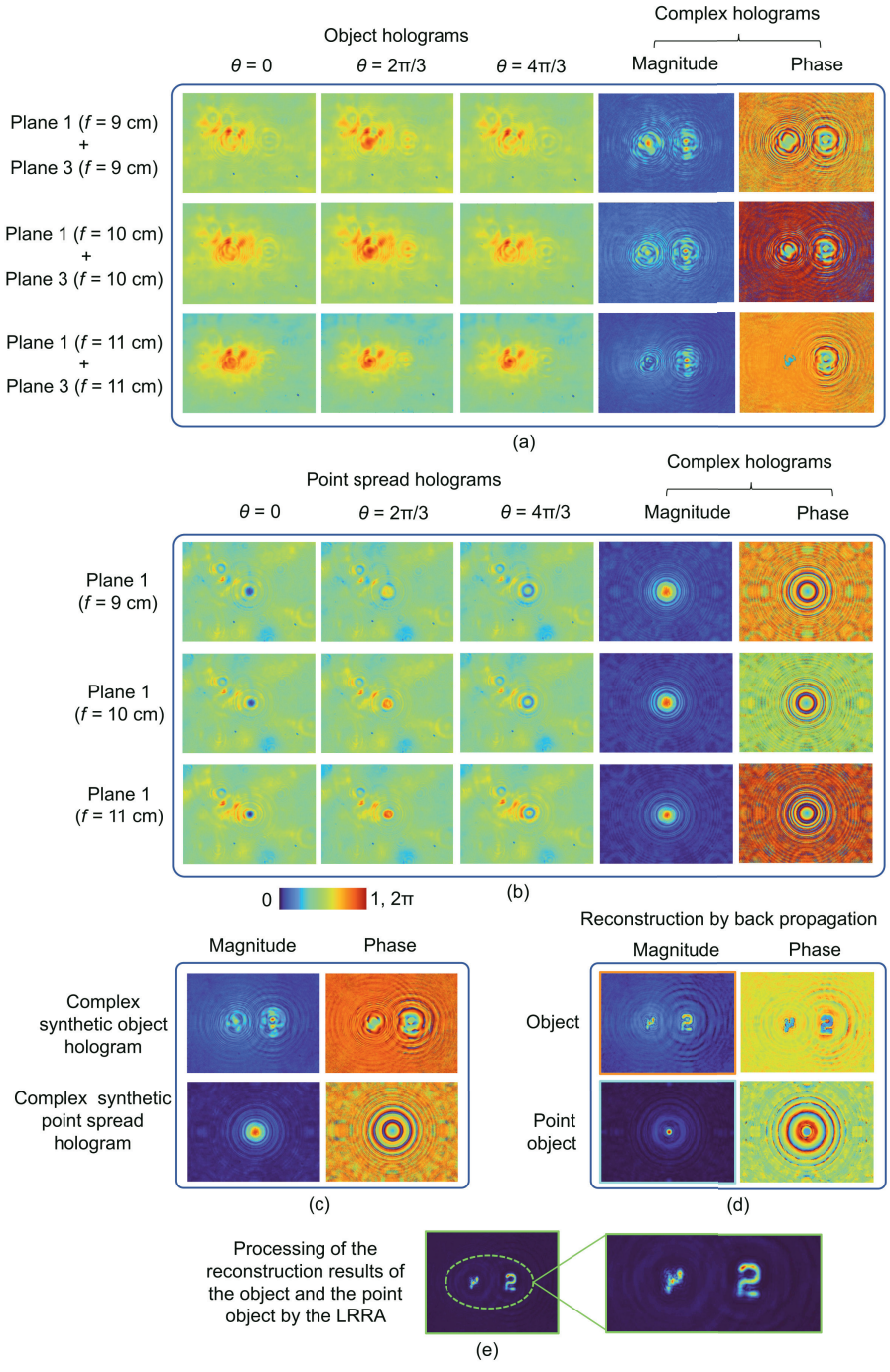

Figure 52: PEAR-FINCH 3D imaging results for the axial-separation configuration where Object 1 (digit '2') was placed at plane 1 and Object 2 (digit '4') was placed at plane 3 (6 mm axial shift). **(a)** Phase-shifted OHs corresponding to phase shift values $\theta = 0$, $2\pi/3$, and $4\pi/3$, the magnitude and phase of the complex OHs for plane 1 ($f = 9$ cm) + plane 3 ($f = 9$ cm), plane 1 ($f = 10$ cm) + plane 3 ($f = 10$ cm), and plane 1 ($f = 11$ cm) + plane 3 ($f = 11$ cm). **(b)** Phase-shifted PSHs corresponding to phase shift

values $\theta = 0$, $2\pi/3$, and $4\pi/3$, the magnitude and phase of the complex PSHs for plane 1 ($f = 9$, 10, and 11 cm). **(c)** The magnitude and phase of the complex SOH and SPSH. **(d)** The magnitude (outlined in orange) and phase of the reconstructed object by numerical back-propagation to $z_r = 10$ cm; the magnitude (outlined in cyan) and phase of the reconstructed point object by numerical back-propagation to $z_r = 10$ cm. **(e)** Processing of the reconstructed object and the point object shown in (d) via LRRA (outlined in green). (Adapted from **Publication IV**)

The magnitude (outlined in orange) and phase of the reconstruction of the object by numerical back-propagation to plane 1 ($z_r = 10$ cm); the magnitude (outlined in cyan) and phase of the reconstruction of the point object by numerical back-propagation to plane 1 ($z_r = 10$ cm) are shown in **Figure 52(d)**. The magnitude of the reconstruction (outlined in orange) indicates that both Object 1 and Object 2 are in focus, confirming that the PEAR-FINCH achieves a greater FD extension than that of FINCH. The final reconstruction result shown in **Figure 52(e)** (outlined in green) with an improved SNR was obtained by processing the reconstructed object and the reconstructed point object shown in **Figure 52(d)** by LRRA. The optimal reconstruction values used correspond to the LRRA parameters n, α, and β, which are 3, 0.84, and 1, respectively.

The same procedure is used to retrieve the information of Object 2, which lies on plane 4 (12 mm axially located away from plane 1), using the PEAR-FINCH. In addition to the OH recorded at planes 1 and 4 using three-phase-shifted diffractive lens masks with a focal length of $f = 10$ cm, six additional phase-shifted OHs were recorded using diffractive lens masks with focal lengths of $f = 9$ cm and $f = 11$ cm, as shown in **Figure 49(d)**. The SOH was generated similarly, and the SPSH obtained at plane 1 was used to improve the SNR by LRRA. The 3D imaging results of PEAR-FINCH for the axial-separation configuration where Object 1 (digit '2') was placed at plane 1 and Object 2 (digit '4') was placed at plane 4 (12 mm axial shift) are shown in **Figure 53**. The phase-shifted OHs corresponding to phase shift values $\theta = 0$, $2\pi/3$, and $4\pi/3$, the magnitude and phase of the complex OHs for plane 1 ($f = 9$ cm) + plane 4 ($f = 9$ cm), plane 1 ($f = 10$ cm) + plane 4 ($f = 10$ cm), and plane 1 ($f = 11$ cm) + plane 4 ($f = 11$ cm) are shown in **Figure 53(a)**. The phase-shifted PSHs corresponding to phase shift values $\theta = 0$, $2\pi/3$, and $4\pi/3$, and the magnitude and phase of the complex PSHs for plane 1 with focal lengths $f = 9$, 10, and 11 cm are shown in **Figure 53(b)**.

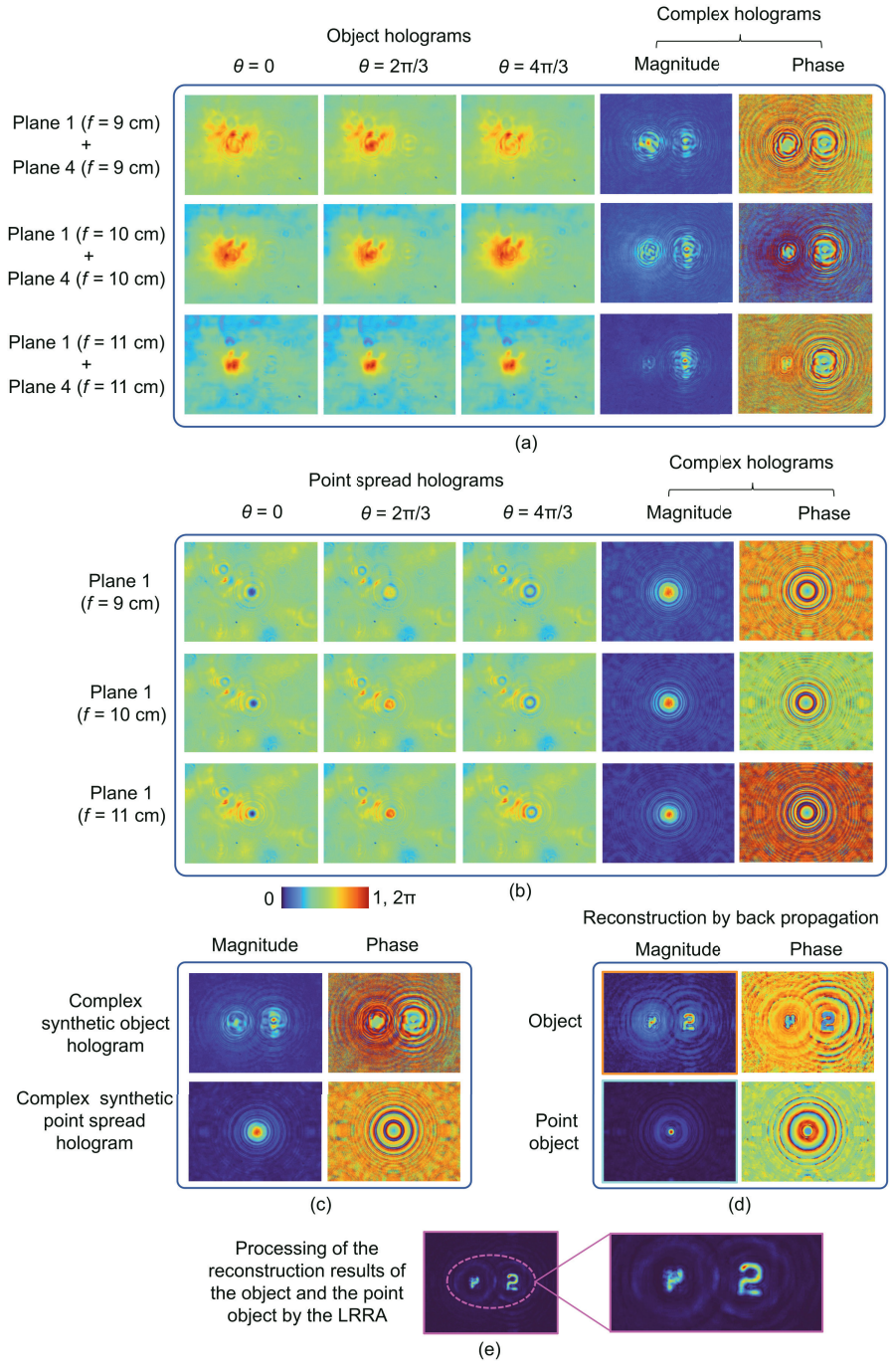

Figure 53: PEAR-FINCH 3D imaging results for the axial-separation configuration where Object 1 (digit '2') was placed at plane 1 and Object 2 (digit '4') was placed at plane 4 (12 mm axial shift). **(a)** Phase-shifted OHs corresponding to phase shift values $\theta = 0$, $2\pi/3$, and $4\pi/3$, the magnitude and phase of the complex OHs for plane 1 ($f = 9$ cm) + plane 4 ($f = 9$ cm), plane 1 ($f = 10$ cm) + plane 4 ($f = 10$ cm), and plane 1 ($f = 11$ cm) + plane 4 ($f = 11$ cm). **(b)** Phase-shifted PSHs corresponding to phase shift

values $\theta = 0$, $2\pi/3$, and $4\pi/3$, the magnitude and phase of the complex PSHs for plane 1 ($f = 9$, 10, and 11 cm). **(c)** The magnitude and phase of the complex SOH and SPSH. **(d)** The magnitude (outlined in orange) and phase of the reconstructed object by numerical back-propagation to $z_r = 10$ cm; the magnitude (outlined in cyan) and phase of the reconstructed point object by numerical back-propagation to $z_r = 10$ cm. **(e)** Processing of the reconstructed object and the point object shown in (d) via LRRA (outlined in magenta). (Adapted from **Publication IV**)

The magnitude and phase of the complex SOH and SPSH are shown in **Figure 53(c)**. The magnitude (outlined in orange) and phase of the reconstructed object by numerical back-propagation to plane 1 ($z_r = 10$ cm); the magnitude (outlined in cyan) and phase of the reconstructed point object by numerical back-propagation to plane 1 ($z_r = 10$ cm) are shown in **Figure 53(d)**. The magnitude of the reconstruction (outlined in orange) indicates that both Object 1 and Object 2 are in focus, confirming that the FD is extended even more as Object 2 is located at the farthest point from plane 1 by the PEAR-FINCH method.

The final reconstruction result shown in **Figure 53(e)** (outlined in magenta) with an improved SNR was obtained by processing the reconstructed object and the reconstructed point object shown in **Figure 53(d)** by LRRA. The optimal reconstruction values for the LRRA parameters n, α, and β are 3, 0.99, and 1, respectively. For both PEAR-FINCH axial-separation configuration results shown in **Figures 52(e) and 53(e)**, the LRRA reconstruction parameters α, β, and n were selected based on the optimal reconstruction defined by one of the figures of merit, such as SSIM or entropy. The above can be automated, and the global maxima or minima of these figures of merit can be found. In practice, we monitored image entropy and visual noise level during reconstruction and selected the parameter set that yielded the lowest entropy and the least noisy result while maintaining stable convergence.

The experimental results obtained using DIS, FINCH, and PEAR-FINCH for different axial-separation configurations are compared in **Figure 54**. PEAR-FINCH clearly demonstrates superior performance, as both Object 1 and Object 2 remain in perfect focus even when Object 2 is placed at planes 3 and 4. This behaviour indicates a substantially extended FD compared with both FINCH and DIS. To quantitatively validate the performance improvement achieved by PEAR-FINCH, the SSIM was calculated using MATLAB's built-in SSIM(A, *ref*) function [99], where A was the reconstructed image being evaluated, and *ref* was the reference image for Object 2 when it was positioned at planes 3 and 4 for all three methods. The corresponding SSIM comparison is shown as a bar plot in **Figure 54(b)**.

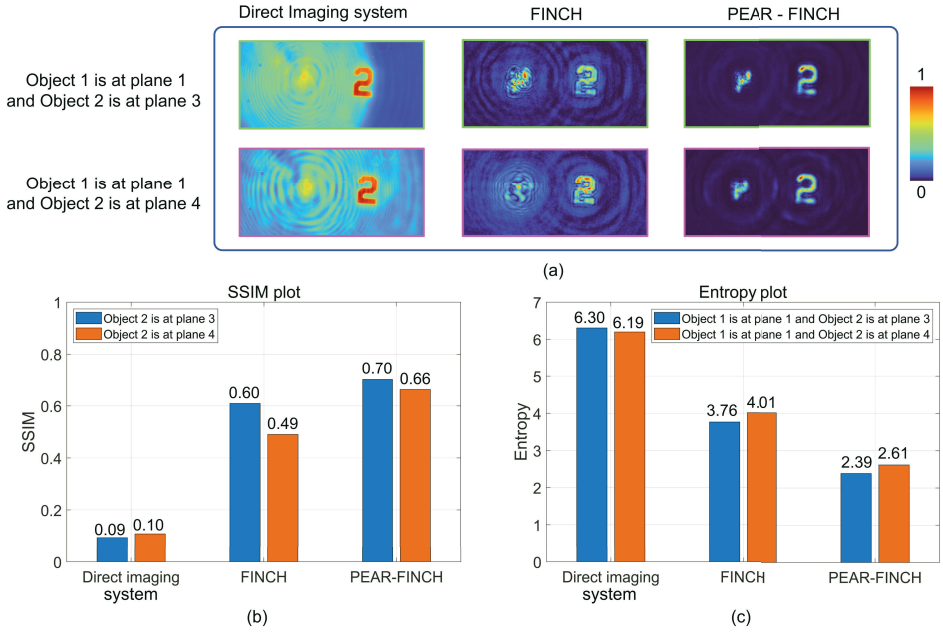

Figure 54: (a) Comparison results of DIS, FINCH, and PEAR-FINCH for different axial-separation configurations: Object 1 was at plane 1 and Object 2 is at plane 3 (outlined in green); Object 1 was at plane 1 and Object 2 was at plane 4 (outlined in magenta). **(b)** SSIM bar plot of DIS, FINCH, and PEAR-FINCH for Object 2 at plane 3 and Object 2 at plane 4. **(c)** entropy bar plot of DIS, FINCH, and PEAR-FINCH for Object 1 at plane 1 and Object 2 at plane 3, and Object 1 at plane 1 and Object 2 at plane 4. (Adapted from **Publication IV**)

Compared to DIS and FINCH, PEAR-FINCH consistently yielded higher SSIM values, confirming superior preservation of structural information at larger axial separations. Quantitatively, relative to FINCH, PEAR-FINCH improved SSIM by ~15% when Object 2 was located at plane 3 and by ~35% when Object 2 was located at plane 4. The improvement relative to DIS is substantially larger, owing to DIS's inherently narrow FD, with SSIM increasing by ~652% for plane 3 and ~515% for plane 4. In addition to SSIM, image entropy was evaluated using MATLAB's built-in entropy(A) function [99] as a measure of reconstruction noise over the entire image plane. Entropy values were calculated for configurations in which Object 1 was placed on plane 1 and Object 2 on planes 3 and 4, across all three imaging methods. The resulting entropy comparison is shown as a bar plot in **Figure 54(c)**. PEAR-FINCH consistently exhibits lower entropy values than both DIS and FINCH, indicating improved SNR. Quantitatively, relative to FINCH, PEAR-FINCH reduces entropy by ~36% for plane 3 and ~34% for plane 4. Relative to DIS, the entropy reduction achieved by PEAR-FINCH is ~62% for plane 3 and ~57% for plane 4. These consistent and substantial improvements in both SSIM and entropy confirm that PEAR-FINCH achieves significantly higher reconstruction fidelity and lower noise than conventional FINCH and DIS under large axial-separation conditions.

4.4.2.1 Axial characteristics analysis for PEAR-FINCH

To investigate the axial response characteristics of different focal length conditions employed in PEAR-FINCH, an axial response analysis based on a gradient energy metric was performed in MATLAB [99] for Object 2 (digit '4') positioned at plane 4, which is 12 mm axially separated from the reference plane. This configuration represents the most challenging case (larger axial-separation), in which both DIS and FINCH failed to resolve Object 2.

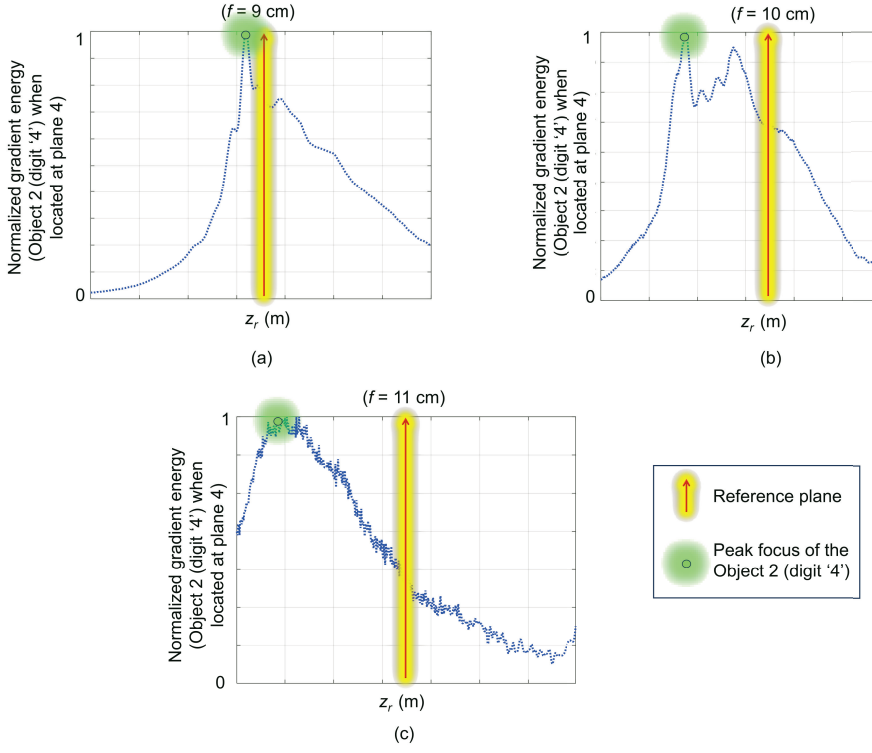

Figure 55: Normalized gradient energy plotted as a function of z_r for Object 2 (digit '4') located at plane 4. The curves correspond to different focal length conditions used in PEAR-FINCH: **(a)** $f = 9$ cm, **(b)** $f = 10$ cm, and **(c)** $f = 11$ cm.

Gradient energy metrics are widely used in imaging and autofocus applications to quantify image sharpness, as they capture high-spatial-frequency content and edge strength, which peak at best focus [102, 103]. For each focal length condition used for SOH generation in PEAR-FINCH ($f = 9$ cm, 10 cm, and 11 cm), the three phase-shifted OHs were first superposed to form the corresponding complex OH. Then, the complex OH was numerically backpropagated over a sufficiently large axial range for 500 uniformly spaced reconstruction distances. At each reconstruction distance, a fixed region containing only Object 2 (digit '4') was selected. The gradient energy value at each reconstruction distance was calculated by computing the horizontal and vertical spatial gradients of the magnitude

of the reconstructed complex field within the selected region using MATLAB's built-in gradient(I) function. Here, I corresponds to the selected region of the reconstructed field magnitude. The metric is defined as the mean squared magnitude of the gradients within the selected region, $F(z_r) = mean\left(G_x^2 + G_y^2\right)$ where $G_x = \frac{\partial I}{\partial x}$ and $G_y = \frac{\partial I}{\partial y}$ denote the horizontal and vertical spatial gradients of the reconstructed field magnitude I, respectively. The mean value is taken over all pixels in the selected region using MATLAB's built-in mean() function. The resulting metric values were normalized by the maximum value over all reconstruction distances to obtain the normalized gradient energy metric. A sharply focused object contains high spatial-frequency components and well-defined edges, resulting in strong gradients, whereas a blurred object exhibits smoother spatial variations in the reconstructed field magnitude and therefore weaker gradients. Consequently, the gradient energy metric reaches its maximum when the object is best focused and decreases as the reconstruction distance moves away from the optimal focus plane. The variation of the normalized gradient energy metric as a function of reconstruction distance, therefore, forms an axial response curve.

The resulting normalized gradient energy metric curves for different reconstruction distances are shown in **Figure 55.** Each focal length condition produces a distinct axial response with a well-defined peak. The axial response corresponding to f = 9 cm exhibits a pronounced peak at a reconstruction distance closer to the reference plane, indicating the best focus of Object 2 as seen in **Figure 55(a)**. In contrast, the axial response for the optimal FINCH condition f = 10 cm does not exhibit a dominant peak near the reference plane, confirming that Object 2 lies outside the effective FD of FINCH as seen in **Figure 55(b)**. Interestingly, a weaker secondary peak is observed near the reference plane. Some pixels in the selected region still exhibit relatively strong gradients; however, this weaker peak does not yield a visually sharp reconstruction of Object 2, resulting only in a blurred appearance. From **Figure 55(c),** it is observed that the axial response for f = 11 cm peaks far away from the reference plane as compared to the cases of f = 9 cm and f = 10 cm. From the axial characteristic analysis, it is observed that, in the combined SOH obtained in PEAR-FINCH, the f = 9 cm contribution is the main component that covers Object 2, while the additional focal length conditions contribute complementary axial sensitivity that improves continuity of the overall depth range. Hence, in the PEAR-FINCH method, these axial responses collectively yield a SOH with an extended, continuous depth range, enabling successful reconstruction of Object 2 beyond the FD limits of FINCH and DIS.

4.4.2.2 Regular Multiplane DIS

Regular multiplane DIS is a widely used approach to extend the effective FD by simultaneously imaging multiple axial planes. To benchmark this conventional approach against the FINCH and PEAR-FINCH methods, regular multiplane DIS experiments were performed, and the results are shown in **Figure 56**. In this approach, four phase-only diffractive lenses with focal lengths of f = 20 cm, 17 cm, 14 cm, and 12 cm were designed. Each diffractive lens was multiplied by a distinct linear phase function, so that the corresponding OIDs were spatially mapped to separate regions of the image sensor. The multifocal diffractive lens was generated by multiplexing all four resulting functions using two approaches: RM and TAP-GSA. The phase masks obtained using RM and TAP-GSA are shown in Column 1 of **Figure 56**.

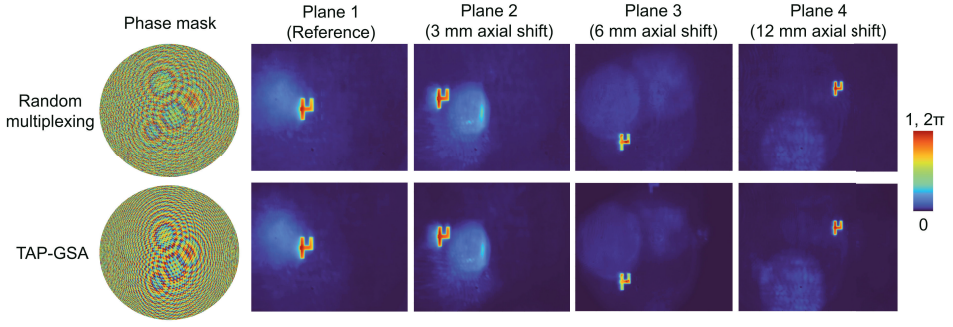

Figure 56. Regular multiplane DIS. Column 1 shows the phase masks of the multifocal lens generated by RM and TAP-GSA. Columns 2–5 show the recorded OIDs corresponding to planes 1–4, respectively. (Adapted from **Publication IV**)

To demonstrate the imaging performance, a test object (digit '4') was sequentially placed at planes 1 to 4. When the object was initially placed at plane 1, the multiplexed phase masks generated using RM and TAP-GSA were displayed on the SLM one after another, and the corresponding OIDs were recorded by the image sensor, as shown in Column 2 of **Figure 56**. For each case, the diffractive lens function in the multiplexed phase mask that matched the object's axial location produced a focused image, whereas the remaining diffractive lens functions produced blurred images. The same process was repeated as the object was shifted to planes 2, 3, and 4, and the corresponding OIDs are shown in Columns 3–5 of **Figure 56**, respectively. These experimental results show that, with regular multiplane DIS, it is only possible to obtain object information that perfectly matches the imaging conditions due to the low FD. Achieving an extended FD comparable to FINCH or PEAR-FINCH would require multiplexing a much larger number of diffractive lenses, which leads to a reduction in SNR. Above all, post-processing will still not be possible with a multiplane lens.

CHAPTER 5:
CONCLUSIONS AND FUTURE PERSPECTIVES

5.1 Summary of the developed research

In conventional imaging systems encompassing both DIS and IIS, the LR-AR parameter space exhibits an inherent one-to-one mapping: for any given LR, there is only one achievable AR. This constraint arises because both LR and AR are fundamentally governed by the imaging system's NA, making independent control of these parameters impossible. Consequently, any attempt to modify AR necessarily alters LR, thereby limiting flexibility in system design and performance. A deeper analysis reveals that this limitation is rooted in the restriction to conventional imaging elements, primarily lenses, which enforce a point-to-point mapping between object and image. While alternative optical fields such as Bessel or Airy beams exhibit propagation-invariant characteristics that can, in principle, reduce AR, they do not map an object point to a point in the image plane but instead to an extended transverse intensity distribution. Attempts to employ such beams within DIS configurations have therefore resulted in degraded LR, effectively shifting the system to a different point in the LR-AR parameter space rather than enabling independent control.
In IIS, however, the optical response of each object point is not directly mapped to an image point but is encoded into an intensity distribution that is subsequently reconstructed computationally. This indirect mapping creates opportunities that have not been fully exploited in prior literature, particularly under spatially incoherent illumination. In earlier works on I-COACH and related methods [77–79], it was demonstrated that this framework introduces a secondary, flexible bottleneck in addition to the NA constraint. As a result, a one-to-many mapping between LR and AR becomes possible within the same NA.

Within the I-COACH and CI frameworks, LR and AR are governed by the lateral and axial correlation lengths, respectively. The above relations enable the use of structured optical fields that do not satisfy conventional imaging requirements. Through indirect mapping, the undesirable transverse intensity distribution of such beams is computationally transformed into a point-like reconstruction, while their propagation characteristics are transferred to the axial response. Prior studies demonstrated that employing ensembles of propagation-invariant beams could access multiple points in the LR-AR parameter space. However, these approaches were limited to real-time optical control and did not permit post-recording modification of imaging characteristics [75,77–79]. These prior works established the foundational principle for this thesis. The central contribution of this doctoral research is the extension of this concept into the post-recording domain: namely, the development of CI frameworks that enable access to multiple points in the LR-AR parameter space *after* data acquisition. It is important to distinguish this capability from conventional post-processing (e.g., denoising), which does not alter the fundamental imaging characteristics. In contrast, this thesis demonstrates that it is possible to modify the intrinsic LR-AR relationship

itself after recording, an ability that has not been previously reported. This advance is enabled by exploiting a fundamental property of spatially incoherent imaging: the independence of object-point contributions. In contrast to CDH, where both mutual and self-interference couple the contributions of different object points, and DIS, where the image is fixed at acquisition, IIS allows linear superposition of independent PSFs. Building on this, the thesis introduces a computational framework in which both PSFs and OIDs are synthesized post-recording through controlled superposition.

Conceptually, this can be interpreted as the realization of a physically inaccessible imaging regime. While the optical system operates under spatially incoherent but temporally coherent conditions, the computational framework effectively introduces an additional degree of incoherence by enabling intensity-level superposition of responses originating from the same object point under different system configurations. This "synthetic incoherence" allows the system to access regions of the LR-AR parameter space that are not reachable through optical means alone. The implementation of this concept relies on constructing and using a multidimensional PSF library, comprising 2D intensity responses across depth, wavelength, and beam type. By performing controlled superposition of PSFs and corresponding OIDs, the effective imaging model is engineered post-acquisition. Based on this principle, the thesis developed three CI frameworks:

- **INCHIS**: Two implementations are presented. In INCHIS-H1, a hybrid optical configuration employing a lens and an axicon generates spherical and Bessel beam responses, respectively. In INCHIS-H2, these responses are combined post-recording with variable weights, enabling continuous tuning of AR independent of LR within the bounds defined by the constituent beams.
- **PEGASASS**: This framework utilizes ensembles of Airy beams with varying 3D propagation trajectories. By synthesizing responses via ensemble combination, PEGASASS enables control over the axial correlation length while preserving the lateral correlation length. In addition to AR tuning, it demonstrates SR tuning, including operation with monochrome sensors through computational channel synthesis.
- **PEAR-FINCH**: Within IDH, multiple FINCH holograms are recorded under different self-interference configurations. The post-recording combination of these holograms enables a significant extension of FD, up to five times that of conventional FINCH, without degrading LR.

A key enabler for these frameworks is the practical realization of multifunctional CPMs. Since combining multiple phase functions generally results in complex-valued functions that are not directly implementable, the thesis first introduces:

- **TAP-GSA**: It encodes amplitude information into phase-only masks, enabling efficient realization of multifunctional DOEs. Experimental validation in FINCH demonstrates improved light efficiency and reduced reconstruction noise, establishing TAP-GSA as a foundational tool for subsequent developments.

Collectively, these contributions establish a new paradigm in CI, wherein imaging characteristics are no longer fixed at the point of acquisition but can be engineered post-recording through controlled synthesis of system responses. By leveraging spatial incoherence and indirect imaging, the thesis demonstrates, for the first time, that AR can be tuned independently of LR after recording, effectively transforming IIS into adaptive and reconfigurable imaging platforms.

5.2 Challenges in the developed research

Although the methods developed in this thesis demonstrate promising capabilities for enabling post-recording control of imaging characteristics, some challenges remain that should be considered for practical implementations and future developments.

5.2.1 Challenges in TAP-GSA

One of the challenges associated with the TAP-GSA is its dependence on the specific optical configuration used in the imaging system. The simulation results and conclusions presented in this work are valid for the specific configuration used in the design and evaluation of the phase masks. When the optical configuration is modified, for example, by changing parameters such as propagation distance, aperture size, wavelength, or pixel size, variations in the performance of the algorithm can be observed. In particular, the optimal DoF value used in the TAP-GSA optimization process may vary with these system parameters. When the DoF approaches 100%, the resulting pure phase mask becomes random-like, introducing light scattering. Conversely, when the DoF is too small, the pure-phase condition is not sufficiently achieved, leading to increased reconstruction noise. Therefore, a trade-off exists between maintaining the pure-phase condition and avoiding excessive random scattering in the phase mask design. As a result, the TAP-GSA must be optimized for the exact experimental conditions and optical configuration of the imaging system to achieve optimal performance. In this thesis, TAP-GSA was primarily implemented and validated within the FINCH framework, as it was developed as a prerequisite method for designing multi-functional phase-only masks, which are needed to develop CI methods for engineering image resolutions. However, the applicability of TAP-GSA to designing phase masks is not limited to systems such as FINCH. Recently, TAP-GSA has also been employed for phase mask design in an I-COACH system based on vortex speckles [104]. Furthermore, TAP-GSA was used to design a multifocal lens by combining multiple phase functions corresponding to different focal lengths for regular multiplane DIS, enabling simultaneous imaging of different planes, as presented in Section 4.4.2.2. These implementations demonstrate that TAP-GSA is a general and flexible framework for designing multifunctional DOEs or CPMs in a variety of CI architectures.

5.2.2 Challenges in INCHIS

One of the challenges observed in the INCHIS framework arises in the INCHIS-H1 method during the implementation of hybrid CPMs. Ideally, as the CPM is tuned from a lens to an axicon, the focal depth is expected to increase, resulting in a systematic reduction in AR. While this trend is generally observed, certain anomalous axial regions occur where the axial behaviour deviates from the expected trend, especially when binary CPMs are used, primarily due to the presence of higher diffraction orders. Addressing these anomalous axial regions requires further investigation in future studies. In addition, experimental implementations may require adjustments to the weighting parameters used to combine the recorded intensity distributions to compensate for variations in exposure time and illumination conditions. Furthermore, in the INCHIS-H2 configuration, the ability to tune AR after recording requires acquiring two images or videos rather than one. Although this introduces a modest reduction in TR, the penalty remains relatively small when compared with many inline holographic imaging techniques that typically require multiple camera shots. These aspects should be considered when designing hybrid CPMs and selecting system parameters for practical implementations. Nevertheless, INCHIS provides a novel framework for post-recording tuning AR without affecting LR, which represents a significant advancement in IIS.

5.2.3 Challenges in PEGASASS

One of the challenges associated with the PEGASASS is the reduction in TR due to the requirement of multiple camera recordings. This arises because several CPMs are used to generate different Airy beams with unique 3D propagation paths, and the corresponding intensity distributions must be recorded separately. As a result, the acquisition time increases compared with single-shot imaging methods. However, considering its 4D imaging capability, this penalty is relatively modest when compared with many IDH techniques, which typically require multiple camera shots. Beyond these challenges, PEGASASS introduces a new approach for achieving multidimensional flexibility in CI systems.

5.2.4 Challenges in PEAR-FINCH

One of the challenges associated with the PEAR-FINCH is the need to record multiple holograms at different focal lengths. Compared with conventional FINCH, this increases acquisition time and data volume, thereby reducing TR. In addition, the reconstruction process involves a two-step procedure: numerical back-propagation followed by deconvolution, which introduces additional computational overhead. Another consideration arises in synthetic hologram generation, where contributions from different focal length conditions may produce a mixture of sharp and blurred components, resulting in low SNR in the reconstructed image. The LRRA effectively suppresses much of this noise for standard test

objects. For continuously structurally varying complex objects, there will be a stronger mixture of sharp and blurred components in the synthetic hologram across different focal length conditions, and the back-propagated reconstruction will exhibit higher noise. This behaviour is expected given the complex nature of the objects. Although LRRA reduces these noise components considerably, it may not eliminate them entirely in highly complex scenes. Therefore, a trade-off exists between object complexity and the level of reconstruction noise introduced during hologram synthesis, which should be considered when applying PEAR-FINCH to real-world objects. Despite these challenges, PEAR-FINCH's ability to engineer the FD entirely after recording provides greater flexibility than conventional imaging approaches.

5.3 Applications of the developed research

The imaging frameworks developed in this thesis have strong potential for applications across several scientific and technological fields. The TAP-GSA provides a versatile computational tool for designing multifunctional DOEs and CPMs, applicable to beam shaping, microscopy, augmented and virtual reality displays, and advanced CI systems. The INCHIS framework, which enables independent tuning of AR without affecting LR, can be particularly useful in microscopy, cinematography, smartphone imaging, computer vision, and motion imaging, where different depth-discrimination characteristics may be required for analysis. The PEGASASS method, which enables post-recording tuning of both AR and SR, has potential applications in multidimensional imaging, remote sensing, biomedical imaging, and chemical analysis, where both AR and SR play critical roles. Finally, the PEAR-FINCH method, which enables post-recording engineering of the FD, may be beneficial for applications requiring extended-FD imaging, such as microscopy, fluorescence imaging, biomedical diagnostics, and holographic imaging of thick samples. Translating these methods into practical imaging devices and evaluating their performance in real-world applications will be an important step toward realizing their full potential.

5.4 Future perspectives of the developed research

The research presented in this thesis opens several promising directions for future work. One important direction involves reducing the number of required camera recordings in the developed methods. Enabling single-shot implementations of techniques such as PEGASASS and PEAR-FINCH would improve TR and enable their application to dynamic scenes. Another promising direction is the integration of advanced reconstruction algorithms, including machine-learning-based approaches, to further improve reconstruction performance. One promising direction for future research is the automation of the proposed CI frameworks. In current implementations, several parameters, such as the relative weights of hybrid components in INCHIS, the number and strengths of Airy beams in

PEGASASS, and the selection of focal length combinations in PEAR-FINCH, are manually determined based on imaging requirements. Automating these processes could significantly improve the usability and efficiency of the CI system, particularly in applications requiring faster analysis. Further work is also needed to extend the proposed techniques to complex real-world scenes. While the methods were validated using standard test objects, additional studies are required to evaluate their performance in practical imaging scenarios. Overall, the research developments presented in this thesis provide a strong foundation for future advancements toward fully flexible and adaptive CI systems, enabling post-recording control of imaging characteristics and expanding the capabilities of next-generation imaging technologies.

RESEARCH HIGHLIGHTS

The research work presented in this thesis has received significant recognition through intellectual property contributions, international conference presentations, international media coverage, research dissemination activities, and outreach efforts. The key highlights are summarized below:

Intellectual Property

Publication II (INCHIS) led to the filing of a *U.S. provisional patent* application through the University of Tartu. The patent reflects the novelty and potential applicability of the developed hybrid imaging approach, enabling flexible post-recording control of imaging resolutions.

> V. Anand, **S. Gopinath**, and A. S. John Francis Rajeswary, "Incoherent hybrid imaging systems," U.S. Patent Application No. 19/098,373, (2025). https://patents.google.com/patent/US20250317543A1/en

Media Coverage and Research Visibility

Publication II (INCHIS), Publication III (PEGASASS), and Publication IV (PEAR-FINCH) have received wide visibility across international scientific news platforms and media outlets:

Interviews and Features

The author had the opportunity to participate in two interviews with ERR Novaator (Estonian National News Broadcasting) to promote the research works INCHIS and PEGASASS. The interviews are available as articles:

- INCHIS – [https://novaator.err.ee/1609141678/tartu-optikute-uus-pildistusmeetod-roomustab-nii-arste-kui-ka-piltnikke]
- PEGASASS – [https://news.err.ee/1609496284/tartu-university-researchers-make-imaging-technology-breakthrough]

International Featured Coverage

Publication II (INCHIS) is also featured in:

- Phys.org – [https://phys.org/news/2023-09-holographic-hybridization-technique-depth-field.html]
- IEEE Spectrum – [https://spectrum.ieee.org/depth-of-field]

International Conference Presentations and Talks

The author disseminated the research work presented in this thesis through several international conferences, invited talks, and academic events.

International Conference Presentations

- SPIE Holography: Advances and Modern Trends VIII, Prague, Czech Republic, 24–28 April 2023 (Oral presentation – Results of Publication I).
- SPIE International Conference on Optical and Photonic Engineering (icOPEN), Singapore, 27 November – 1 December 2023 (Oral presentation – Results of Publication II).
- IEEE International Conference on Next Generation Electronics (NEleX), Tamil Nadu, India, 14–16 December 2023 (Oral Presentation – Preliminary results Publication III). The author received the Best Paper Award.

Summer School Presentation

- 22nd Estonian Summer School on Computer and Systems Science (ESSCaSS), University of Tartu, Estonia, 18–21 August 2025 (Poster presentation – Results of Publication I).

Invited Talks

The author received prestigious invitations to speak at the following international conferences and academic events. At these events, the author presented the results of Publications I, II, and III.

- 1st International Conference on Emerging Trends in Optical Technologies (ETOT-I), Andhra Pradesh, India, 2–4 January 2025.
- 8th International Conference on Machine Vision and Applications (ICMVA), Melbourne, Australia, 12–14 June 2025.
- Laser Research Center, Vilnius University, Lithuania, 12 April 2024.

Research Dissemination and Outreach

Research briefings of Publication I (TAP-GSA), Publication II (INCHIS), and Publication III (PEGASASS) were prepared and presented by the author as part of science communication and outreach activities. These research briefings were recorded and published on the ERA CIPHR LAB YouTube channel:

- TAP-GSA – [https://www.youtube.com/watch?v=r99UGMCxwkk]
- INCHIS – [https://www.youtube.com/watch?v=aDi6WrK34hs]
- PEGASASS – [https://www.youtube.com/watch?v=bA08Bjziy4s]

The INCHIS work was also presented by the author to a broader audience through the following activities:

- Three-Minute Thesis Competition, University of Tartu Library, 28 September 2023 – [https://uttv.ee/naita?id=34804&keel=eng]
- Training Camp: "The Art of Giving a Popular Science Talk", Voore, Estonia, 10 May 2024.

These efforts improved the visibility and accessibility of the research.

Impact and Global Recognition of PEAR-FINCH

Following the publication of the PEAR-FINCH work, the research gained significant international attention and was widely covered by major scientific news platforms. The author sincerely acknowledges the support of the Marketing and Communication Office team from the University of Tartu and the Institute of Physics faculty for promoting and disseminating this research.

The work was featured on the following news platforms:

- Research in Estonia – https://researchinestonia.eu/2026/04/06/3d-images-five-times-clearer/
- ERR Novaator – [https://news.err.ee/1609932482/new-method-by-university-of-tartu-scientists-turns-foggy-holograms-into-a-clear-image]
- University of Tartu News – https://fi.ut.ee/en/news/pear-finch-new-breakthrough-3d-holographic-imaging
- EurekAlert – [https://www.eurekalert.org/news-releases/1116566]
- Phys.org – [https://phys.org/news/2026-02-hologram-method-boosts-3d-image.html]
- ScienceBlog – [https://scienceblog.com/a-computational-trick-lets-scientists-refocus-holograms-after-they-have-already-been-recorded/]
- Bioengineer.org – [https://bioengineer.org/new-technique-boosts-3d-object-image-quality-by-five-times/]
- Scienmag – [https://scienmag.com/new-technique-boosts-3d-object-image-quality-by-five-times/]
- Mirage News – [https://www.miragenews.com/new-method-boosts-3d-image-quality-fivefold-1619699/]
- Wiley Analytical Science – [https://analyticalscience.wiley.com/content/news-do/physicists-achieve-fivefold-expansion-focus-3d-holography]

Scientific Impact and Citations

The developed works have gained notable attention within the research community to date: Publication I (TAP-GSA) – 26 citations; Publication II (INCHIS) – 18 citations; Publication III (PEGASASS) – 11 citations; Publication IV (PEAR-FINCH) – 2 citations (published on January 29, 2026). Despite its recent publication, the PEAR-FINCH work has already received significant attention, with 876 article downloads within two months, indicating strong early impact and interest from the scientific community.

Summary of Impact

These highlights demonstrate that the research contributions presented in this thesis have not only advanced the field of CI but have also gained recognition beyond the academic community through patents, international conferences, media coverage, and outreach activities. This reflects the broader relevance and potential impact of the developed CI frameworks.

KOKKUVÕTE (EESTI KEELES)

Täiustatud mitmemõõtmelised mittekoherentsed kujutamissüsteemid ümberseadistatava aksiaalse ja spektraalse lahutusvõimega

Tavapärastes kujutamissüsteemides, mis hõlmavad nii DIS- kui ka IIS-süsteeme, esineb LR-AR parameetrite ruumis loomupärane üks-ühele vastavus: iga antud LR-i jaoks on olemas ainult üks saavutatav AR. See piirang tuleneb asjaolust, et nii LR kui ka AR on põhimõtteliselt määratud kujutamissüsteemi numbrilise apertuuri (NA) poolt, mistõttu nende parameetrite sõltumatu juhtimine ei ole võimalik. Seetõttu muudab iga katse AR-i muuta paratamatult ka LR-i, mis piirab süsteemi disaini ja toimivuse paindlikkust. Sügavam analüüs näitab, et see piirang tuleneb tavapäraste kujutamiselementide, eeskätt läätsede kasutamisest, mis kehtestavad objekti ja kujutise vahel punktist-punkti vastavuse. Kuigi alternatiivsed optilised väljad, nagu Besseli- või Airy-kiired, omavad levimis-invariantseid omadusi, mis võivad põhimõtteliselt vähendada AR-i, ei kujuta need objekti punkti kujutistasandil punktina, vaid laiendatud ristlõikelise intensiivsusjaotusena. Katsed selliseid kiiri kasutada DIS-konfiguratsioonides on seetõttu viinud LR-i halvenemiseni, nihutades süsteemi LR-AR parameetrite ruumis teise punkti, mitte võimaldades nende sõltumatut juhtimist. IIS-süsteemides ei kaardistata aga iga objekti punkti optilist vastust otse kujutise punktiks, vaid see kodeeritakse intensiivsusjaotusse, mis rekonstrueeritakse hiljem arvutuslikult. Selline kaudne kaardistus loob võimalusi, mida varasem kirjandus ei ole täielikult ära kasutanud, eriti ruumiliselt mittekoherentse valgustuse korral. Varasemates töödes I-COACH ja sellega seotud meetodite kohta [77–79] näidati, et see lähenemine tekitab lisaks NA põhisele esmasele piirangule teise, paindliku kitsaskoha. Selle tulemusena muutub võimalikuks LR-i ja AR-i üks-mitmele vastavus sama NA piires.

I-COACH ja CI raamistikus määravad LR-i ja AR-i vastavalt lateraalse ja aksiaalse korrelatsioonipikkuse abil. Ülaltoodud seosed võimaldavad kasutada struktureeritud optilisi välju, mis ei vasta tavapärastele kujutamisnõuetele. Kaudse kaardistamise abil muudetakse selliste kiirte ebasoovitav ristlõikeline intensiivsusjaotus arvutuslikult punktitaoliseks rekonstruktsiooniks, samas kui nende levimisomadused kantakse üle aksiaalsele vastusele. Varasemad uuringud näitasid, et levimis-invariantsete kiirte ansamblite kasutamisel on võimalik ligipääs mitmele punktile LR-AR parameetrite ruumis. Need lähenemised piirdusid siiski reaalajas optilise juhtimisega ega võimaldanud kujutamisomaduste muutmist pärast salvestamist [75, 77–79]. Need varasemad tööd lõid käesoleva doktoritöö aluspõhimõtte. Selle töö keskne panus seisneb selle kontseptsiooni laiendamises salvestusjärgsesse domeeni: nimelt CI-raamistike arendamises, mis võimaldavad ligipääsu mitmele punktile LR-AR parameetrite ruumis pärast andmete omandamist. Oluline on eristada seda võimekust tavapärasest järeltöötlusest (nt müra vähendamine), mis ei muuda kujutamise põhiomadusi. Seevastu näitab käesolev töö, et on võimalik muuta LR-AR seost ennast pärast salvestamist, mis ei ole varem kirjanduses kajastatud. See edasiminek on võimalik tänu ruumiliselt mitte-

koherentse kujutamise põhiomadusele: objekti punktide panuste sõltumatusele. Erinevalt CDH-st, kus nii vastastikune kui ka eneseinterferents seob erinevate objektipunktide panuseid, ning DIS-ist, kus kujutis on fikseeritud salvestamise hetkel, võimaldab IIS sõltumatute PSF-ide lineaarset superpositsiooni. Sellele tuginedes tutvustab käesolev töö arvutuslikku raamistikku, milles nii PSF-id kui ka OID-d sünteesitakse pärast salvestamist kontrollitud superpositsiooni abil.

Kontseptuaalselt võib seda tõlgendada füüsiliselt kättesaamatu kujutamisrežiimi realiseerimisena. Kuigi optiline süsteem töötab ruumiliselt mittekoherentse, kuid ajaliselt sidusa valguse tingimustes, lisab arvutuslik raamistik efektiivselt täiendava mittesidususe astme, võimaldades sama objekti punkti erinevate süsteemikonfiguratsioonide korral tekkinud vastuste intensiivsustasemel superpositsiooni. See „sünteetiline mittesidusus“ võimaldab süsteemil pääseda LR-AR parameetrite ruumi piirkondadesse, mis ei ole pelgalt optiliste vahenditega saavutatavad. Selle kontseptsiooni realiseerimine põhineb mitmemõõtmelise PSF-teegi loomisel ja kasutamisel, mis sisaldab 2D intensiivsusvastuseid sügavuse, lainepikkuse ja kiire tüübi lõikes. PSF-ide ja vastavate OID-de kontrollitud superpositsiooni abil kujundatakse efektiivne kujutamismudel pärast andmete omandamist. Selle põhimõtte alusel arendab töö välja kolm peamist CI-raamistikku:

- **INCHIS:** Esitatakse kaks teostust. INCHIS-H1-s genereerib hübriidne optiline konfiguratsioon, mis kasutab läätse ja aksikoni, vastavalt sfääriliste ja Besseli kiirte vastuseid. INCHIS-H2-s kombineeritakse need vastused pärast salvestamist muutuva kaaluga, võimaldades AR-i pidevat reguleerimist LR-ist sõltumatult nende kiirte poolt määratud piirides.
- **PEGASASS:** See raamistik kasutab erinevate 3D levimistrajektooridega Airy kiirte ansambleid. Ansambli kombinatsiooni kaudu vastuseid sünteesides võimaldab PEGASASS kontrollida aksiaalset korrelatsioonipikkust, säilitades samal ajal lateraalse korrelatsioonipikkuse. Lisaks AR-i reguleerimisele demonstreeritakse ka SR-i reguleerimist, sealhulgas tööd monokroomsete sensoritega arvutusliku kanalite sünteesi abil.
- **PEAR-FINCH:** IDH raamistikus salvestatakse mitu FINCH hologrammi erinevate eneseinterferentsi konfiguratsioonidega. Nende hologrammide salvestusjärgne kombineerimine võimaldab FD märkimisväärset laiendamist, kuni viis korda võrreldes tavapärase FINCH-iga, ilma LR-i halvenemiseta.

Nende raamistike oluline võimaldaja on multifunktsionaalsete CPM-ide praktiline realiseerimine. Kuna mitme faasifunktsiooni kombineerimine viib üldjuhul kompleksväärtuslike funktsioonideni, mida ei saa otseselt realiseerida, tutvustab töö esmalt:

- **TAP-GSA:** See kodeerib amplituuditeabe faasipõhistesse maskidesse, võimaldades multifunktsionaalsete DOE-de tõhusat realiseerimist. Eksperimentaalne valideerimine FINCH-süsteemis näitab paranenud valgusefektiivsust ja vähenenud rekonstrueerimismüra, kinnitades TAP-GSA rolli edasiste arenduste aluseks.

Kokkuvõttes loovad need panused uue paradigma CI-s, kus kujutamisomadused ei ole enam fikseeritud andmete omandamise hetkel, vaid neid saab kujundada pärast salvestamist süsteemivastuste kontrollitud sünteesi abil. Kasutades ruumilist mittekoherentsust ja kaudset kujutamist, näitab töö esmakordselt, et AR-i on võimalik reguleerida LR-ist sõltumatult pärast salvestamist, muutes IIS-süsteemid kohandatavateks ja ümberseadistatavateks kujutamisplatvormideks.

ACKNOWLEDGEMENTS

First and foremost, I express my sincere gratitude to my supervisor, Prof. Vijaykumar Anand, for giving me the opportunity to pursue my PhD under his guidance. He was also one of my advisors for my Master's thesis at Thiagarajar College in India, conducted in collaboration with the University of Tartu. Coming from a background with limited research experience and exposure to team-based research, I found the initial phase of my PhD quite challenging. However, his invaluable guidance, continuous support in all possible ways, and insightful discussions since the very beginning have helped me gradually adapt and grow. His encouragement and expertise have played a crucial role in shaping my PhD research and my development as a researcher. I am also deeply thankful for the opportunities to work on various projects in our group and to participate in international conferences and competitions, which have significantly enriched my academic and research journey.

I express my sincere gratitude to all my mentors and professors at Thiagarajar College, India, especially my Head of the Department, Prof. N. Srinivasan, Student Welfare Dean, Prof. R. Srinivasan, my other Master's thesis advisor, Prof. R. Dhanalakshmi, and Mr. R. Rajesh, Training and Placement Officer for their support and guidance during my Master's studies, and also helping to lay the foundation for my PhD journey.

I express my sincere thanks to Prof. Joseph Rosen, who is like an external supervisor from Ben-Gurion University, Israel, for his invaluable guidance, constructive feedback, and support throughout my PhD projects. I am also grateful to Prof. Aile Tamm and Prof. Kaupo Kukli from the University of Tartu for their valuable suggestions and for providing access to the fabrication of optical elements in their Thin Films Laboratory. I would also like to thank Prof. Indrek Jogi, Prof. Kalev Tarkpea, Prof. Kaido Reivelt, and Prof. Rainer Parna from our Institute of Physics for their guidance and support during my PhD studies. I would also like to extend my thanks to Prof. Saulius Juodkazis at Swinburne University of Technology, Australia, and Prof. Ravi Kumar at SRM University AP, India, for their support.

I am grateful to my co-authors for their collaboration and contributions to the research work presented in this thesis. I would also like to acknowledge the members of the CIPHR project for their support, teamwork, and stimulating discussions, which significantly contributed to this work. I would like to thank Dr. Praveen Periyasamy, who supported me during the early stage of my research career and helped me with my first training project. I am also thankful to Dr. Amudhavel Jayavel and Dr. Viktor Palm for their guidance and support, and to Dr. Vipin Tiwari for his valuable discussions and assistance during the later stage of my PhD.

I thank my fellow CIPHR team colleagues and friends, Francis Gracy, Andrei Bleahu, Agnes Pristy, Narmada Joshi, Eulalia Puig, Tauno Kahro, Oskar Tamm, and Otto Maasik for their support and technical assistance, and for creating a

positive and collaborative research environment. I am also thankful to our research manager, Aravind Simon, and project manager, Tiia Lillemaa, for their continuous support throughout my PhD journey. I am especially grateful for their help when I first arrived in Tartu, making my transition and settlement smooth and comfortable, as well as for their assistance with conference travel arrangements.

I gratefully acknowledge the Institute of Physics, University of Tartu, for providing the necessary facilities and infrastructure to carry out this research. I also acknowledge the financial support provided by the CIPHR project throughout my PhD journey. I am thankful to the University of Tartu Library for partially covering the article processing charges for the open access publication of my final PhD work. I also acknowledge the Estonian Doctoral School Mobility Grant for supporting my conference visit to Melbourne, Australia, and the Erasmus Blended Mobility program for supporting my summer school visit to Finland. Furthermore, I would like to thank the Estonian National Government for their financial support throughout my entire PhD journey.

I express my deepest gratitude to my parents and family members, and relatives for allowing me to step out of my comfort zone and pursue my PhD abroad. Their unconditional love, patience, and constant support have been my greatest strength throughout my PhD studies. I thank my school and college friends for their encouragement and support throughout this journey. I am deeply grateful to my girlfriend, Vidyasri, for being my constant support and strength. Despite the long distance, her encouragement and understanding have helped me navigate both the highs and lows of this journey.

I would like to thank the Estonian people, who were very kind and helpful. I also thank my friend Srirathi and other friends in Tartu, as well as colleagues and friends from the Institute of Physics and other departments of the University of Tartu, for providing such an inspiring and supportive academic environment. Finally, I thank Almighty God for guiding me throughout this journey. To be honest, I had never heard of Estonia before my Master's studies. After completing my Master's degree, everything unfolded unexpectedly, and I consider it a blessing that brought me to this wonderful place. The kindness, support, and helpful nature of the people here made my journey even more meaningful. Studying and growing in this environment has truly been a privilege.

REFERENCES

1. J. Rosen, A. Vijayakumar, M. Kumar, M. R. Rai, *et al*., "Recent advances in self-interference incoherent digital holography," Adv. Opt. Photonics **11**, 1–66 (2019). https://doi.org/10.1364/AOP.11.000001
2. T. S. Huang, "Digital holography," Proc. IEEE **59**, 1335–1346 (1971). https://doi.org/10.1109/PROC.1971.8408
3. T. C. Poon and J. P. Liu, *Introduction to Modern Digital Holography: With MATLAB* (Cambridge University Press, 2014).
4. T. Tahara, X. Quan, R. Otani, Y. Takaki, and O. Matoba, "Digital holography and its multidimensional imaging applications: a review," Microscopy **67**, 55–67 (2018). https://doi.org/10.1093/jmicro/dfy007
5. B. Javidi, A. Carnicer, A. Anand, G. Barbastathis, *et al*., "Roadmap on digital holography," Opt. Express **29**, 35078–35118 (2021). https://doi.org/10.1364/OE.435915
6. W. Osten, A. Faridian, P. Gao, K. Korner, *et al*., "Recent advances in digital holography [Invited]," Appl. Opt. **53**, G44–G63 (2014). https://doi.org/10.1364/AO.53.000G44
7. T. C. Poon, "Optical Scanning Holography - A Review of Recent Progress," J. Opt. Soc. Korea **13**, 406–415 (2009). https://doi.org/10.3807/JOSK.2009.13.4.406
8. J. P. Liu, T. Tahara, Y. Hayasaki, and T. C. Poon, "Incoherent Digital Holography: A Review," Appl. Sci. **8**, 143 (2018). https://doi.org/10.3390/app8010143
9. T. Tahara, Y. Zhang, J. Rosen, V. Anand, *et al*., "Roadmap of incoherent digital holography," Appl. Phys. B **128**, 193 (2022). https://doi.org/10.1007/s00340-022-07911-x
10. J. Rosen, S. Alford, B. Allan, V. Anand, *et al*., "Roadmap on computational methods in optical imaging and holography [Invited]," Appl. Phys. B **130**, 166 (2024). https://doi.org/10.1007/s00340-024-08280-3
11. J. G. Ables, "Fourier transform photography: a new method for X-ray astronomy," Proc. Astron. Soc. Aust. **1**, 172–173 (1968). https://doi.org/10.1017/S1323358000011292
12. R. H. Dicke, "Scatter-hole cameras for x-rays and gamma rays," Astrophys. J. **153**, L101 (1968).
13. T. M. Cannon and E. E. Fenimore, "Coded aperture imaging: many holes make light work," Opt. Eng. **19**, 193283 (1980). https://doi.org/10.1117/12.7972511
14. M. J. Cieślak, K. A. Gamage, and R. Glover, "Coded-aperture imaging systems: Past, present and future development – A review," Radiat. Meas. **92**, 59–71 (2016). https://doi.org/10.1016/j.radmeas.2016.08.002
15. V. Tiwari, S. Gopinath, T. Kahro, *et al*., "Recent advances in spatially incoherent coded aperture imaging technologies," Technologies **13**, 210 (2025). https://doi.org/10.3390/technologies13050210
16. J. L. Horner and P. D. Gianino, "Phase-only matched filtering," Appl. Opt. **23**, 812–816 (1984). https://doi.org/10.1364/AO.23.000812
17. E. E. Fenimore and T. M. Cannon, "Coded aperture imaging with uniformly redundant arrays," Appl. Opt. **17**, 337–347 (1978). https://doi.org/10.1364/AO.17.000337
18. S. R. Gottesman and E. E. Fenimore, "New family of binary arrays for coded aperture imaging," Appl. Opt. **28**, 4344–4352 (1989). https://doi.org/10.1364/AO.28.004344
19. H. H. Barrett and F. A. Horrigan, "Fresnel Zone Plate Imaging of Gamma Rays: Theory," Appl. Opt. **12**, 2686–2699 (1973). https://doi.org/10.1364/AO.12.002686

20. M. E. Gehm, R. John, D. J. Brady, R. M. Willett, and T. J. Schulz, "Single-shot compressive spectral imaging with a dual-disperser architecture," Opt. Express **15**, 14013–14027 (2007). https://doi.org/10.1364/OE.15.014013
21. T. H. Tsai and D. J. Brady, "Coded aperture snapshot spectral polarization imaging," Appl. Opt. **52**, 2153–2161 (2013). https://doi.org/10.1364/AO.52.002153
22. H. H. Barrett and K. J. Myers, *Foundations of Image Science* (Wiley, 2004).
23. O. Flasseur, C. Fournier, N. Verrier, L. Denis, *et al*., "Self-calibration for lensless color microscopy," Appl. Opt. **56**, F189–F199 (2017). https://doi.org/10.1364/AO.56.00F189
24. O. Faix, "Fourier transform infrared spectroscopy," in *Methods in Lignin Chemistry* (Springer, Berlin, Heidelberg, 1992), pp. 83–109. https://doi.org/10.1007/978-3-642-74065-7_7
25. S. H. Kong, D. D. L. Wijngaards, and R. F. Wolffenbuttel, "Infrared micro-spectrometer based on a diffraction grating," Sens. Actuators A: Phys. **92**, 88–95 (2001). https://doi.org/10.1016/S0924-4247(01)00544-1
26. T. G. Etoh, A. Q. Nguyen, Y. Kamakura, K. Shimonomura, *et al*., "The theoretical highest frame rate of Silicon image sensors," Sensors **17**, 483 (2017). https://doi.org/10.3390/s17030483
27. U. Leischner, W. Zieglgänsberger, and H. U. Dodt, "Resolution of ultramicroscopy and field of view analysis," PLoS One **4**, e5785 (2009). https://doi.org/10.1371/journal.pone.0005785
28. D. H. Johnson, "Signal-to-noise ratio," Scholarpedia **1**, 2088 (2006). https://doi.org/10.4249/scholarpedia.2088
29. T. C. Poon, "Scanning holography and two-dimensional image processing by acousto-optic two-pupil synthesis," J. Opt. Soc. Am. A **2**, 521–527 (1985). https://doi.org/10.1364/JOSAA.2.000521
30. V. Anand, T. Tahara, and J. Rosen, "The evolution of incoherent digital holography: A perspective on concepts, technologies, and impact (invited)," Phys. Lett. A **576**, 131443 (2026). https://doi.org/10.1016/j.physleta.2026.131443
31. J. Rosen and G. Brooker, "Digital spatially incoherent Fresnel holography," Opt. Lett. **32**, 912–914 (2007). https://doi.org/10.1364/OL.32.000912
32. J. Rosen, S. Alford, V. Anand, J. Art, *et al*., "Roadmap on Recent Progress in FINCH Technology," J. Imaging **7**, 197 (2021). https://doi.org/10.3390/jimaging7100197
33. J. Rosen, N. Siegel, and G. Brooker, "Theoretical and experimental demonstration of resolution beyond the Rayleigh limit by FINCH fluorescence microscopic imaging," Opt. Express **19**, 26249–26268 (2011). https://doi.org/10.1364/OE.19.026249
34. B. W. Schilling, T. C. Poon, G. Indebetouw, B. Storrie, *et al*., "Three-dimensional holographic fluorescence microscopy," Opt. Lett. **22**, 1506–1508 (1997). https://doi.org/10.1364/OL.22.001506
35. T. C. Poon and G. Indebetouw, "Three-dimensional point spread functions of an optical heterodyne scanning image processor," Appl. Opt. **42**, 1485–1492 (2003). https://doi.org/10.1364/AO.42.001485
36. H. Yu, Y. Kim, D. Yang, W. Seo, *et al*., "Deep learning-based incoherent holographic camera enabling acquisition of real-world holograms for holographic streaming system," Nat. Commun. **14**, 3534 (2023). https://doi.org/10.1038/s41467-023-39329-0

37. J. Rosen and G. Brooker, “Non-scanning motionless fluorescence three-dimensional holographic microscopy,” Nat. Photonics **2**, 190–195 (2008). https://doi.org/10.1038/nphoton.2007.300
38. G. Brooker, N. Siegel, V. Wang, and J. Rosen, “Optimal resolution in Fresnel incoherent correlation holographic fluorescence microscopy,” Opt. Express **19**, 5047–5062 (2011). https://doi.org/10.1364/OE.19.005047
39. K. Choi, J. Yim, S. Yoo, and S. W. Min, “Self-interference digital holography with a geometric-phase hologram lens,” Opt. Lett. **42**, 3940–3943 (2017). https://doi.org/10.1364/OL.42.003940
40. T. Nobukawa, T. Muroi, Y. Katano, N. Kinoshita, and N. Ishii, “Single-shot phase-shifting incoherent digital holography with multiplexed checkerboard phase gratings,” Opt. Lett. **43**, 1698–1701 (2018). https://doi.org/10.1364/OL.43.001698
41. S. Sakamaki, N. Yoneda, and T. Nomura, “Single-shot in-line Fresnel incoherent holography using a dual-focus checkerboard lens,” Appl. Opt. **59**, 6612–6618 (2020). https://doi.org/10.1364/AO.393176
42. T. Tahara, T. Kanno, Y. Arai, and T. Ozawa, “Single-shot phase-shifting incoherent digital holography,” J. Opt. **19**, 065705 (2017). https://doi.org/10.1088/2040-8986/aa6e82
43. H. Wang, X. Han, S. Liu, H. Liu, *et al*., “Dynamic 3D Fresnel incoherent correlation holography imaging based on single-shot mirrored phase-shifting technology,” Opt. Lett. **49**, 5886–5889 (2024). https://doi.org/10.1364/OL.538944
44. R. Kelner, B. Katz, and J. Rosen, “Optical sectioning using a digital Fresnel incoherent-holography-based confocal imaging system,” Optica **1**, 70–74 (2014). https://doi.org/10.1364/OPTICA.1.000070
45. V. Anand and J. Rosen, “Computational optical sectioning in Fresnel incoherent correlation holography,” Sci. Rep. **15**, 45209 (2025). https://doi.org/10.1038/s41598-025-29281-y
46. P. Bouchal and Z. Bouchal, “Selective edge enhancement in three-dimensional vortex imaging with incoherent light,” Opt. Lett. **37**, 2949–2951 (2012). https://doi.org/10.1364/OL.37.002949
47. A. Vijayakumar, Y. Kashter, R. Kelner and J. Rosen, “Coded aperture correlation holography–a new type of incoherent digital holograms,” Opt. Express **24**, 12430–12441 (2016). https://doi.org/10.1364/OE.24.012430
48. A. Vijayakumar, M. Kumar, M. R. Rai, and J. Rosen, “Coded aperture correlation holography system for recording secured digital holograms of incoherently illuminated 3D scenes,” in *Advanced Secure Optical Image Processing for Communications*, vol. 4, (IOP Publishing, Bristol, UK, 2018), pp. 1–19.
49. A. Vijayakumar, T. Katkus, S. Lundgaard, D. Linklater, *et al*., “Fresnel incoherent correlation holography with single camera shot,” Opto-Electron. Adv. **3**, 200004 (2020). https://doi.org/10.29026/oea.2020.200004
50. F. G. Arockiaraj, A. P. Ignatius Xavier, S. Gopinath, A. S. John Francis Rajeswary, *et al*., “Optimizing the temporal and spatial resolutions and light throughput of Fresnel incoherent correlation holography in the framework of coded aperture imaging,” J. Opt. **26**, 035605 (2024). https://doi.org/10.1088/2040-8986/ad2620
51. M. R. Rai, A. Vijayakumar, and J. Rosen, “Non-linear adaptive three-dimensional imaging with interferenceless coded aperture correlation holography (I-COACH),” Opt. Express **26**, 18143–18154 (2018). https://doi.org/10.1364/OE.26.018143

52. A. P. Ignatius Xavier, T. Kahro, S. Gopinath, V. Tiwari, *et al*., "Coded aperture imaging using non-linear Lucy-Richardson algorithm," Opt. Laser Technol. **183**, 112300 (2025). https://doi.org/10.1016/j.optlastec.2024.112300
53. A. Vijayakumar and J. Rosen, "Interferenceless coded aperture correlation holography – a new technique for recording incoherent digital holograms without two-wave interference," Opt. Express **25**, 13883–13896 (2017). https://doi.org/10.1364/OE.25.013883
54. W. H. Richardson, "Bayesian-Based Iterative Method of Image Restoration*," J. Opt. Soc. Am. **62**, 55–59 (1972). https://doi.org/10.1364/JOSA.62.000055
55. L. B. Lucy, "An iterative technique for the rectification of observed distributions," Astron. J. **79**, 745 (1974).
56. V. Anand, M. Han, J. Maksimovic, S. H. Ng, *et al*., "Single-shot mid-infrared incoherent holography using Lucy-Richardson-Rosen algorithm," Opto-Electron Sci. **1**, 210006 (2022). https://doi.org/10.29026/oes.2022.210006
57. A. P. Ignatius Xavier, F. G. Arockiaraj, S. Gopinath, A. S. John Francis Rajeswary, *et al*., "Single-Shot 3D Incoherent Imaging Using Deterministic and Random Optical Fields with Lucy–Richardson–Rosen Algorithm," Photonics **10**, 987 (2023). https://doi.org/10.3390/photonics10090987
58. A. Bleahu, S. Gopinath, T. Kahro, P. Periyasamy Angamuthu, *et al*., "3D incoherent imaging using an ensemble of sparse self-rotating beams," Opt. Express **31**, 26120–26134 (2023). https://doi.org/10.1364/OE.493526
59. H. Vardhan, S. Gopinath, V. Tiwari, A. K. Sivarajan, *et al.*, "Coded aperture imaging with helico-conical beams," Appl. Phys. B **131**, 220 (2025). https://doi.org/10.1007/s00340-025-08585-x
60. V. Anand, "Developing variants of the Lucy–Richardson algorithm for coded aperture imaging: tutorial," J. Opt. Soc. Am. A **42**, 1964–1976 (2025). https://doi.org/10.1364/JOSAA.573587
61. Z. He, H. Wang, Y. Li, Z. Zhang, *et al*., "A deconvolutional reconstruction method based on Lucy – Richardson algorithm for joint scanning laser thermography," IEEE Trans. Instrum. Meas. **70**, 1–8 (2021). https://doi.org/10.1109/TIM.2020.3034967
62. S. A. Hojjatoleslami, M. R. N. Avanaki, and A. Gh. Podoleanu, "Image quality improvement in optical coherence tomography using Lucy – Richardson deconvolution algorithm," Appl. Opt. **52**, 5663–5670 (2013). https://doi.org/10.1364/AO.52.005663
63. D. Smith, S. Gopinath, F. G. Arockiaraj, A. N. K. Reddy, *et al*., "Nonlinear Reconstruction of Images from Patterns Generated by Deterministic or Random Optical Masks—Concepts and Review of Research," J. Imaging **8**, 174 (2022). https://doi.org/10.3390/jimaging8060174
64. A. Jayavel, S. Gopinath, P. Periyasamy Angamuthu, F. G. Arockiaraj, *et al*., "Improved Classification of Blurred Images with Deep-Learning Networks Using Lucy-Richardson-Rosen Algorithm," Photonics **10**, 396 (2023). https://doi.org/10.3390/photonics10040396
65. J. Rosen and V. Anand, "Incoherent nonlinear deconvolution using an iterative algorithm for recovering limited-support images from blurred digital photographs," Opt. Express **32**, 1034–1046 (2024). https://doi.org/10.1364/OE.506475
66. H. Wang, Z. Göröcs, W. Luo, Y. Zhang, *et al*., "Computational out-of-focus imaging increases the space–bandwidth product in lens-based coherent microscopy," Optica **3**, 1422–1429 (2016). https://doi.org/10.1364/OPTICA.3.001422

67. J. Liang and L. V. Wang, “Single-shot ultrafast optical imaging,” Optica **5**, 1113–1127 (2018). https://doi.org/10.1364/OPTICA.5.001113
68. T. Igarashi, M. Naruse, and R. Horisaki, “Incoherent diffractive optical elements for extendable field-of-view imaging,” Opt. Express **31**, 31369–31382 (2023). https://doi.org/10.1364/OE.499866
69. M. R. Rai, A. Vijayakumar, and J. Rosen, “Extending the field of view by a scattering window in an I-COACH system,” Opt. Lett. **43**, 1043–1046 (2018). https://doi.org/10.1364/OL.43.001043
70. M. G. L. Gustafsson, “Surpassing the lateral resolution limit by a factor of two using structured illumination microscopy,” J. Microsc. **198**, 82–87 (2000). https://doi.org/10.1046/j.1365-2818.2000.00710.x
71. S. W. Hell and J. Wichmann, “Breaking the diffraction resolution limit by stimulated emission: stimulated-emission-depletion fluorescence microscopy,” Opt. Lett. **19**, 780–782 (1994). https://doi.org/10.1364/OL.19.000780
72. M. Rust, M. Bates, and X. Zhuang, “Sub-diffraction-limit imaging by stochastic optical reconstruction microscopy (STORM),” Nat. Methods **3**, 793–796 (2006). https://doi.org/10.1038/nmeth929
73. Y. Kashter, A. Vijayakumar, Y. Miyamoto, and J. Rosen, “Enhanced super resolution using Fresnel incoherent correlation holography with structured illumination,” Opt. Lett. **41**, 1558–1561 (2016). https://doi.org/10.1364/OL.41.001558
74. Y. Kashter, A. Vijayakumar, and J. Rosen, “Resolving images by blurring: super-resolution method with a scattering mask between the observed objects and the hologram recorder,” Optica **4**, 932–939 (2017). https://doi.org/10.1364/OPTICA.4.000932
75. A. Vijayakumar, Y. Kashter, R. Kelner and J. Rosen, “Coded aperture correlation holography system with improved performance [Invited],” Appl. Opt. **56**, F67–F77 (2017). https://doi.org/10.1364/AO.56.000F67
76. A. Bulbul, N. Hai, and J. Rosen, “Coded aperture correlation holography (COACH) with a superior lateral resolution of FINCH and axial resolution of conventional direct imaging systems,” Opt. Express **29**, 42106–42118 (2021). https://doi.org/10.1364/OE.446945
77. A. Vijayakumar, “Tuning Axial Resolution Independent of Lateral Resolution in a Computational Imaging System Using Bessel Speckles,” Micromachines **13**, 1347 (2022). https://doi.org/10.3390/mi13081347
78. R. Kumar, V. Anand, and J. Rosen, “3D single shot lensless incoherent optical imaging using coded phase aperture system with point response of scattered airy beams,” Sci. Rep. **13**, 2996 (2023). https://doi.org/10.1038/s41598-023-30183-0
79. M. R. Rai and J. Rosen, “Depth-of-field engineering in coded aperture imaging,” Opt. Express **29**, 1634–1648 (2021). https://doi.org/10.1364/OE.412744
80. T. Nobukawa, Y. Katano, T. Muroi, N. Kinoshita, and N. Ishii, “Bimodal Incoherent Digital Holography for Both Three-Dimensional Imaging and Quasi-Infinite–Depth-of-Field Imaging,” Sci. Rep. **9**, 3363 (2019). https://doi.org/10.1038/s41598-019-39728-8
81. O. Barlev and M. A. Golub, “Multifunctional binary diffractive optical elements for structured light projectors,” Opt. Express **26**, 21092–21107 (2018). https://doi.org/10.1364/OE.26.021092
82. M. Polin, K. Ladavac, S.-H. Lee, Y. Roichman, and D. G. Grier, “Optimized holographic optical traps,” Opt. Express **13**, 5831–5845 (2005). https://doi.org/10.1364/OPEX.13.005831

83. A. Vijayakumar and S. Bhattacharya, "Design of multifunctional diffractive optical elements," Opt. Eng. **54**, 024104 (2015). https://doi.org/10.1117/1.OE.54.2.024104
84. M. Pasienski and B. DeMarco, "A high-accuracy algorithm for designing arbitrary holographic atom traps," Opt. Express **16**, 2176–2190 (2008). https://doi.org/10.1364/OE.16.002176
85. A. Vijayakumar and S. Bhattacharya, "Compact generation of superposed higher-order Bessel beams via composite diffractive optical elements," Opt. Eng. **54**, 111310 (2015). https://doi.org/10.1117/1.OE.54.11.111310
86. Y. Shi, C. Wan, C. Dai, Z. Wang, *et al*., "Augmented reality enabled by on-chip meta-holography multiplexing," Laser Photonics Rev. **16**, 2100638 (2022). https://doi.org/10.1002/lpor.202100638
87. A. Vijayakumar and S. Bhattacharya, "Phase-shifted Fresnel axicon," Opt. Lett. **37**, 1980–1982 (2012). https://doi.org/10.1364/OL.37.001980
88. H. Wang and R. Piestun, "Azimuthal multiplexing 3D diffractive optics," Sci. Rep. **10**, 6438 (2020). https://doi.org/10.1038/s41598-020-63075-8
89. W. Yu, T. Konishi, T. Hamamoto, H. Toyota, *et al*., "Polarization-multiplexed diffractive optical elements fabricated by subwavelength structures," Appl. Opt. **41**, 96–100 (2002). https://doi.org/10.1364/AO.41.000096
90. A. Vijayakumar, C. Rosales-Guzmán, M. R. Rai, J. Rosen, *et al*., "Generation of structured light by multilevel orbital angular momentum holograms," Opt. Express **27**, 6459–6470 (2019). https://doi.org/10.1364/OE.27.006459
91. A. Vijayakumar and S. Bhattacharya, *Design and Fabrication of Diffractive Optical Elements with MATLAB* (SPIE Press, 2017).
92. Z. Kuang, W. Perrie, S. P. Edwardson, E. Fearon, and G. Dearden, "Ultrafast laser parallel microdrilling using multiple annular beams generated by a spatial light modulator," J. Phys. D: Appl. Phys. **47**, 115501 (2014). https://doi.org/10.1088/0022-3727/47/11/115501
93. A. Vijayakumar and S. Bhattacharya, "Quasi-achromatic Fresnel zone lens with ring focus," Appl. Opt. **53**, 1970–1974 (2014). https://doi.org/10.1364/AO.53.001970
94. X.-B. Hu, S.-Y. Ma, and C. Rosales-Guzmán, "High-speed generation of singular beams through random spatial multiplexing," J. Opt. **23**, 044002 (2021). https://doi.org/10.1088/2040-8986/abef22
95. R. W. Gerchberg and W. O. Saxton, "A practical algorithm for the determination of phase from image and diffraction plane pictures," Optik **35**, 227–246 (1972).
96. B. Katz, J. Rosen, R. Kelner, and G. Brooker, "Enhanced resolution and throughput of Fresnel incoherent correlation holography (FINCH) using dual diffractive lenses on a spatial light modulator (SLM)," Opt. Express **20**, 9109–9121 (2012). https://doi.org/10.1364/OE.20.009109
97. D. Smith, S. H. Ng, M. Han, T. Katkus, *et al*., "Imaging with diffractive axicons rapidly milled on sapphire by femtosecond laser ablation," Appl. Phys. B **127**, 154 (2021). https://doi.org/10.1007/s00340-021-07701-x
98. J. Rosen and R. Kelner, "Modified Lagrange invariants and their role in determining transverse and axial imaging resolutions of self-interference incoherent holographic systems," Opt. Express **22**, 29048–29066 (2014). https://doi.org/10.1364/OE.22.029048
99. MATLAB, version 9.13.0 (R2022b), The MathWorks Inc., Natick, Massachusetts, USA (2022). https://www.mathworks.com

100. O. Brzobohatý, T. Čižmár, and P. Zemánek, “High quality quasi-Bessel beam generated by round-tip axicon,” Opt. Express **16**, 12688–12700 (2008). https://doi.org/10.1364/OE.16.012688
101. C. J. Zapata-Rodríguez and A. Sánchez-Losa, “Three-dimensional field distribution in the focal region of low-Fresnel-number axicons,” J. Opt. Soc. Am. A **23**, 3016–3026 (2006). https://doi.org/10.1364/JOSAA.23.003016
102. S. Pertuz, D. Puig, and M. A. Garcia, “Analysis of focus measure operators for shape-from-focus,” Pattern Recognit. **46**, 1415–1432 (2013). https://doi.org/10.1016/j.patcog.2012.11.011
103. W. Piao, Y. Han, L. Hu, and C. Wang, “Quantitative Evaluation of Focus Measure Operators in Optical Microscopy,” Sensors **25**, 3144 (2025). https://doi.org/10.3390/s25103144
104. E. Puig Vilardell, S. Gopinath, V. Tiwari, T. Kahro, *et al*., “Spatio-spectral correlations in interferenceless coded aperture correlation holography with vortex speckles,” Appl. Phys. B **131**, 142 (2025). https://doi.org/10.1007/s00340-025-08507-x

CHAPTER 6:
ATTACHED PUBLICATIONS

CURRICULUM VITAE (IN ENGLISH)

Name: Shivasubramanian Gopinath
Date of Birth: 30 August 1999
Nationality: Indian
Languages: English, Tamil (Native)
Address: Room No. B206, Institute of Physics, W. Ostwaldi 1, 50411 Tartu, Estonia
Mobile Number: +372 55580344, +91 8838116170
E-mail: shivasubramanian.gopinath@ut.ee, gopishiva62@gmail.com

Academic Profile:

Current affiliation: Doctoral student, Junior Research Fellow, and a member of the CIPHR research group, Institute of Physics, University of Tartu, Estonia (2022 – Present)

Research interests: Computational imaging, incoherent digital holography, coded aperture imaging, and diffractive optics

Education:

Master of Science in Physics, Thiagarajar College, India (2020–2022)

Bachelor of Science in Physics, Thiagarajar College, India (2017–2020)

Higher Secondary Education, TVS Higher Secondary School, India (2015–2017)

Secondary Education, TVS Higher Secondary School, India (2010–2015)

Primary Education, TVS Primary School, India (2005–2010)

Publications:

F. G. Arockiaraj, **S. Gopinath**, J. Rosen, and V. Anand, "Invasive imaging through thin scattering layer using special beams with temporal coherence and spatial incoherence," Opt. Laser Technol. **200**, 115130 (2026). https://doi.org/10.1016/j.optlastec.2026.115130

S. Gopinath, J. Rosen, and V. Anand, "Axial resolution post-processing engineering in Fresnel incoherent correlation holography," J. Phys. Photonics **8**, 015041 (2026). https://doi.org/10.1088/2515-7647/ae38ae

P. A. Nair, A. Deshpande, S. S. Kumar, **S. Gopinath**, *et al.*, "Enhancing limited-view photoacoustic vascular images via non-linear Lucy-Richardson deconvolution," Opt. Continuum **4**, 2885–2895 (2025). https://doi.org/10.1364/OPTCON.577884

H. Vardhan, **S. Gopinath**, V. Tiwari, *et al.*, "Coded aperture imaging with helico-conical beams," Appl. Phys. B **131**, 220 (2025). https://doi.org/10.1007/s00340-025-08585-x

E. Puig Vilardell, **S. Gopinath**, V. Tiwari, T. Kahro, *et al.*, "Spatio-spectral correlations in interferenceless coded aperture correlation holography with vortex speckles," Appl. Phys. B **131**, 1–15 (2025). https://doi.org/10.1007/s00340-025-08507-x

V. Tiwari, **S. Gopinath**, T. Kahro, *et al.*, "Recent advances in spatially incoherent coded aperture imaging technologies," Technologies **13**, 210 (2025). https://doi.org/10.3390/technologies13050210

A. P. Ignatius Xavier, T. Kahro, **S. Gopinath**, F. G. Arockiaraj, *et al.*, "Coded aperture imaging using non-linear Lucy-Richardson algorithm," Opt. Laser Technol. **183**, 112300 (2025). https://doi.org/10.1016/j.optlastec.2024.112300

N. Joshi, A. P. Ignatius Xavier, **S. Gopinath**, V. Tiwari, and V. Anand, "Spatial ensemble mapping for coded aperture imaging—A tutorial," Photonics **11**, 1174 (2024). https://doi.org/10.3390/photonics11121174

J. Rosen, S. Alford, B. Allan, V. Anand, *et al.*, "Roadmap on computational methods in optical imaging and holography [invited]," Appl. Phys. B **130**, 166 (2024). https://doi.org/10.1007/s00340-024-08280-3

S. Gopinath and V. Anand, "Post-ensemble generation with Airy beams for spatial and spectral switching in incoherent imaging," Opt. Lett. **49**, 3247–3250 (2024). https://doi.org/10.1364/OL.522319

O. Tamm, V. Tiwari, **S. Gopinath**, A. S. John Francis Rajeswary, *et al.*, "Super-resolution correlating optical endoscopy," IEEE Access **12**, 76955–76962 (2024). https://doi.org/10.1109/ACCESS.2024.3406209

M. Han, D. Smith, T. Kahro, D. Stonyte, A. Kasikov, D. Gailevicius, V. Tiwari, A. P. Ignatius Xavier, **S. Gopinath**, *et al.*, "Extending the depth of focus of an infrared microscope using a binary axicon fabricated on barium fluoride," Micromachines **15**, 537 (2024). https://doi.org/10.3390/mi15040537

F. G. Arockiaraj, A. P. Ignatius Xavier, **S. Gopinath**, A. S. John Francis Rajeswary, *et al.*, "Optimizing the temporal and spatial resolutions and light throughput of Fresnel incoherent correlation holography in the framework of coded aperture imaging," J. Opt. **26**, 035605 (2024). https://doi.org/10.1088/2040-8986/ad2620

S. Gopinath, A. S. John Francis Rajeswary, and V. Anand, "Sculpting axial characteristics of incoherent imagers by hybridization methods," Opt. Lasers Eng. **172**, 107837 (2024). https://doi.org/10.1016/j.optlaseng.2023.107837

A. P. Ignatius Xavier, F. G. Arockiaraj, **S. Gopinath**, *et al.*, "Single shot 3D incoherent imaging using deterministic and random optical fields with Lucy-Richardson-Rosen algorithm," Photonics **10**, 987 (2023). https://doi.org/10.3390/photonics10090987

A. Bleahu, **S. Gopinath**, T. Kahro, *et al.*, "Self-wavefront interference using transverse splitting holography," Results Phys. **52** 106839 (2023). https://doi.org/10.1016/j.rinp.2023.106839

A. Bleahu, **S. Gopinath**, T. Kahro, *et al.*, "3D incoherent imaging using an ensemble of sparse self-rotating beams," Opt. Express **31**, 26120–26134 (2023). https://doi.org/10.1364/OE.493526

S. Gopinath, A. Bleahu, T. Kahro, *et al.*, "Enhanced design of multiplexed coded masks for Fresnel incoherent correlation holography," Sci. Rep. **13**, 7390 (2023). https://doi.org/10.1038/s41598-023-34492-2

A. Jayavel, **S. Gopinath**, P. Periyasamy Angamuthu, F. G. Arockiaraj, *et al.*, "Improved classification of blurred images with deep-learning networks using Lucy-Richardson-Rosen algorithm," Photonics **10**, 396 (2023). https://doi.org/10.3390/photonics10040396

S. Gopinath, P. Periyasamy Angamuthu, T. Kahro, *et al.*, "Implementation of a large-area diffractive lens using multiple sub-aperture diffractive lenses and computational reconstruction," Photonics **10**, 3 (2022). https://doi.org/10.3390/photonics10010003

P. Periyasamy Angamuthu, F. G. Arockiaraj, **S. Gopinath**, D. Smith, *et al.*, "Deep deconvolution of object information modulated by a refractive lens using Lucy-Richardson-Rosen algorithm," Photonics **9**, 625 (2022). https://doi.org/10.3390/photonics9090625

D. Smith, **S. Gopinath**, F. G. Arockiaraj, *et al.*, "Nonlinear reconstruction of images from patterns generated by deterministic or random optical masks—concepts and review of research," J. Imaging **8**, 174 (2022). https://doi.org/10.3390/jimaging8060174

Master's Thesis (not peer reviewed): **S. Gopinath**, "A semi-synthetic study of multidimensional imaging using a scattering lens," Preprints (2022). https://doi.org/10.20944/preprints202206.0049.v1

Conference Oral Presentations:

IEEE International Conference on Next Generation Electronics (NEleX), Vellore, India (2023); Proceedings: https://doi.org/10.1109/NEleX59773.2023.10421312 (Award: Best Paper Award)

SPIE International Conference on Optical and Photonic Engineering (icOPEN), Singapore (2023); Proceedings: https://doi.org/10.1117/12.2665170

SPIE Holography: Advances and Modern Trends VIII, Prague, Czech Republic (2023); Proceedings: https://doi.org/10.1117/12.3015742

Invited Talks:

8th International Conference on Machine Vision and Applications (ICMVA), Melbourne, Australia (2025)

1st International Conference on Emerging Trends in Optical Technologies (ETOT-I), India (2025)

Laser Research Center, Vilnius University, Lithuania (2024)

Teaching and Supervision Experience at the Institute of Physics, University of Tartu:

Assistant Lecturer (2024): Course – LTFY.03.01 Hands-on Training on Optical Instrumentation: Imaging Systems, Interferometry, and Holography

Co-supervisor, Master's Thesis (2025): Student – Otto Maasik; Project – Practical Post-Recording Spectral Bandwidth Extension in Fresnel Incoherent Correlation Holography

Co-supervisor, Bachelor's Thesis (2024): Student – Oskar Tamm; Project – Super-Resolution Correlation Optical Endoscopy

Supervisor, Bachelor's Seminar Project (2025): Student – Grete Valtin; Project – Design and Demonstration of Multifocal Diffractive Lenses for Imaging Applications

Co-supervisor, Bachelor's Seminar Project (2023): Student – Sanna Kruusmaa; Project – Experimental Demonstration of Shack-Hartmann Wavefront Sensor

Co-supervisor, Bachelor's Seminar Project (2023): Student – Oskar Tamm; Project – Laboratory model of an astronomical telescope using sparse sub-aperture diffractive lenses

Academic Service:

Peer Reviewer for international journals, including: Optics Letters, Optics Express, Optics and Laser Technology, Journal of Optics, Applied Physics B, and Applied Optics

Co-organizer of international conferences, hackathons, and summer school programs organized by the CIPHR group at the Institute of Physics, University of Tartu

Professional Training and Development:

22nd Estonian Summer School on Computer and Systems Science (ESSCaSS), University of Tartu, Estonia (2025)

Erasmus Blended Mobility, 33rd Jyväskylä Summer School, Finland (2024)

FLIR Infrared Camera Training, Kaunas, Lithuania (2024)

The Art of Giving a Popular Science Talk, Estonia – Participant (2023); Speaker (2024)

Industrial Visit – Karl Storz, Tallinn, Estonia (2023)

Achievements, Awards, and Grants:

US provisional patent: Incoherent hybrid imaging systems (2025)

Best student award: Thiagarajar College, India, for outstanding academic performance in the Master's program (2020–2022)

Lab skills competition award: Gandhigram Rural Institute, India, for participating in the Girphy Fest lab skills event (2022)

Optica photo contest: The submitted photo has been featured in Optics and Photonics News (2022) – https://www.optica-opn.org/home/gallery/photo_contests/2022/the_sun/

Estonian doctoral school mobility grant (2025): ~2000 € for participation in the 8th International Conference on Machine Vision and Applications (ICMVA), Melbourne, Australia, 2025

University of Tartu library APC support grant (2026): ~1400 €, for open access publication of the article titled “Axial Resolution Post-Processing Engineering in Fresnel Incoherent Correlation Holography,” which covered 50% of the APC

Outreach and Science Communication:

Three-Minute Thesis Competition, University of Tartu: Incoherent Hybrid Imaging System (INCHIS) – https://www.uttv.ee/naita?id=34804

Research Interviews, ERR Novaator (Estonian National Broadcasting):

Sculpting Axial Characteristics of Incoherent Imagers by Hybridization Methods – https://novaator.err.ee/1609141678/tartu-optikute-uus-pildistusmeetod-roomustab-nii-arste-kui-ka-piltnikke

Post-Ensemble Generation with Airy Beams for Spatial and Spectral Switching in Incoherent Imaging – https://news.err.ee/1609496284/tartu-university-researchers-make-imaging-technology-breakthrough

Skills:

Technical: MATLAB, Building Optical Setups, Microsoft Office, C Programming (Basic)

Soft Skills: Scientific Writing, Mentoring, Teamwork, Project Management

ELULOOKIRJELDUS (EESTI KEELES)

Nimi:	Shivasubramanian Gopinath
Sünniaeg:	30. august 1999
Kodakondsus:	India
Keeled:	inglise, tamili (emakeel)
Aadress:	tuba B206, Füüsika Instituut, W. Ostwaldi 1, 50411 Tartu, Eesti
Telefon:	+372 55580344, +91 8838116170
E-post:	shivasubramanian.gopinath@ut.ee, gopishiva62@gmail.com

Akadeemiline profiil:

Praegune ametikoht: doktorant, nooremteadur ja CIPHR uurimisrühma liige, Tartu Ülikooli Füüsika Instituut, Eesti (2022 – praegu)

Uurimishuvid: arvutuslik kujutamine, mittesidus digitaalne holograafia, kodeeritud apertuuri kujutamine ja difraktsioonoptika

Haridus:

Füüsika magistrikraad, Thiagarajar College, India (2020–2022)

Füüsika bakalaureusekraad, Thiagarajar College, India (2017–2020)

Gümnaasiumiharidus, TVS Higher Secondary School, India (2015–2017)

Põhiharidus, TVS Higher Secondary School, India (2010–2015)

Algkooliharidus, TVS Primary School, India (2005–2010)

Publikatsioonid:

F. G. Arockiaraj, **S. Gopinath**, J. Rosen, and V. Anand, "Invasive imaging through thin scattering layer using special beams with temporal coherence and spatial incoherence," Opt. Laser Technol. **200**, 115130 (2026). https://doi.org/10.1016/j.optlastec.2026.115130

S. Gopinath, J. Rosen, and V. Anand, "Axial resolution post-processing engineering in Fresnel incoherent correlation holography," J. Phys. Photonics **8**, 015041 (2026). https://doi.org/10.1088/2515-7647/ae38ae

P. A. Nair, A. Deshpande, S. S. Kumar, **S. Gopinath**, *et al.*, "Enhancing limited-view photoacoustic vascular images via non-linear Lucy-Richardson deconvolution," Opt. Continuum **4**, 2885–2895 (2025). https://doi.org/10.1364/OPTCON.577884

H. Vardhan, **S. Gopinath**, V. Tiwari, *et al.*, "Coded aperture imaging with helico-conical beams," Appl. Phys. B **131**, 220 (2025). https://doi.org/10.1007/s00340-025-08585-x

E. Puig Vilardell, **S. Gopinath**, V. Tiwari, T. Kahro, *et al.*, "Spatio-spectral correlations in interferenceless coded aperture correlation holography with vortex speckles," Appl. Phys. B **131**, 1–15 (2025). https://doi.org/10.1007/s00340-025-08507-x

V. Tiwari, **S. Gopinath**, T. Kahro, *et al.*, "Recent advances in spatially incoherent coded aperture imaging technologies," Technologies **13**, 210 (2025). https://doi.org/10.3390/technologies13050210

A. P. Ignatius Xavier, T. Kahro, **S. Gopinath**, F. G. Arockiaraj, *et al.*, "Coded aperture imaging using non-linear Lucy-Richardson algorithm," Opt. Laser Technol. **183**, 112300 (2025). https://doi.org/10.1016/j.optlastec.2024.112300

N. Joshi, A. P. Ignatius Xavier, **S. Gopinath**, V. Tiwari, and V. Anand, "Spatial ensemble mapping for coded aperture imaging—A tutorial," Photonics **11**, 1174 (2024). https://doi.org/10.3390/photonics11121174

J. Rosen, S. Alford, B. Allan, V. Anand, *et al.*, "Roadmap on computational methods in optical imaging and holography [invited]," Appl. Phys. B **130**, 166 (2024). https://doi.org/10.1007/s00340-024-08280-3

S. Gopinath and V. Anand, "Post-ensemble generation with Airy beams for spatial and spectral switching in incoherent imaging," Opt. Lett. **49**, 3247–3250 (2024). https://doi.org/10.1364/OL.522319

O. Tamm, V. Tiwari, **S. Gopinath**, A. S. John Francis Rajeswary, *et al.*, "Super-resolution correlating optical endoscopy," IEEE Access **12**, 76955–76962 (2024). https://doi.org/10.1109/ACCESS.2024.3406209

M. Han, D. Smith, T. Kahro, D. Stonyte, A. Kasikov, D. Gailevicius, V. Tiwari, A. P. Ignatius Xavier, **S. Gopinath**, *et al.*, "Extending the depth of focus of an infrared microscope using a binary axicon fabricated on barium fluoride," Micromachines **15**, 537 (2024). https://doi.org/10.3390/mi15040537

F. G. Arockiaraj, A. P. Ignatius Xavier, **S. Gopinath**, A. S. John Francis Rajeswary, *et al.*, "Optimizing the temporal and spatial resolutions and light throughput of Fresnel incoherent correlation holography in the framework of coded aperture imaging," J. Opt. **26**, 035605 (2024). https://doi.org/10.1088/2040-8986/ad2620

S. Gopinath, A. S. John Francis Rajeswary, and V. Anand, "Sculpting axial characteristics of incoherent imagers by hybridization methods," Opt. Lasers Eng. **172**, 107837 (2024). https://doi.org/10.1016/j.optlaseng.2023.107837

A. P. Ignatius Xavier, F. G. Arockiaraj, **S. Gopinath**, *et al.*, "Single shot 3D incoherent imaging using deterministic and random optical fields with Lucy-Richardson-Rosen algorithm," Photonics **10**, 987 (2023). https://doi.org/10.3390/photonics10090987

A. Bleahu, **S. Gopinath**, T. Kahro, *et al.*, "Self-wavefront interference using transverse splitting holography," Results Phys. **52** 106839 (2023). https://doi.org/10.1016/j.rinp.2023.106839

A. Bleahu, **S. Gopinath**, T. Kahro, *et al.*, "3D incoherent imaging using an ensemble of sparse self-rotating beams," Opt. Express **31**, 26120–26134 (2023). https://doi.org/10.1364/OE.493526

S. Gopinath, A. Bleahu, T. Kahro, *et al.*, "Enhanced design of multiplexed coded masks for Fresnel incoherent correlation holography," Sci. Rep. **13**, 7390 (2023). https://doi.org/10.1038/s41598-023-34492-2

A. Jayavel, **S. Gopinath**, P. Periyasamy Angamuthu, F. G. Arockiaraj, *et al.*, "Improved classification of blurred images with deep-learning networks using Lucy-Richardson-Rosen algorithm," Photonics **10**, 396 (2023). https://doi.org/10.3390/photonics10040396

S. Gopinath, P. Periyasamy Angamuthu, T. Kahro, *et al.*, "Implementation of a large-area diffractive lens using multiple sub-aperture diffractive lenses and computational reconstruction," Photonics **10**, 3 (2022). https://doi.org/10.3390/photonics10010003

P. Periyasamy Angamuthu, F. G. Arockiaraj, **S. Gopinath**, D. Smith, *et al.*, "Deep deconvolution of object information modulated by a refractive lens using Lucy-Richardson-Rosen algorithm," Photonics **9**, 625 (2022). https://doi.org/10.3390/photonics9090625

D. Smith, **S. Gopinath**, F. G. Arockiaraj, *et al.*, "Nonlinear reconstruction of images from patterns generated by deterministic or random optical masks—concepts and review of research," J. Imaging **8**, 174 (2022). https://doi.org/10.3390/jimaging8060174

Magistritöö (retsenseerimata): **S. Gopinath**, "A semi-synthetic study of multi-dimensional imaging using a scattering lens," Preprints (2022). https://doi.org/10.20944/preprints202206.0049.v1

Konverentsiettekanded:

IEEE International Conference on Next Generation Electronics (NEleX), Vellore, India (2023); artikli kogumik: https://doi.org/10.1109/NEleX59773.2023.10421312 (auhind: parim artikkel)

SPIE International Conference on Optical and Photonic Engineering (icOPEN), Singapur (2023); artikli kogumik: https://doi.org/10.1117/12.2665170

SPIE Holography: Advances and Modern Trends VIII, Praha, Tšehhi (2023); artikli kogumik: https://doi.org/10.1117/12.3015742

Kutsutud ettekanded:

8th International Conference on Machine Vision and Applications (ICMVA), Melbourne, Austraalia (2025)

1st International Conference on Emerging Trends in Optical Technologies (ETOT-I), India (2025)

Laser Research Center, Vilniuse Ülikool, Leedu (2024)

Õpetamis- ja juhendamiskogemus Tartu Ülikooli Füüsika Instituudis:

Õppeassistent (2024): kursus – LTFY.03.01 Hands-on Training on Optical Instrumentation: Imaging Systems, Interferometry, and Holography

Kaasjuhendaja, magistritöö (2025): üliõpilane – Otto Maasik; teema – Practical Post-Recording Spectral Bandwidth Extension in Fresnel Incoherent Correlation Holography

Kaasjuhendaja, bakalaureusetöö (2024): üliõpilane – Oskar Tamm; teema – Super-Resolution Correlation Optical Endoscopy

Juhendaja, bakalaureuse seminariprojekt (2025): üliõpilane – Grete Valtin; teema – Design and Demonstration of Multifocal Diffractive Lenses for Imaging Applications

Kaasjuhendaja, bakalaureuse seminariprojekt (2023): üliõpilane – Sanna Kruusmaa; teema – Experimental Demonstration of Shack-Hartmann Wavefront Sensor

Kaasjuhendaja, bakalaureuse seminariprojekt (2023): üliõpilane – Oskar Tamm; teema – Laboratory model of an Astronomical Telescope using Sparse Sub-Aperture Diffractive Lenses

Akadeemiline tegevus:

Retsensent rahvusvahelistes teadusajakirjades, sh Optics Letters, Optics Express, Optics and Laser Technology, Journal of Optics, Applied Physics B ja Applied Optics

Kaasorganiseerija rahvusvahelistel konverentsidel, häkatonidel ja suvekoolidel, mida korraldas CIPHR uurimisrühm Tartu Ülikooli Füüsika Instituudis

Täiendkoolitus ja professionaalne areng:

22. Eesti arvuti- ja süsteemiteaduse suvekool (ESSCaSS), Tartu Ülikool, Eesti (2025)

Erasmus Blended Mobility, 33. Jyväskylä suvekool, Soome (2024)

FLIR infrapunakaamera koolitus, Kaunas, Leedu (2024)

The Art of Giving a Popular Science Talk, Eesti – osaleja (2023); esineja (2024)

Tööstusvisiit – Karl Storz, Tallinn, Eesti (2023)

Saavutused, auhinnad ja grandid:

USA ajutine patent: Incoherent hybrid imaging systems (2025)

Parima üliõpilase auhind: Thiagarajar College, India, silmapaistvate akadeemiliste tulemuste eest magistriõppes (2020 – 2022)

Laborioskuste võistluse auhind: Gandhigram Rural Institute, India, Girphy Festi laborioskuste võistlus (2022)

Optica fotokonkurss: esitatud foto avaldati ajakirjas Optics and Photonics News (2022) – https://www.optica-opn.org/home/gallery/photo_contests/2022/the_sun/

Eesti Doktorikooli mobiilsusgrant (2025): ~2000 € osalemiseks 8. rahvusvahelisel konverentsil International Conference on Machine Vision and Applications (ICMVA), Melbourne, Austraalia (2025)

Tartu Ülikooli raamatukogu APC toetusgrant (2026): ~1400 € avatud juurdepääsuga publikatsiooni avaldamiseks “Axial Resolution Post-Processing Engineering in Fresnel Incoherent Correlation Holography,” mis kattis 50% APC tasust

Teaduskommunikatsioon ja teaduse populariseerimine:

Three-Minute Thesis Competition, Tartu Ülikool: Incoherent Hybrid Imaging System (INCHIS) – https://www.uttv.ee/naita?id=34804

Uurimisintervjuud, ERR Novaator (Eesti Rahvusringhääling):

Sculpting Axial Characteristics of Incoherent Imagers by Hybridization Methods – https://novaator.err.ee/1609141678/tartu-optikute-uus-pildistusmeetod-roomustab-nii-arste-kui-ka-piltnikke

Post-Ensemble Generation with Airy Beams for Spatial and Spectral Switching in Incoherent Imaging – https://news.err.ee/1609496284/tartu-university-researchers-make-imaging-technology-breakthrough

Oskused:

Tehnilised oskused: MATLAB, optiliste süsteemide ülesehitamine, Microsoft Office, C programmeerimine (algteadmised)

Üldoskused: teaduslik kirjutamine, juhendamine, meeskonnatöö, projektijuhtimine

DISSERTATIONES PHYSICAE UNIVERSITATIS TARTUENSIS

1. **Andrus Ausmees**. XUV-induced electron emission and electron-phonon interaction in alkali halides. Tartu, 1991.
2. **Heiki Sõnajalg**. Shaping and recalling of light pulses by optical elements based on spectral hole burning. Tartu, 1991.
3. **Sergei Savihhin**. Ultrafast dynamics of F-centers and bound excitons from picosecond spectroscopy data. Tartu, 1991.
4. **Ergo Nõmmiste**. Leelishalogeniidide röntgenelektronemissioon kiiritamisel footonitega energiaga 70–140 eV. Tartu, 1991.
5. **Margus Rätsep**. Spectral gratings and their relaxation in some low-temperature impurity-doped glasses and crystals. Tartu, 1991.
6. **Tõnu Pullerits**. Primary energy transfer in photosynthesis. Model calculations. Tartu, 1991.
7. **Olev Saks**. Attoampri diapasoonis voolude mõõtmise füüsikalised alused. Tartu, 1991.
8. **Andres Virro**. AlGaAsSb/GaSb heterostructure injection lasers. Tartu, 1991.
9. **Hans Korge**. Investigation of negative point discharge in pure nitrogen at atmospheric pressure. Tartu, 1992.
10. **Jüri Maksimov**. Nonlinear generation of laser VUV radiation for high-resolution spectroscopy. Tartu, 1992.
11. **Mark Aizengendler**. Photostimulated transformation of aggregate defects and spectral hole burning in a neutron-irradiated sapphire. Tartu, 1992.
12. **Hele Siimon**. Atomic layer molecular beam epitaxy of A^2B^6 compounds described on the basis of kinetic equations model. Tartu, 1992.
13. **Tõnu Reinot**. The kinetics of polariton luminescence, energy transfer and relaxation in anthracene. Tartu, 1992.
14. **Toomas Rõõm**. Paramagnetic H^{2-} and F^+ centers in CaO crystals: spectra, relaxation and recombination luminescence. Tallinn, 1993.
15. **Erko Jalviste**. Laser spectroscopy of some jet-cooled organic molecules. Tartu, 1993.
16. **Alvo Aabloo**. Studies of crystalline celluloses using potential energy calculations. Tartu, 1994.
17. **Peeter Paris**. Initiation of corona pulses. Tartu, 1994.
18. **Павел Рубин**. Локальные дефектные состояния в CuO_2 плоскостях высокотемпературных сверхпроводников. Тарту, 1994.
19. **Olavi Ollikainen**. Applications of persistent spectral hole burning in ultrafast optical neural networks, time-resolved spectroscopy and holographic interferometry. Tartu, 1996.
20. **Ülo Mets**. Methodological aspects of fluorescence correlation spectroscopy. Tartu, 1996.
21. **Mikhail Danilkin**. Interaction of intrinsic and impurity defects in CaS:Eu luminophors. Tartu, 1997.

22. **Ирина Кудрявцева**. Создание и стабилизация дефектов в кристаллах KBr, KCl, RbCl при облучении ВУФ-радиацией. Тарту, 1997.
23. **Andres Osvet**. Photochromic properties of radiation-induced defects in diamond. Tartu, 1998.
24. **Jüri Örd**. Classical and quantum aspects of geodesic multiplication. Tartu, 1998.
25. **Priit Sarv**. High resolution solid-state NMR studies of zeolites. Tartu, 1998.
26. **Сергей Долгов**. Электронные возбуждения и дефектообразование в некоторых оксидах металлов. Тарту, 1998.
27. **Kaupo Kukli**. Atomic layer deposition of artificially structured dielectric materials. Tartu, 1999.
28. **Ivo Heinmaa**. Nuclear resonance studies of local structure in $RBa_2Cu_3O_{6+x}$ compounds. Tartu, 1999.
29. **Aleksander Shelkan**. Hole states in CuO_2 planes of high temperature superconducting materials. Tartu, 1999.
30. **Dmitri Nevedrov**. Nonlinear effects in quantum lattices. Tartu, 1999.
31. **Rein Ruus**. Collapse of 3d (4f) orbitals in 2p (3d) excited configurations and its effect on the x-ray and electron spectra. Tartu, 1999.
32. **Valter Zazubovich**. Local relaxation in incommensurate and glassy solids studied by Spectral Hole Burning. Tartu, 1999.
33. **Indrek Reimand**. Picosecond dynamics of optical excitations in GaAs and other excitonic systems. Tartu, 2000.
34. **Vladimir Babin**. Spectroscopy of exciton states in some halide macro- and nanocrystals. Tartu, 2001.
35. **Toomas Plank**. Positive corona at combined DC and AC voltage. Tartu, 2001.
36. **Kristjan Leiger**. Pressure-induced effects in inhomogeneous spectra of doped solids. Tartu, 2002.
37. **Helle Kaasik**. Nonperturbative theory of multiphonon vibrational relaxation and nonradiative transitions. Tartu, 2002.
38. **Tõnu Laas**. Propagation of waves in curved spacetimes. Tartu, 2002.
39. **Rünno Lõhmus**. Application of novel hybrid methods in SPM studies of nanostructural materials. Tartu, 2002.
40. **Kaido Reivelt**. Optical implementation of propagation-invariant pulsed free-space wave fields. Tartu, 2003.
41. **Heiki Kasemägi**. The effect of nanoparticle additives on lithium-ion mobility in a polymer electrolyte. Tartu, 2003.
42. **Villu Repän**. Low current mode of negative corona. Tartu, 2004.
43. **Алексей Котлов**. Оксианионные диэлектрические кристаллы: зонная структура и электронные возбуждения. Tartu, 2004.
44. **Jaak Talts**. Continuous non-invasive blood pressure measurement: comparative and methodological studies of the differential servo-oscillometric method. Tartu, 2004.
45. **Margus Saal**. Studies of pre-big bang and braneworld cosmology. Tartu, 2004.

46. **Eduard Gerškevitš**. Dose to bone marrow and leukaemia risk in external beam radiotherapy of prostate cancer. Tartu, 2005.
47. **Sergey Shchemelyov**. Sum-frequency generation and multiphoton ionization in xenon under excitation by conical laser beams. Tartu, 2006.
48. **Valter Kiisk**. Optical investigation of metal-oxide thin films. Tartu, 2006.
49. **Jaan Aarik**. Atomic layer deposition of titanium, zirconium and hafnium dioxides: growth mechanisms and properties of thin films. Tartu, 2007.
50. **Astrid Rekker**. Colored-noise-controlled anomalous transport and phase transitions in complex systems. Tartu, 2007.
51. **Andres Punning**. Electromechanical characterization of ionic polymer-metal composite sensing actuators. Tartu, 2007.
52. **Indrek Jõgi**. Conduction mechanisms in thin atomic layer deposited films containing TiO_2. Tartu, 2007.
53. **Aleksei Krasnikov**. Luminescence and defects creation processes in lead tungstate crystals. Tartu, 2007.
54. **Küllike Rägo**. Superconducting properties of MgB_2 in a scenario with intra- and interband pairing channels. Tartu, 2008.
55. **Els Heinsalu**. Normal and anomalously slow diffusion under external fields. Tartu, 2008.
56. **Kuno Kooser**. Soft x-ray induced radiative and nonradiative core-hole decay processes in thin films and solids. Tartu, 2008.
57. **Vadim Boltrushko**. Theory of vibronic transitions with strong nonlinear vibronic interaction in solids. Tartu, 2008.
58. **Andi Hektor**. Neutrino Physics beyond the Standard Model. Tartu, 2008.
59. **Raavo Josepson**. Photoinduced field-assisted electron emission into gases. Tartu, 2008.
60. **Martti Pärs**. Study of spontaneous and photoinduced processes in molecular solids using high-resolution optical spectroscopy. Tartu, 2008.
61. **Kristjan Kannike**. Implications of neutrino masses. Tartu, 2008.
62. **Vigen Issahhanjan**. Hole and interstitial centres in radiation-resistant MgO single crystals. Tartu, 2008.
63. **Veera Krasnenko**. Computational modeling of fluorescent proteins. Tartu, 2008.
64. **Mait Müntel**. Detection of doubly charged higgs boson in the CMS detector. Tartu, 2008.
65. **Kalle Kepler**. Optimisation of patient doses and image quality in diagnostic radiology. Tartu, 2009.
66. **Jüri Raud**. Study of negative glow and positive column regions of capillary HF discharge. Tartu, 2009.
67. **Sven Lange**. Spectroscopic and phase-stabilisation properties of pure and rare-earth ions activated ZrO_2 and HfO_2. Tartu, 2010.
68. **Aarne Kasikov**. Optical characterization of inhomogeneous thin films. Tartu, 2010.
69. **Heli Valtna-Lukner**. Superluminally propagating localized optical pulses. Tartu, 2010.

70. **Artjom Vargunin**. Stochastic and deterministic features of ordering in the systems with a phase transition. Tartu, 2010.
71. **Hannes Liivat**. Probing new physics in e+e− annihilations into heavy particles via spin orientation effects. Tartu, 2010.
72. **Tanel Mullari**. On the second order relativistic deviation equation and its applications. Tartu, 2010.
73. **Aleksandr Lissovski**. Pulsed high-pressure discharge in argon: spectroscopic diagnostics, modeling and development. Tartu, 2010.
74. **Aile Tamm**. Atomic layer deposition of high-permittivity insulators from cyclopentadienyl-based precursors. Tartu, 2010.
75. **Janek Uin**. Electrical separation for generating standard aerosols in a wide particle size range. Tartu, 2011.
76. **Svetlana Ganina**. Hajusandmetega ülesanded kui üks võimalus füüsikaõppe efektiivsuse tõstmiseks. Tartu, 2011
77. **Joel Kuusk**. Measurement of top-of-canopy spectral reflectance of forests for developing vegetation radiative transfer models. Tartu, 2011.
78. **Raul Rammula**. Atomic layer deposition of HfO_2 – nucleation, growth and structure development of thin films. Tartu, 2011.
79. **Сергей Наконечный**. Исследование электронно-дырочных и интерстициал-вакансионных процессов в монокристаллах MgO и LiF методами термоактивационной спектроскопии. Тарту, 2011.
80. **Niina Voropajeva**. Elementary excitations near the boundary of a strongly correlated crystal. Tartu, 2011.
81. **Martin Timusk**. Development and characterization of hybrid electro-optical materials. Tartu, 2012, 106 p.
82. **Merle Lust**. Assessment of dose components to Estonian population. Tartu, 2012, 84 p.
83. **Karl Kruusamäe**. Deformation-dependent electrode impedance of ionic electromechanically active polymers. Tartu, 2012, 128 p.
84. **Liis Rebane**. Measurement of the $W \to \tau\nu$ cross section and a search for a doubly charged Higgs boson decaying to τ-leptons with the CMS detector. Tartu, 2012, 156 p.
85. **Jevgeni Šablonin**. Processes of structural defect creation in pure and doped MgO and NaCl single crystals under condition of low or super high density of electronic excitations. Tartu, 2013, 145 p.
86. **Riho Vendt**. Combined method for establishment and dissemination of the international temperature scale. Tartu, 2013, 108 p.
87. **Peeter Piksarv**. Spatiotemporal characterization of diffractive and non-diffractive light pulses. Tartu, 2013, 156 p.
88. **Anna Šugai**. Creation of structural defects under superhigh-dense irradiation of wide-gap metal oxides. Tartu, 2013, 108 p.
89. **Ivar Kuusik**. Soft X-ray spectroscopy of insulators. Tartu, 2013, 113 p.
90. **Viktor Vabson**. Measurement uncertainty in Estonian Standard Laboratory for Mass. Tartu, 2013, 134 p.

91. **Kaupo Voormansik**. X-band synthetic aperture radar applications for environmental monitoring. Tartu, 2014, 117 p.
92. **Deivid Pugal**. hp-FEM model of IPMC deformation. Tartu, 2014, 143 p.
93. **Siim Pikker**. Modification in the emission and spectral shape of photo-stable fluorophores by nanometallic structures. Tartu, 2014, 98 p.
94. **Mihkel Pajusalu**. Localized Photosynthetic Excitons. Tartu, 2014, 183 p.
95. **Taavi Vaikjärv**. Consideration of non-adiabaticity of the Pseudo-Jahn-Teller effect: contribution of phonons. Tartu, 2014, 129 p.
96. **Martin Vilbaste**. Uncertainty sources and analysis methods in realizing SI units of air humidity in Estonia. Tartu, 2014, 111 p.
97. **Mihkel Rähn**. Experimental nanophotonics: single-photon sources- and nanofiber-related studies. Tartu, 2015, 107 p.
98. **Raul Laasner**. Excited state dynamics under high excitation densities in tungstates. Tartu, 2015, 125 p.
99. **Andris Slavinskis**. EST Cube-1 attitude determination. Tartu, 2015, 104 p.
100. **Karlis Zalite**. Radar Remote Sensing for Monitoring Forest Floods and Agricultural Grasslands. Tartu, 2016, 124 p.
101. **Kaarel Piip**. Development of LIBS for *in-situ* study of ITER relevant materials. Tartu, 2016, 93 p.
102. **Kadri Isakar**. ^{210}Pb in Estonian air: long term study of activity concentrations and origin of radioactive lead. Tartu, 2016, 107 p.
103. **Artur Tamm**. High entropy alloys: study of structural properties and irradiation response. Tartu, 2016, 115 p.
104. **Rasmus Talviste**. Atmospheric-pressure He plasma jet: effect of dielectric tube diameter. Tartu, 2016, 107 p.
105. **Andres Tiko**. Measurement of single top quark properties with the CMS detector. Tartu, 2016, 161 p.
106. **Aire Olesk**. Hemiboreal Forest Mapping with Interferometric Synthetic Aperture Radar. Tartu, 2016, 121 p.
107. **Fred Valk**. Nitrogen emission spectrum as a measure of electric field strength in low-temperature gas discharges. Tartu, 2016, 149 p.
108. **Manoop Chenchiliyan**. Nano-structural Constraints for the Picosecond Excitation Energy Migration and Trapping in Photosynthetic Membranes of Bacteria. Tartu, 2016, 115p.
109. **Lauri Kaldamäe**. Fermion mass and spin polarisation effects in top quark pair production and the decay of the higgs boson. Tartu, 2017, 104 p.
110. **Marek Oja**. Investigation of nano-size α- and transition alumina by means of VUV and cathodoluminescence spectroscopy. Tartu, 2017, 89 p.
111. **Viktoriia Levushkina**. Energy transfer processes in the solid solutions of complex oxides. Tartu, 2017, 101 p.
112. **Mikk Antsov**. Tribomechanical properties of individual 1D nanostructures: experimental measurements supported by finite element method simulations. Tartu, 2017, 101 p.
113. **Hardi Veermäe**. Dark matter with long range vector-mediated interactions. Tartu, 2017, 137 p.

114. **Aris Auzans**. Development of computational model for nuclear energy systems analysis: natural resources optimisation and radiological impact minimization. Tartu, 2018, 138 p.
115. **Aleksandr Gurev**. Coherent fluctuating nephelometry application in laboratory practice. Tartu, 2018, 150 p.
116. **Ardi Loot**. Enhanced spontaneous parametric downconversion in plasmonic and dielectric structures. Tartu, 2018, 164 p.
117. **Andreas Valdmann**. Generation and characterization of accelerating light pulses. Tartu, 2019, 85 p.
118. **Mikk Vahtrus**. Structure-dependent mechanical properties of individual one-dimensional metal-oxide nanostructures. Tartu, 2019, 110 p.
119. **Ott Vilson**. Transformation properties and invariants in scalar-tensor theories of gravity. Tartu, 2019, 183 p.
120. **Indrek Sünter**. Design and characterisation of subsystems and software for ESTCube-1 nanosatellite. Tartu, 2019, 195 p.
121. **Marko Eltermann**. Analysis of samarium doped TiO_2 optical and multiresponse oxygen sensing capabilities. Tartu, 2019, 113 p.
122. **Kalev Erme**. The effect of catalysts in plasma oxidation of nitrogen oxides. Tartu, 2019, 114 p.
123. **Sergey Koshkarev**. A phenomenological feasibility study of the possible impact of the intrinsic heavy quark (charm) mechanism on the production of doubly heavy mesons and baryons. Tartu, 2020, 134 p.
124. **Kristi Uudeberg**. Optical Water Type Guided Approach to Estimate Water Quality in Inland and Coastal Waters. Tartu, 2020, 222 p.
125. **Daniel Blixt**. Hamiltonian analysis of covariant teleparallel theories of gravity. Tartu, 2021, 142 p.
126. **Ulbossyn Ualikhanova**. Gravity theories based on torsion: theoretical and observational constraints. Tartu, 2021, 154 p.
127. **Iaroslav Iakubivskyi**. Nanospacecraft for Technology Demonstration and Science Missions. Tartu, 2021, 177 p.
128. **Heido Trofimov**. Polluted clouds at air pollution hot spots help to better understand anthropogenic impacts on Earth's climate. Tartu, 2022, 96 p.
129. **Ott Rebane**. *In situ* non-contact sensing of microbiological contamination by fluorescence spectroscopy. Tartu, 2022, 157 p.
130. **Juhan Saaring**. Ultrafast Relaxation Processes in Ternary Hexafluorides Studied under Synchrotron Radiation Excitation. Tartu, 2022, 106 p.
131. **Ahmet Ilker Topuz**. Quantitative and qualitative investigations for muon scattering tomography via GEANT4 simulations: A computational study. Tartu, 2023, 163 p.
132. **Nico Benincasa**. Phase transitions and gravitational waves in models of dark matter. Tartu, 2023, 206 p.
133. **Kaja Pae**. Electron-phonon interactions in local degenerate electronic states in solids. Tartu, 2024, 201 p.
134. **Kristjan Müürsepp**. Phenomenological implications of Standard Model extensions. Tartu, 2024, 136 p.

135. **Ye Wang**. Investigating the properties of metal surfaces under high electric fields based on ab initio calculations. Tartu, 2024, 107 p.
136. **Laxmipriya Pati**. The effects of non-Riemannian connection in teleparallel gravity. Tartu, 2025, 172 p.
137. **Débora Aguiar Gomes**. Theoretical and astrophysical aspects of extended general relativity. Tartu, 2025, 169 p.
138. **Mina Hajizadeh Omaslanolya**. Structure and dynamics of photoactive proteins studied by (in situ-) neutron scattering methods. Tartu, 2025, 150 p.
139. **Aditya Savio Paul**. Advancing the study of small solar system bodies through multi-agent mapping and characterization. Tartu, 2025, 244 p.
140. **Sanu Bifal Maji**. Synthesis and luminescence investigation of nano-particles doped with Pr^{3+} ions in selected fluoride and phosphate hosts. Tartu, 2025, 114 p.
141. **Ernest Michael Priidik Gallagher**. On the internal gauge theory analogy to the Cartan Khronon theory of gravity. Tartu, 2026, 221 p.
142. **Maria Naeem**. First order electroweak radiative corrections to the decay of the polarised *W* boson. Tartu, 2026, 236 p.
143. **Konstantinos Pallikaris**. Novel black holes in Einstein gravity. Tartu, 2026, 133 p.
144. **Aleksei Kubarski**. Dynamical symmetry breaking and dark matter. Tartu, 2026, 133 p.
145. **Lucy Zheng**. Cartan Khronon – Real space-time structure. Tartu, 2026, 193 p.
146. **Muhammad Usama Jamal**. Energy transfer to luminescence centres in alkali and rare-earth metal molybdates. Tartu, 2026, 100 p.
147. **Vasiliki Karanasou**. Exotic spherically symmetric objects in modified gravity. Tartu, 2026, 134 p.
148. **Andrei Goronovski**. Systematic study and NORM-LCA methodology development of NORM aspects in the bauxite residue valorization chain. Tartu, 2026, 158 p.
149. **Hando Tohver**. Open-Source Modeling Approaches for Radioactive Waste Management in Nuclear Newcomer Countries. Tartu, 2026, 153 p.